The Henryk Niewodniczański
INSTITUTE OF NUCLEAR PHYSICS
Polish Academy of Sciences
ul. Radzikowskiego 152, 31-342 Kraków, Poland

https://www.ifj.edu.pl/badania/publikacje/

Kraków, July 23, 2025

New Physics searches via Higgs boson couplings to di-bosons

Magdalena Sławińska

Monograph

Wydano nakładem Instytutu Fizyki Jądrowej
im. Henryka Niewodniczańskiego
Polskiej Akademii Nauk
Kraków: 2025

Recenzenci:
Prof. dr hab. Barbara Wosiek
Prof. dr hab. Wiesław Płaczek

ISBN: 978-83-63542-43-6 (print)
ISBN: 978-83-63542-45-0 (pdf)
DOI: https://doi.org/10.48733/978-83-63542-45-0

Contents

Abstract

The Higgs boson is the last discovered particle of the Standard Model (SM) and the only known fundamental scalar. It crowns the theoretical construction of the SM by providing masses to electroweak bosons through the mechanism of spontaneous symmetry breaking. The essential feature of this mechanism is the famous "Mexican hat" potential with non-zero vacuum expectation value. Measurements of Higgs boson coupling strengths to bosons and fermions, in agreement with SM predictions, have experimentally confirmed the Brout-Englert-Higgs mechanism of electroweak symmetry breaking. With more data being collected by ATLAS and CMS experiments at the Large Hadron Collider (LHC), more subtle properties of the Higgs boson can be revealed. These measurements will either confirm the SM nature of this particle, leading to a better understanding of the SM, or hint at the existence of beyond Standard Model (BSM) interactions.

In this monograph I present results of two sets of studies, that I carried out within the ATLAS experiment, that were aimed at measuring the Higgs potential and searching for beyond Standard Model (BSM) deviations to its shape. One set of analyses uses leptonic Higgs boson decays to W bosons. I measured Higgs boson production cross-sections in gluon fusion and vector boson fusion and constrained Higgs boson couplings to polarised electroweak bosons, thus probing the Higgs potential at its minimum. The other class of measurements focuses on Higgs bosons self-interactions that result from the global shape of the Higgs potential. They are performed by studying the production of the Higgs boson pairs. Due to a very small cross-section for the di-Higgs production predicted by the SM, an observation of this process with the currently available data would hint to the presence of BSM phenomena in the Higgs sector. To maximise sensitivity to Higgs pair production at the LHC, several final states are statistically combined. Results of feasibility studies for the upgraded LHC are also reported, using the $b\bar{b}\gamma\gamma$ final state.

Within experimental uncertainties, a good agreement has been found with the Standard Model and constraints have been set on selected BSM models.

Streszczenie

Bozon Higgsa jest ostatnią odkrytą cząstką Modelu Standardowego (SM) i jedyną znaną fundamentalną cząstką skalarną. Wieńczy ona teoretyczną konstrukcję Modelu Standardowego, nadając masy bozonom elektrosłabym poprzez mechanizm spontanicznego łamania symetrii. Istotną cechą tego mechanizmu jest słynny potencjał w kształcie meksykańskiego kapelusza z niezerową wartością oczekiwaną próżni. Pomiary sił sprzężenia bozonu Higgsa z bozonami i fermionami, zgodne z przewidywaniami SM w granicach niepewności pomiarowych, potwierdziły eksperymentalnie mechanizm łamania symetrii elektrosłabej Brouta-Englerta-Higgsa. Wraz z gromadzeniem większej ilości danych przez eksperymenty ATLAS i CMS przy Wielkim Zderzaczu Hadronów (Large Hadron Collider, LHC), mogą zostać odkryte bardziej subtelne właściwości bozonu Higgsa. Pomiary te albo potwierdzą naturę SM tej cząstki, prowadząc do lepszego zrozumienia SM, albo wskażą na istnienie oddziaływań poza Modelem Standardowym (BSM).

W niniejszej monografii przedstawiam wyniki dwóch linii badań, które przeprowadziłam w ramach eksperymentu ATLAS. Miały one na celu pomiary potencjału Higgsa i poszukiwanie odchyleń od jego kształtu wywołanymi przez nieznane oddziaływania poza Modelem Standardowym (BSM). Pierwsza klasa analiz wykorzystuje leptonowe rozpady bozonu Higgsa na bozony W. Zmierzyłam przekroje czynne na produkcję bozonów Higgsa w procesach fuzji gluonów i fuzji bosonów elektrosłabych oraz sprzężenia bozonów Higgsa ze spolaryzowanymi bozonami elektrosłabymi W i Z. W ten sposób zbadałam potencjał bozonu Higgsa w jego minimum. Druga klasa pomiarów skupia się na samo-oddziaływaniach bozonów Higgsa, które wynikają z globalnego kształtu jego potencjału. Jest ona wykonywana poprzez badanie produkcji par bozonów Higgsa. Ze względu na bardzo mały przekrój czynny na produkcję dwóch bozonów Higgsa przewidywany przez SM, obserwacja tego procesu na podstawie obecnie dostępnych danych wskazywałaby na obecność

zjawisk BSM w sektorze Higgsa. Aby zmaksymalizować czułość na produkcję par cząstek Higgsa w LHC, wykonana jest kombinacja statystyczna kilku stanów końcowych. Przedstawiam również wyniki studiów wykonalności dla zmodernizowanego LHC, wykorzystując stan końcowy $b\bar{b}\gamma\gamma$.

W ramach niepewności eksperymentalnych uzyskałam dobrą zgodność z Modelem Standardowym i ustaliłam ograniczenia dla wybranych modeli BSM.

Acknowledgements

This monograph is the result of many years of work and effort, and I could not have completed it without the support of many people. I would like to thank them here.

To Bob van Eijk, thanks to whom I joined the ATLAS experiment. During my postdoc at Nikhef he provided the vision in Higgs pairs searches and necessary support. I am thankful to him for always having time for discussions, for sharing his experience and giving me feedback on project organisation and working with PhD students. To the Nikhef group: To Stan Bentvelsen, Wouter Verkerke, Pamela Ferrari for challenging discussions, to Wouter van den Wollenberg for his many questions and enthusiasm, to Lucrezia Bruni, Federica Pasquali, Dominik Duda for our work together, to Lydia Brenner for discussions about physics and life, and to others.

To Leandro Nissati, for sharing his enthusiasm in Higgs pair measurements and his support during my first years in ATLAS.

To the LHC Higgs Cross Section Working group, in particular for Sally Dawson, Michael Spira, Christoph Englert, Gudrun Heinrich, and Eleni Vryonidou for valuable discussions and sharing their expertise in Higgs Pair cross-section measurements. To Tilman Plehn, Johann Brehmer, Marco Zaro and Gino Isidori for feedback on theoretical aspects of polarisation-dependent couplings.

To the ATLAS Collaboration, and in particular to Higgs Working Group, for much feedback during preparation of analyses included in this monograph.

To the members of VBSCan COST Action, in particular to Pietro Govoni for inspiring meetings and trusting me with leading group efforts.

To my IFJ PAN ATLAS group: To Anna Kaczmarska, Paweł Bruckman De Renstrom, Bartek Żabiński for inspiring discussions, to Ewa Stanecka for support and feedback, to Barbara Wosiek, for her critical and constructive comments during the preparation of this monograph, to Beata Murzyn and

Monika Ławik hor helping me navigate through the bureaucracy of IFJ PAN.

To my husband Marek for believing in me and supporting me in everything I do. Finally, to my daughter Cecylia, for giving me perspective on work and life.

Statement on author's contribution

The physics of the Higgs boson has been my major research interest since 2013. I have investigated several processes involving this particle and measured properties of this newly discovered boson in order to search for possible deviations from the Standard Model (SM) predictions. My studies have been performed within the ATLAS experiment at the Large Hadron Collider (LHC).

Higgs boson pair searches

I joined the ATLAS Collaboration in 2013, about a year after the Higgs boson discovery, with an interest in establishing, whether the spontaneous electroweak symmetry breaking in the electroweak sector proceeds indeed via the Higgs mechanism. My research in years 2013-2018 focused on observing Higgs boson pair production. This process enables extracting the trilinear Higgs self-coupling, that is directly related to the shape of the Higgs potential. The measurement of the coupling strength of the Higgs boson self-interaction is crucial to establish if electroweak symmetry breaking is triggered by the Standard Model Higgs mechanism or some other, hitherto unknown dynamics. Higgs pair production at the LHC, in the SM, is mediated at the leading order by two Feynman diagrams. Only one of them is sensitive to the trilinear Higgs couplings and negative interference between the two contributions decreases the rates of observed Higgs pairs. I found that Higgs pair production is most sensitive to the trilinear coupling at the Higgs resonance itself and applied this finding to the $b\bar{b}\gamma\gamma$ final state of the di-Higgs decays [1].

In years 2014-2018 I was a co-convener of the Di-Higgs subgroup of the LHC Higgs Cross Section Working Group at CERN. This group had been established in order to provide recommendations and harmonise theory inputs to experimental analyses and physics benchmarks to study. For Higgs pair

procuction which, according to the SM predictions, was too rare a process to be observed at the current run of the LHC, our group recommended generic models predicting enhancement of the cross-section. I co-edited the di-Higgs chapter to CERN Yellow Report 4 [2]. This monograph is a roadmap for particle physics, providing recommendations for physics measurements and theoretical frameworks to compare experimental findings with theory predictions.

In 2015 I was involved in preparing a study summarising statistical combination of di-Higgs searches [3] performed at a proton-proton collision energy of 8 TeV, using four final states: $b\bar{b}b\bar{b}$, $b\bar{b}\tau\tau$, $b\bar{b}\gamma\gamma$, and $W^+W^-\gamma\gamma$. I was not directly involved in the data analysis itself, but appointed as an ATLAS editorial board member (an internal review proces by the ATLAS Collaboration), responsible for cross-checking preliminary results, helping the analysis team to complete the study, interpret results and write the paper. The outcome of this study includes limits on the SM Higgs boson production cross-section and exclusions of several BSM scenarions.

I continued Higgs pair searches using the $b\bar{b}\gamma\gamma$ final state. I performed a study of the $b\bar{b}\gamma\gamma$ background in the analysis of data collected at a centre-of-mass energy of 13 TeV [4]. I took part in combining results of double Higgs boson searches performed in ATLAS using up to 36.1 fb^{-1} and final states: $b\bar{b}b\bar{b}$, $b\bar{b}W^+W^-$, $b\bar{b}\tau\tau$, $b\bar{b}\gamma\gamma$, $W^+W^-W^+W^-$ and $W^+W^-\gamma\gamma$ [5]. I provided theory inputs for the SM, electroweak singlet and anomalous Higgs self-coupling interpretations. The results of this combination are 95% confidence level exclusion limits on the SM Higgs boson pair production cross-section. It yields in observation (expectation) 6.9 (10) times the predicted Standard Model cross-section. Limits are also set on the ratio of the Higgs boson self-coupling to its Standard Model value, κ_λ. This ratio is constrained at 95% confidence level and its observed limits are $-5.0 < \kappa_\lambda < 12.0$.

I presented results of di-Higgs searches during QCD@LHC Conference in Debrecen, Hungary in August 2017 on behalf of ATLAS and CMS Collaborations.

Physics prospects studies for the High Luminosity LHC

While the observation of Higgs boson pair production might be beyond the reach of the LHC, the upgraded LHC program called High Luminosity LHC (HL-LHC) will likely offer sufficient luminosity to do so. In 2013 I established the sensitivity to Higgs pair production in the $b\bar{b}\gamma\gamma$ final state with the ATLAS detector in the High Luminosity LHC phase. I co-edited

the related public note [6], prepared for the ECFA 2014 Conference, in which the experimental expected limits on the Higgs trilinear coupling were set for the first time. This study was based on event selection proposed in my study [1] for this channel. In April 2016, on behalf of ATLAS Collaboration, I presented prospects for measuring Higgs boson properties and observing new physics in the High Luminosity LHC at the DIS2016 conference.

Higgs boson properties

Single Higgs boson production at the LHC is about 1000 times more abundant than its pair production. Therefore, already the currently collected dataset offers sufficient statistics to investigate (subtle) Higgs properties. Such measurements may possibly lead to the discovery of new physics.

I was involved in the measurement of Higgs boson production cross-sections in gluon fusion and vector boson fusion using its decays to a pair of leptonically decaying W bosons, $h \to WW^* \to e\nu\mu\nu$ [7]. I compared signal predictions from different simulations and took part in optimising signal selection using di-lepton triggers. The results of this study confirmed the SM nature of the Higgs boson.

With the aim to improve the resolution on the Higgs coupling strengths to di-bosons and search for BSM interactions, I initiated in 2017 a novel analysis in the ATLAS experiment. Its goal was to measure Higgs boson couplings to polarised W and Z bosons in the vector boson fusion production and $h \to WW^*$ decays. Anomalous Higgs boson couplings to longitudinally polarised electroweak W and Z bosons may reveal a composite nature of the Higgs boson [8]. This study utilises signal selection and background estimation performed by the cross-section measurement of [7], on top of which it performs a differential measurement with respect to variable most sensitive to BSM effects. I was the main analyser in this study, responsible for all its ingredients. I formulated the research hypothesis, selected the optimal observable for a differential measurement, estimated theoretical uncertaitnties of the signal. I translated BSM signal parametrisation into the framework of Pseudo Observables [9], thus providing theorists valuable information to test their BSM models. In this analysis I adopted novel techniques for efficient simulations of the signal samples with different parameters and different uncertainty distributions based on Lagrangian morphing. I performed statistical analysis and determined couplings and their uncertainties using likelihood profiling.

In presenting results I am following the rules of the ATLAS Collaboration. Therefore only publicly available and approved by the collaboration results and plots are included in the presented monograph. I make two exceptions from this rule, while presenting my own studies performed with simulations and neither real data nor ATLAS software: in Chapter 4, while discussing the impact on polarisation-dependent anomalous couplings on the measured cross-section, prior to preparing ATLAS analysis and Chapter 5 where my original results not related to the ATLAS measurements are presented. For completeness, I give references to internal notes of the ATLAS collaboration, that summarise more technical aspects of analyses to which I contributed as well as preliminary studies superceded by journal publications.

1 Introduction

A unified description of electro-magnetic and weak interactions based on quantum field theory and the local $SU(2)_L \times U(1)_Y$ symmetry was a huge success of particle physics theory in the last century. The theory of electroweak interactions [10–12] correctly predicted the existence of electroweak bosons and their interactions with fermions. This theory, however, was plagued by inevitable constrain: either electroweak bosons (except for the photon) needed to be massless, or new so called "Goldstone bosons" (or "Nambu-Goldstone bosons") would emerge as a result of breaking the symmetry by the vacuum. A clever mechanism was postulated by Brout, Englert and Higgs [13–15], in which a complex scalar doublet was added to the electroweak theory. Thanks to the vacuum structure of the new field, three electroweak bosons gain mass while absorbing the "unwanted" massless modes of the Higgs field. This mechanism (called the BEH, or the Higgs mechanism) predicts additionally the emergence of a massive, elementary scalar boson, named after its postulator, the Higgs boson. This particle has been the missing piece of the electroweak theory, the ultimate proof of its correctness, sought after for almost forty years in various experiments all over the world.

It was finally discovered by the ATLAS and CMS experiments [16, 17] at the Large Hadron Collider (LHC) at CERN. Following this discovery, the properties of this new particle are studied with increasing precision by the ATLAS and CMS experiments. Yet the Higgs boson is still the least known particle of the Standard Model.

There is a striking analogy between electroweak symmetry breaking and the Meissner effect in superconductors. Superconductivity is explained in BCS theory through interactions with quantum fluid of Cooper pairs that cause magnetic forces to become short-range. In BCS theory of superconductivity Cooper pairs are composite objects – pairs of electrons exchanging phonons. Higgs boson, on the other hand, is the only known scalar particle

in the Standard Model (SM) of particle physics that within experimentally accessible range remains elementary.

Is the Higgs boson indeed elementary – in accordance with the SM predictions – or exhibits its composite nature at larger scales, $\sim$1 TeV? Is it the only particle of its kind or a part of a larger sector? In other words: is the electroweak symmetry breaking realised in Nature by the mathematically simplest mechanism possible, or is it more complex than we have originally thought? To answer these questions, the properties of the new boson and its potential are being put to experimental tests. Measurements of Higgs couplings to bosons and fermions probe local properties of the Higgs potential at the vicinity of its vacuum. The information on its global shape can be obtained from measuring Higgs self-interactions. These measurements are then confronted with both the SM and other relevant beyond Standard Model (BSM) theories to establish, which model best matches observed phenomena.

Indeed, while correctly predicting the quantum properties of particles in a broad range of energy scales, the SM falls short of being a complete theory of fundamental interactions. Instead, it is likely to be a part of a more general, yet unknown BSM theory. Therefore, measurements of Higgs boson properties and interactions may either provide a valuable confirmation of the Standard Model at $\sim$ 1 TeV scales or reveal the first hints of new phenomena, not accounted for in this theory. Various contemporary theoretical models link the properties of Higgs boson to the origin of large range of observed masses of quarks and leptons, the strength of electroweak interactions with respect to gravity as well as cosmological properties of the universe, such as early inflation or baryogenesis.

This monograph is focused on measurements that solidify the current understanding of electroweak symmetry breaking through assesing the Higgs potential and provide insight into (possible) BSM properties of the Higgs boson. In Chapter 2, I review the principles of the Higgs mechanism, focusing on its implications on the Higgs boson interactions with electroweak bosons and its self-interactions, which are the main interest of this monograph. Chapter 3 presents the ATLAS detector and the Large Hadron Collider. It recapitulates the discovery of the Higgs boson and early measurements of its properties. It also summarises, what has been known about the boson from early measurements.

This is followed by presenting the first line of research, studies of Higgs couplings to massive electroweak bosons. Measurements of these couplings are performed using WW^* fully leptonic Higgs boson decays. In Chapter 4

cross-section measurements in several Higgs boson production channels are detailed. These analyses are followed by a study constraining Higgs couplings to longitudinally and transversally polarised W and Z bosons. This last analysis sheds light onto the properties of the Higgs field degrees of freedom, the infamous "Nambu-Goldstone bosons", that through the Higgs mechanism provide longitudinal polarisations of the massive electroweak bosons.

The other part of this monograph reviews analyses aimed at observing pair production of the Higgs bosons. Chapter 5 discusses the relationship between the Higgs boson potential and its self coupling in the SM and beyond it. It presents techniques of increasing the sensitivity to measuring Higgs boson self interactions at the LHC. The findings of this chapter are further extended in Chapter 8, in which early feasibility studies in constraining the Higgs trilinear coupling at the upgraded LHC are presented. In Chapters 6 and 7 Higgs pair searches at Run 1 and 2 of the LHC are presented. Both chapters outline analysis techniques specific to various di-Higgs decay channels, with a focus on their statistical combinations. In this way, the constraints on the Higgs trilinear self-coupling, presented in Chapter 7 are comparable with results expected with much larger dataset in Chapter 8.

Conventions In the following I adopt a short-hand notation for naming particles and anti-particles, skipping their charges. This refers mainly to processes involving a pair production of a particle and its anti-particle. For example, I denote Higgs boson decays to a pair of W^+W^- bosons as $h \to WW^*$, rather than "$h \to W^+W^{-*}$ and $h \to W^-W^{+*}$" , or di-Higgs decays by $hh \to \tau\tau bb$ instead of $hh \to \tau^+\tau^- b\bar{b}$. Similarly, I refer to a "top quark pair" rather than "top–anti-top pair". This is because particles and anti-particles are treated in the same way in experimental identification (e.g. identification efficiency of b-quarks and $\bar{b}$-quarks is assumed equal) and often kinematical effects (such as distinguishing that one W boson is off its mass shell, W^*) are more relevant than particles' charges. On the other hand, whenever a particle's charge is relevant, this information is given, e.g. $W^\pm W^\pm$ production, or W^+Z^0 production.

Additionally, l, or light lepton refers to either an electron or a muon (and their anti-particles). The heaviest lepton, τ, is always discussed separately, because its short lifetime requires the usage of different reconstruction techniques.

The natural units are used where proton carries a positive unit of charge

and the speed of light $c = 1$. Hence, one electronvolt (eV) is 1.602×10^{-19} J.

2 Electroweak symmetry breaking in the Standard Model

In the following I briefly present Glashow-Weinberg-Salam electroweak lagrangian of the Standard Model (SM). I discuss its properties and in particular constrains on the masses of gauge fields its symmetry structure imposes. The Brout-Englert-Higgs (BEH) mechanism [13–15] of generating these nonzero masses by spontaneously breaking the local symmetry of the gauge group is shown. This is done first using a simplified example of breaking $U(1)$ symmetry, and followed by a complete picture, including field mixing and their non-abelian couplings. The emphasis is put on the Higgs boson potential and on interactions between gauge fields and the Higgs fields. These ingredients of the Standard Model will be put to experimental tests in later chapters of this monograph.

2.1 The electroweak sector of the SM

Electroweak interactions respect Lorentz invariance and a local gauge invariance and respect the $SU(2)_L \times U(1)_Y$ symmetry group. The subscript L means that only the left-handed fermion fields are doublets of the $SU(2)$ group, while right-handed ones form singlets. In other words, only left-handed components of lepton and quark fields participate in the weak interactions. Similarly, only electrically charged lepton and quark fields (of both left and right handedness) participate in electromagnetic interactions. Weak and electromagnetic interactions are mediated by four bosonic fields $W^{1\mu}, W^{2\mu}, W^{3\mu}$ and B^{μ}. The great success of a field theory description of electromagnetic interactions lies in their unified description in a single la-

grangian:

$$\begin{aligned}\mathcal{L}_{\text{el-weak}} &= i\bar{\psi}\gamma_\mu D^\mu\psi - \frac{1}{2}g\bar{\psi}\gamma^\mu\sigma_i W^i_\mu - \frac{1}{2}g'Y\bar{\psi}\gamma^\mu B_\mu\psi \\ &\quad - \frac{1}{4}W^a_{\mu\nu}W^{\mu\nu}_a - \frac{1}{4}B^{\mu\nu}B_{\mu\nu},\end{aligned} \tag{2.1}$$

where the first line corresponds to interactions among fermions and bosons and the second one to inter-bosonic interactions. The couplings g and g' correspond to coupling strengths of $SU(2)_L$ and $U(1)$ symmetries, respectively and σ_i denotes Pauli matrices. In the following, only the gauge boson sector of the SM lagrangian is considered:

$$\mathcal{L}_{\text{gauge}} = -\frac{1}{4}W^a_{\mu\nu}W^{\mu\nu}_a - \frac{1}{4}B^{\mu\nu}B_{\mu\nu}, \tag{2.2}$$

where the field strength tensors are defined by

$$\begin{aligned}W^a_{\mu\nu} &= D_\mu W^a_\nu - D_\nu W^a_\mu + g\epsilon^{abc}W^b_\mu W^c_\nu, \\ B_{\mu\nu} &= D_\mu B_\nu - D_\nu B_\mu\end{aligned} \tag{2.3}$$

and the covariant derivative has the form:

$$\begin{aligned}D_\mu &= \partial_\mu - \frac{i}{2}g\sigma_i W^i_\mu(x) - \frac{i}{2}g'Y B_\mu(x) \\ &= \partial_\mu - \frac{i}{2}\begin{pmatrix} gW^3_\mu + g'B_\mu & g(W^1_\mu - W^2_\mu) \\ g(W^1_\mu + W^2_\mu) & -gW^3_\mu + g'B_\mu \end{pmatrix}.\end{aligned} \tag{2.4}$$

This form of the covariant derivative ensures that the electroweak interactions are invariant under the transformation

$$U(x) = \exp\left(i\frac{Y}{2}\alpha(x) + iI\sum_{i=1}^{3}\sigma_i\beta_i(x)\right) \tag{2.5}$$

called also the local $SU(2)_L \times U(1)_Y$ gauge invariance [10–12]. I is the weak isospin and Y the hypercharge related with the electric charge Q and isospin through $Y = 2(Q - I_3)$. Functions $\alpha(x)$ and $\beta_i(x)$ are local functions.

Any addition to the Lagrangian (2.2) of a term quadratic in the fields, such as $mB^\mu B_\mu$, would violate local gauge invariance of (2.5). Therefore, the Glashow electroweak theory predicts that the gauge bosons are massless. This feature stands in contrast to the observations. Weak interactions have

finite range and should therefore be mediated by massive bosons. The direct discovery of electroweak bosons at CERN later confirmed their masses are $\mathcal{O}(100)$ GeV.

To overcome this obstacle in the electroweak theory, a mechanism of electroweak spontaneous symmetry breaking was introduced by [13–15, 18]. The Brout-Englert-Higgs (BEH) mechanism predicts the existence of a new field ϕ:

$$\begin{aligned}\mathcal{L}_{\text{gauge-Higgs}} &= \mathcal{L}_{\text{gauge}} + \mathcal{L}_{\text{Higgs}} \\ &= \mathcal{L}_{\text{gauge}} + (D_\mu\phi)^\dagger(D^\mu\phi) - V_\phi\end{aligned} \tag{2.6}$$

The potential of the Higgs field has the form:

$$V(|\phi|^2) = \mu^2|\phi|^2 + \lambda|\phi|^4, \tag{2.7}$$

where $\lambda > 0$ and $\mu^2 < 0$. This potential depends on $|\phi|^2$, which is motivated by gauge invariance. The rank four polynomial gives the simplest expression for a renormalisable potential. The remarkable features of the Higgs potential is that the quasi-mass term μ^2 is negative and its minimum value, the Higgs vacuum expectation value (VEV, v), is non-zero $v^2 = -\mu^2/\lambda$.

The notation of (2.6), may be slightly misleading. The $\mathcal{L}_{\text{Higgs}}$ term denoting all functional dependence on the Higgs field in the electroweak lagrangian, but depends additionally on the gauge fields through the covariant derivative. The term $\mathcal{L}_{\text{gauge}}$, on the other hand, encapsulates the dependence on the gauge fields, and not on the Higgs field. The reason for extracting $\mathcal{L}_{\text{Higgs}}$ is that Higgs-gauge fields interactions present in the kinetic term of the scalar field are the essence of the BEH mechanism. In the following two sections the BEH mechanism will be outlined first in one dimension, by demonstrating breaking of the $U(1)$ symmetry. These considerations will be followed by reminding the symmetry breaking in the full $SU(2)_L \times U(1)_Y$ gauge group, realised by 2 complex scalar fields, in section 2.3.

2.2 The BEH mechanism in $U(1)$

In this simplification we consider only a single scalar field ϕ to illustrate how a single gauge boson vector field B_μ acquires mass. By omitting other gauge fields for a moment, the scheme of electroweak symmetry breaking is not blurred by field mixing and their non-abelian couplings.[1]

[1]Similar approach can be found for example in [19].

The lagrangian of this toy model, which would correspond to electromagnetism with a massive photon, is given by

$$\mathcal{L} = -\frac{1}{4}B^{\mu\nu}B_{\mu\nu} + (D_\mu\phi)^*(D^\mu\phi) - V_\phi \tag{2.8}$$

where the covariant derivative ensuring a local U(1) symmetry of the theory is given by

$$D^\mu = \partial^\mu - igB^\mu. \tag{2.9}$$

We have

$$(D_\mu\phi)^*(D^\mu\phi) = (\partial_\mu + igB_\mu)\phi^*(\partial^\mu - igB^\mu)\phi \tag{2.10}$$

and V is the Higgs potential

$$V_\phi = \mu^2|\phi|^2 + \lambda|\phi|^4. \tag{2.11}$$

The Higgs field can be expanded around its VEV $v = \sqrt{\frac{-\mu^2}{\lambda}}$ as

$$\phi(x) = \frac{1}{\sqrt{2}}\left(v + \eta(x) + i\xi(x)\right), \tag{2.12}$$

where $\eta(x)$ and $\xi(x)$ are real fields corresponding to small excitations in the radial and in the tangent directions around the vacuum, respectively. In order to explicitly show, how these two degrees of the Higgs field interact with the gauge field, we inspect the kinetic term of the scalar field:

$$\begin{aligned}&(D_\mu\phi)^*(D^\mu\phi) = \\ &\underbrace{\frac{1}{2}(\partial_\mu\eta)(\partial^\mu\eta) - \lambda v^2\eta^2}_{\text{massive field}} \quad + \quad \underbrace{\frac{1}{2}(\partial_\mu\xi)(\partial^\mu\xi)}_{\text{massless field}} + \frac{1}{2}g^2v^2B_\mu B^\mu + gvB_\mu\partial^\mu\xi + \cdots .\end{aligned} \tag{2.13}$$

Let us examine each term of the eq. (2.13). The spontaneous symmetry breaking gives rise to the quadratic terms in $\eta(x)$. Out of two real fields in (2.12), $\eta(x)$ is massive and $\xi(x)$ remains massless. The mass of the field $\eta(x)$ can be read out from (2.13): $\frac{1}{2}m_h^2\eta^2(x) = \frac{1}{2}\cdot 2\lambda v^2\eta^2(x)$. The term $gvB_\mu\partial^\mu\xi$ in eq.(2.13) is unphysical, but can be removed from the lagrangian by a redefinition of a gauge field:

$$B'_\mu \equiv B_\mu + \frac{1}{gv}\partial_\mu\xi. \tag{2.14}$$

In this way:

$$\frac{1}{2}(\partial_\mu\xi)(\partial^\mu\xi) + \frac{1}{2}g^2v^2B_\mu B^\mu + gvB_\mu\partial^\mu\xi = \frac{1}{2}g^2v^2\left|B_\mu + \frac{1}{gv}\partial_\mu\xi\right|^2 \to \frac{1}{2}g^2v^2B'^2_\mu. \tag{2.15}$$

This gauge redefinition will not be needed (nor possible), should the Higgs VEV $v = 0$. Transformation eq. (2.14) does not change the field strength tensor $B^{\mu\nu}B_{\mu\nu}$. The transformation of the Higgs field under eq. (2.14) looks as follows:

$$\begin{aligned}\phi(x) \to \phi'(x) &= \exp\left[-ig\frac{\xi(x)}{gv}\right]\phi(x) = \exp\left[-i\frac{\xi(x)}{v}\right]\frac{1}{\sqrt{2}}(v+\eta(x)+i\xi(x)) \\ &= \exp\left[-i\frac{\xi(x)}{v}\right]\frac{1}{\sqrt{2}}\left[(v+\eta(x))\exp\left[i\frac{\xi(x)}{v}\right] + \mathcal{O}(\xi(x)^2)\right] \\ &\simeq \frac{1}{\sqrt{2}}(v+\eta(x)).\end{aligned} \tag{2.16}$$

After the gauge redefinition (2.14) the massless field ξ is "rotated out" from the scalar field ϕ, and completely vanishes from the lagrangian. The Higgs field now becomes real. The lagrangian after symmetry breaking, $\mathcal{L}_{SB}$, has the form:

$$\mathcal{L} \to \mathcal{L}_{SB} = -\frac{1}{4}B'^{\mu\nu}B'_{\mu\nu} + \frac{1}{2}g^2v^2B'^2_\mu + \frac{1}{2}(\partial_\mu\eta)(\partial^\mu\eta) - \lambda v^2\eta^2 \tag{2.17}$$

Spontaneous symmetry breaking gives rise to a massless boson ξ, as stated in the Goldstone theorem: "If there is a continuous symmetry transformation under which the Lagrangian is invariant, then either the vacuum state is also invariant under the transformation, or there must exist spinless particles of zero mass." The existence of these "unwanted Goldstone bosons" [11] was perceived as a central problem to the electroweak theory, because they were never detected. The BEH mechanism demonstrates that these massless bosons are absorbed by gauge fields, giving rise to their masses. In the physical gauge (2.14) all fields are physical.

2.3 The BEH mechanism in the $SU(2)_L \times U(1)_Y$

We now consider the electroweak lagrangian of (2.2) featuring $SU(2)_L \times U(1)_Y$ local symmetry.

The Higgs sector in the SM consists of two complex scalar fields (an isospin doublet):

$$\phi = \begin{pmatrix} \phi^+ \\ \phi^0 \end{pmatrix} = \frac{1}{\sqrt{2}} \begin{pmatrix} \phi_1 + i\phi_2 \\ \phi_3 + i\phi_4 \end{pmatrix}. \tag{2.18}$$

The Higgs field can be expanded around its vacuum like in the previous section.

$$\phi_0(x) = \frac{1}{\sqrt{2}} \exp^{i\xi^a T^a} \begin{pmatrix} 0 \\ v + h(x) \end{pmatrix}, \tag{2.19}$$

where h represents its real component, and three other fields in eq. (2.18) will lead to 3 Nambu-Goldstone bosons ξ^a. Like in eq. (2.16), the unitarity transformation "rotates them out". Therefore, in a unitarity gauge, ϕ_0 can be reduced to:

$$\phi_0(x) = \frac{1}{\sqrt{2}} \begin{pmatrix} 0 \\ v + h(x) \end{pmatrix}. \tag{2.20}$$

$$\begin{aligned} (D_\mu \phi_0)^\dagger (D_\mu \phi_0) =& \frac{1}{2}(\partial_\mu h)(\partial^\mu h) \\ &+ \frac{1}{8} g^2 (W^1_\mu + iW^2_\mu)(W^{1\mu} - iW^{2\mu})(v+h)^2 \\ &+ \frac{1}{8}(gW^3_\mu - g' B_\mu)(gW^{3\mu} - g' B^\mu)(v+h)^2. \end{aligned} \tag{2.21}$$

The kinetic Higgs term $(D_\mu \phi_0)^\dagger (D^\mu \phi_0)$ gives rise to mass terms for gauge bosons. The physical bosons spectra consist of four electroweak bosons that result from mixing of the gauge fields $W^{1\mu}, W^{2\mu}, W^{3\mu}$ and B^μ.

In order to obtain physical bosons, the following transformations are performed:

$$W^\pm_\mu = \frac{1}{\sqrt{2}}(W^1_\mu \mp iW^2_\mu). \tag{2.22}$$

The fields $W^\pm_\mu$ are electrically charged and correspond to physical particles. The unitarity transformation of W^3_μ and B_μ results in two fields: Z_μ

and γ_μ, that are electrically neutral:

$$\begin{aligned} Z_\mu &= \frac{g}{\sqrt{g^2+g'^2}} W^3_\mu - \frac{g'}{\sqrt{g^2+g'^2}} B_\mu \\ \gamma_\mu &= \frac{g'}{\sqrt{g^2+g'^2}} W^3_\mu + \frac{g}{\sqrt{g^2+g'^2}} B_\mu. \end{aligned} \tag{2.23}$$

Typically the above coupling combinations are expressed in terms of the weak mixing angle (called also Weinberg mixing angle) θ_W:

$$\cos\theta_W = \frac{g}{\sqrt{g^2+g'^2}}, \quad \sin\theta_W = \frac{g'}{\sqrt{g^2+g'^2}}. \tag{2.24}$$

After these transformations the quadratic terms:

$$\frac{1}{8} v^2 g^2 (W^+_\mu W^{+\mu} + W^-_\mu W^{-\mu}) + \frac{1}{8} v^2 (g^2+g'^2) Z_\mu Z^\mu \tag{2.25}$$

give masses of the charged and neutral bosons:

$$M^2_{W^+} = M^2_{W^-} = \frac{1}{4} g^2 v^2, \quad M^2_Z = \frac{1}{4}(g^2+g'^2) v^2, \quad M_\gamma = 0. \tag{2.26}$$

The photon remains massless and the masses of W and Z bosons are related by custodial symmetry (approximate SO(4) symmetry of the Higgs sector):

$$\cos^2\theta_W M^2_Z = M^2_W. \tag{2.27}$$

The $SU(2)_L \times U(1)_Y$ symmetry is broken to the $U(1)$ symmetry. The remaining $U(1)$ symmetry means that the photon remains massless. The W and Z bosons emerging from the original $W^{1\mu}, W^{2\mu}, W^{3\mu}$ and B^μ fields gain masses by absorbing three out of four degrees of freedom of the Higgs field.

In section 4.10 we will explore further differences between massive gauge bosons and a photon.

2.4 Higgs boson couplings to W^+, W^-, Z and photon

The terms of (2.21), that are trilinear and quartic polynomials in the gauge fields:

$$\frac{1}{4} g^2 W_\mu W^\mu (v+h)^2 = \frac{1}{4} g^2 v^2 W_\mu W^\mu + \frac{1}{2} g^2 v h W_\mu W^\mu + \frac{1}{4} g^2 h^2 W_\mu W^\mu \tag{2.28}$$

results in triple and quartic Higgs-W boson couplings:

$$g_{hWW} = \frac{1}{2}g^2 v = gM_W \tag{2.29}$$

and

$$g_{hhWW} = \frac{1}{4}g^2. \tag{2.30}$$

The lagrangian features no terms involving both Higgs boson and the photon. Consequently, all tree-level photon couplings to the Higgs boson are 0. The Higgs boson can decay to a pair of photons, but this process is mediated by virtual quantum effects resulting in the branching ratio $Br(h \to \gamma\gamma) = 0.2\%$.

2.5 Polarisation states of electroweak bosons

A free spin-1 massive particle B_μ fulfils the equation:

$$(\Box + m^2)B^\mu - \partial^\mu(\partial_\mu B^\nu) = 0, \Leftrightarrow (\partial_\mu B^\mu) = 0 \tag{2.31}$$

with the d'Alembert operator $\Box = \partial_\mu \partial^\mu$. This equation is satisfied by plane waves solution in the form

$$\Box \exp[-ipx] = -m^2 \exp[-ipx] \Rightarrow B = e^\mu \exp[-ipx] \tag{2.32}$$

with p being the particle's four-momentum. Inserting this solution into equation (2.31), gives the constraint:

$$p_\mu e^\mu = 0. \tag{2.33}$$

This constraint results in three independent polarisation states of massive electroweak bosons, that can be written as:

$$B^\mu = e^\mu_\lambda \exp[-ipx] = e^\mu_\lambda \exp[-i(\overrightarrow{p} \cdot \overrightarrow{x} - Et)]. \tag{2.34}$$

Decomposing e^μ into Carthesian coordinates gives three linear polarisation states:

$$e^\mu_x = (0,1,0,0); \quad e^\mu_y = (0,0,1,0); \quad e^\mu_z = (0,0,0,1). \tag{2.35}$$

Alternatively, for any particle with momentum p^μ the decomposition can be made into two transverse polarisations

$$e^\mu_- = \frac{1}{\sqrt{2}}(0,1,-i,0), \quad e^\mu_+ = -\frac{1}{\sqrt{2}}(0,1,i,0), \tag{2.36}$$

and the longitudinal one:

$$e_L^\mu = \frac{1}{m}\left(p_z, 0, 0, E\right). \tag{2.37}$$

The above decomposition has the advantage that particle's helicities, defined as the projection of a particle's spin onto its direction of motion, corresponds to +1, 0, –1 helicities for e_+^μ, e_L^μ, e_-^μ.

These polarisation vectors fulfill the sum rule

$$\sum e_\lambda^{*\mu} e_\lambda^\nu = -g^{\mu\nu} + \frac{p^\mu p^\nu}{m^2}. \tag{2.38}$$

In case of the (massless) photon, longitudinal polarisation can be removed by fixing gauge to the Coulomb gauge $\overrightarrow{\epsilon} \cdot \overrightarrow{q} = 0$. Unlike the photon, massive electroweak bosons have exhausted their gauge freedom by a gauge fixing transformation of equation (2.14). In this way "eating massless Nambu-Goldstone bosons", originating from the complex components of the Higgs field, results in unremovable longitudinal polarisations.

The above polarisations refer to on-shell particles. In both Higgs production and in its decay to WW^* , discussed in Chapter 4, at least one electroweak boson is off-shell. The polarisations of off-shell particles can be defined, following Ref [20], by defining the transverse and longitudinal parts of the boson fields in unitary gauge, V, as:

$$V_T^\mu = \mathbb{P}_\nu^\mu V^\nu; \qquad V_L^\mu = (\mathbb{1} - \mathbb{P})_\nu^\mu V^\nu, \tag{2.39}$$

where projection operator $\mathbb{P}_\nu^\mu$ is given by

$$\mathbb{P}^{0\mu} = \mathbb{P}^{\nu 0} = 0; \qquad \mathbb{P}^{ij} = \delta_{ij} - \frac{\vec{p}^i \vec{p}^j}{\vec{p}^2}, i, j = 1, 2, 3. \tag{2.40}$$

Polarisations are not Lorentz invariant: a boost of a particle's momentum can cause mixing of its transverse and longitudinal polarisations. For the purpose of discussed measurement, polarisations are defined in the Higgs rest frame.

Polarisation has measurable effects on the kinematics of the boson's decay products and is typically measured using angular variables. The example of WW^* decays is given in Section 4.1.

2.6 Production cross-sections and branching ratios of the Higgs boson

The SM predictions for Higgs boson production and decay rates at the LHC are illustrated in Figure 2.1. The largest Higgs boson production mechanism in proton-proton collisions is through gluon fusion. Its most precise computations to date are done at next-to-next-to-next-to leading order in QCD and combined with next-to leading order in QED [21]. The cross-section for this process at centre of mass energy of 13 TeV equals $48.58\ ^{+2.22}_{-3.27}$(theory) ± 1.56(PDF+α_S) *pb*. The second largest production process is vector boson fusion, followed by associated production with W, Z, a pair of b quarks, top quarks, and a single top quark.

The predictions for branching fractions depend on the Higgs boson mass. The total decay width of the Higgs boson is ~ 4 MeV, which means that it is extremely short-lived. Its estimated lifetime is of the order of 10^{-22}s, after which the boson decays to other particles. The largest branching ratios for the SM Higgs boson of a mass around 125 GeV are displayed in the right plot in Figure 2.1. The dominant decay chanel is to a pair of b quarks (0.5824 $\pm$ 0.65% fraction of all decays), followed by a pair of W bosons (0.2137 $\pm$ 0.99%), a pair of gluons (0.0818$\pm$ 3.41%), τ leptons (0.06272 $\pm$ 1.17%), Z bosons (0.02619 $\pm$ 0.99%), two photons (0.00227 $\pm$ 1.73%). Should the Higgs boson be heavier than 350 GeV, it would predominantly decay to a pair of top quarks.

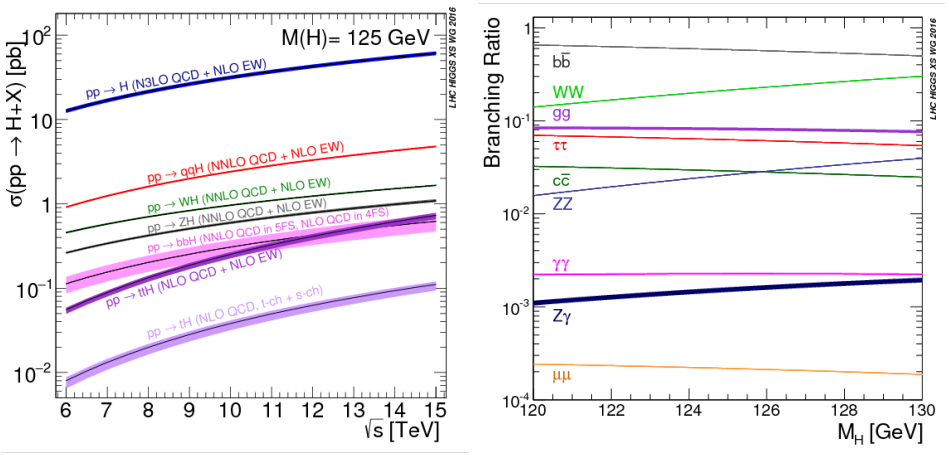

Figure 2.1: Left plot: SM predictions for Higgs boson production channels at the LHC as a function of centre-of-mass energy $\sqrt{s}$. Right plot: Higgs boson branching ratios as a function of its mass. Theoretical uncertainties are indicated by line widths. Figure from [2].

3 Higgs boson at the LHC

3.1 The Large Hadron Collider

The Large Hadron Collider (LHC), built in tunnel ring of a 27-kilometre circumference, is the largest particle physics accelerator. It also holds the record of centre-of-mass energy of colliding protons, which is 13.6 TeV[1].

Protons are obtained by ionising hydrogen atoms. Before being injected to the LHC, they enter a system of accelerators, that step-wise increase their energy. Protons are first accelerated in a linear accelerator Linac-2 to 50 MeV. This is followed by a series of circular accelerators: the Proton Synchrotron Booster (PSB), the Proton Synchrotron (PS) and the Super Proton Synchrotron (SPS), that increase the energy of protons to 1.4 GeV, 25 GeV and 450 GeV, respectively.

Upon being injected to the LHC, protons are localised in bunches forming two beams travelling in opposite directions in two tubes kept at high vacuum, called the beam pipes. The design number of protons in one bunch is 1.15×10^{11} and each beam is composed of up to 2808 bunches.

In order to boost the energy of the particles to the design value of 7 TeV per bunch, the LHC features superconducting magnets with a number of accelerating structures along the way. Strong magnetic field maintained by superconducting electromagnets bends the particles around the accelerator ring and accelerates them. The electromagnets are built from coils of superconducting cables, thus conducting electricity without resistance or loss of energy. The LHC magnets need therefore to be cooled down to -271.3°C, a temperature close to the absolute 0 K. This is achieved using liquid helium.

[1]In addition to protons, the LHC is designed to accelerate and collide heavy ions, such as lead nuclei with each other or with protons. For the purpose of discussion the Higgs boson properties, this monograph is restricted to proton-proton collisions.

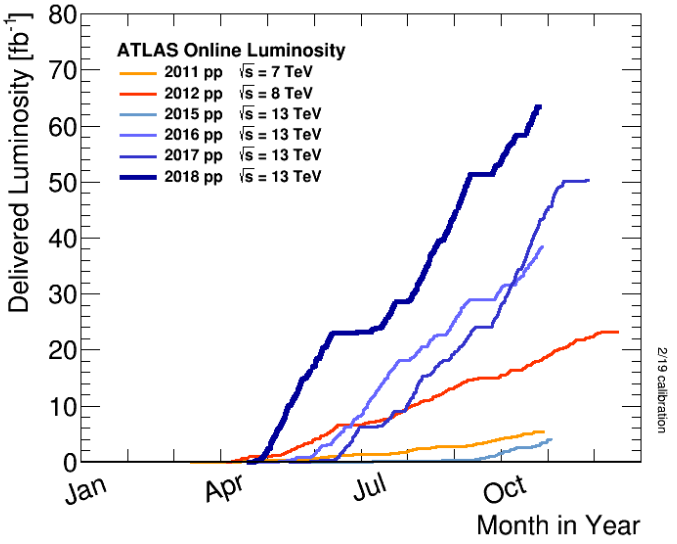

Figure 3.1: Cumulative luminosity versus day delivered to ATLAS during data-taking periods for high energy p-p collisions. Figures from Ref. [22]

Beams of particles from the LHC collide at the centres of four detectors built around its circumference: ATLAS, CMS, LHCb and ALICE.

The design luminosity of the LHC is 10^{34}cm^{-2}. The first collision at the LHC took place at the end of March 2010 with instantenuous luminosity 2×10^{27} cm^{-2} s^{-1}. This value has gradually been increasing. Cumulative luminosity delivered to ATLAS during data-taking periods described in this monograph is displayed in Fig.3.1.

3.1.1 Data taking periods

The LHC has been designed to collide protons at a maximum center-of-mass energy of 14 TeV. Its nominal energy, however, has never yet been reached. Instead, the accelerator has been operating in several periods, lasting a couple of years, during which the center-of-mass energy of colliding protons, $\sqrt{s}$, has been increased from 7 TeV to 13.6 TeV. The LHC started operations in 2010. In 2010 and 2011 $\sqrt{s} = 7$ TeV was reached, followed by $\sqrt{s} = 8$ TeV in 2012. This data taking period is referred to as Run 1. The so-called Run 2 took place in years 2015 – 2018. The centre-of-mass energy of colliding protons was substantially increased, reaching 13 TeV. The Run 3, ongoing since 2022,

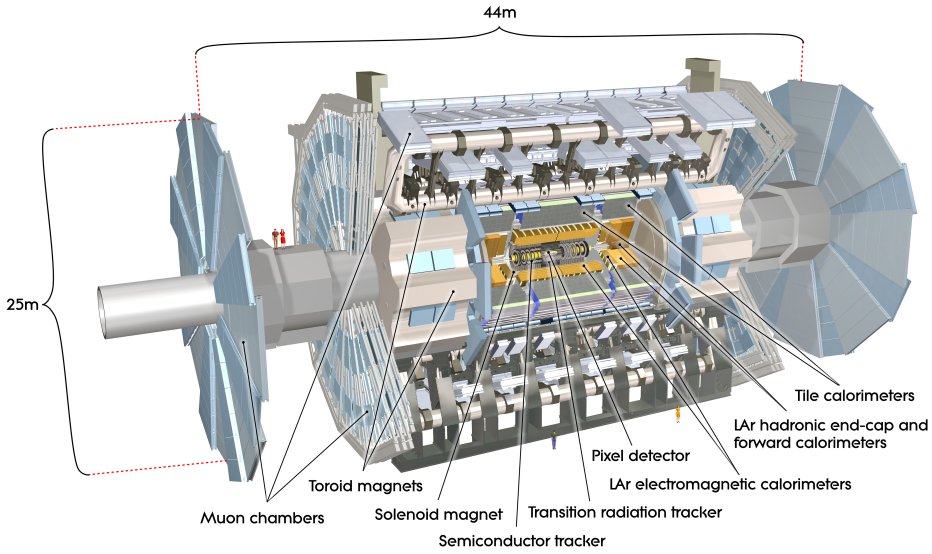

Figure 3.2: Illustration of the ATLAS detector. Picture from Ref. [23]

marks another energy increase to $\sqrt{s} = 13.6$ TeV. Data-taking periods are separated with technical stops of one to two years, devoted to accelerator and detector upgrades and maintenance. After the completion of Run 3, the LHC is going to be upgraded in order to reach the energy of 14 TeV and larger collision rates. This phase is called High Luminosity LHC (HL-LHC). Its planned operational conditions will be described in Chapter 8.

Analyses described in this monograph have been conducted using Run 1 and Run 2 data collected by the ATLAS detector.

3.2 The ATLAS detector

The ATLAS (A Toroidal Lhc ApparatuS) detector, depicted in Fig. 3.2, is the largest detector ever constructed for a particle collider. It has a shape of a cylinder lying on its side, 46 metres long and of a diameter of 25 metres. It is equipped with more than 100 million electronics channels that record the particles produced by the collisions. The total weight of the detector is 7000 tonnes. Together with the CMS (Compact Muon Solenoid) detector, ATLAS was designed as a general-purpose detector, capable of identifying particles

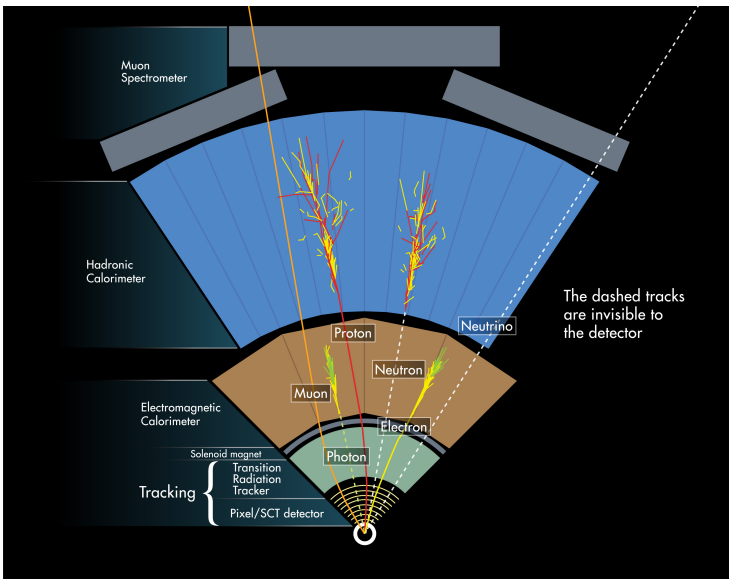

Figure 3.3: A schematic illustration of identification of particles in the ATLAS subdetectors, shown in a transverse view of its quadrant. Picture from Ref. [24]

in a broad range of masses and energies. The architecture of the ATLAS detector is forward-backward symmetric, which assures the same accuracy of particles traversing it in opposite directions. It consists of several subdetectors, specialised for measuring different properties of particles. Starting from the LHC beam pipe and going outwards: the Inner Detector (ID), measures tracks of charged particles and enables the reconstruction of decay vertices of short-lived particles, the Electromagnetic Calorimeter (ECal) and the Hadronic Calorimeter (HCal) measure energy deposits of streams of particles, and the Muon Spectrometer (MS) enables reconstruction of muon tracks. These complementary functionalities are schematically depicted in Fig. 3.3.

All reconstructed particles momenta are defined in the right-handed coordinate system used by ATLAS. The origin of this coordinate system is located at the nominal interaction point (IP) in the centre of the detector and the z-axis runs along the beam pipe. The x-axis points from the IP to the centre of the LHC ring, and the y-axis points upwards. Cylindrical coordinates (r, θ, ϕ) are used in the plane perpendicular to the beam (also called a transverse plane), r being the radius, θ the polar angle and ϕ the

azimuthal angle around the beam pipe. The pseudorapidity η is defined as $\eta = -\ln\tan(\theta/2)$. Angular distance between reconstructed objects, ΔR , is computed using $\Delta R \equiv \sqrt{(\Delta\eta)^2 + (\Delta\phi)^2}$.

The ATLAS **magnet system** consists of the superconducting Barrel Toroid and two Endcap Toroids and a central Solenoid magnet. The Barrel Toroid is composed of eight superconducting magnet coils, each 25-m long, placed radially and symetrically around the beam axis. Together with the Solenoid they form a cylinder around the beam pipe through the centre of the ATLAS detector. The magnetic field produced by the central solenoid is 2 T. It bends the paths of charged particles produced in collisions at the LHC, depending on their masses and energies, thus enabling their identification.

3.2.1 Inner Detector

ATLAS Inner Detector features three subdetectors: a silicon Pixel and microstrip (SCT) trackers, complemented with the transition radiation tracker (TRT). The cut-away view over all sub-systems is shown in Figure 3.4. Inner detector extends radially from the radius of 36 mm (inside which the beam pipe is located) to 2.1 m and has a total length of 6.2 m, providing pseudo-rapidity coverage of $|\eta| < 2.5$. The Pixel and SCT detectors in the barrel region are shaped as concentric cylinders (three and four, respectively) around the beam axis. In each end-cap region they are mounted on disks perpendicular to the beam axis (three for Pixel and nine for the SCT). The outermost subdetector, TRT, is made up with straw tubes grouped in 73 planes in the barrel and 160 in end-caps. The TRT only provides information on the radial coordinate R and azimuthal angle ϕ. In the barrel region, the straws are parallel to the beam axis and are 144 cm long, while in the end-cap region, they are arranged radially in wheels and are 37 cm long. Inner detector is designed to cope with large track density: as many as $\sim 10^3$ particle tracks are expected from proton collisions every 25 ns. In order to provide robust reconstruction of multiple interaction vertices and particles' momenta, each subdetector is made of very granular modules: each pixel size is 50 μm $\times$ 400 μm, SCT sensors have a strip pitch of 80μm, straw tubes of the TRT have diameters of 4 mm and an intrinsic accuracy of 130 μm per straw. In 2014 inner detector was supplemented with an additional subdetector, the insertable b-layer (IBL), placed closest to the beam pipe. This additional pixel layer improves the determination of the track impact parameters and provides vertexing information crucial for precise reconstruction of

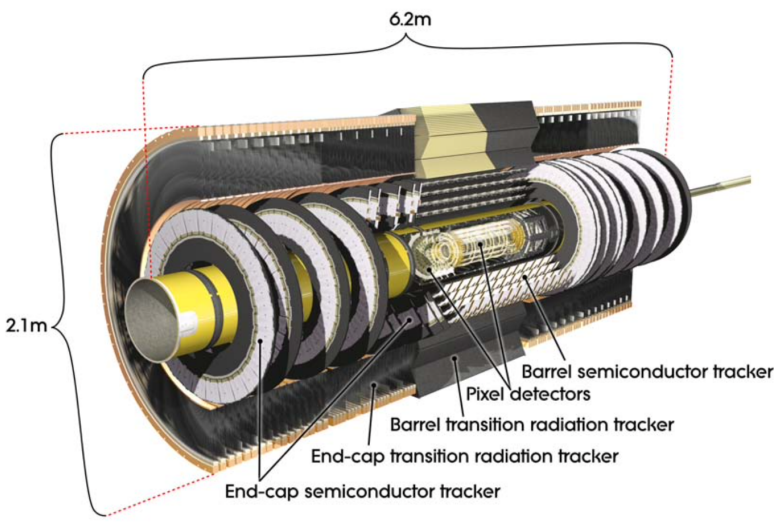

Figure 3.4: Schematic view of ATLAS inner detector. Picture from Ref. [25]

short-lived particles, such as b-quarks.

Tracks traversing the barrel region cross eight strip layers of the SCT and ∼30 in the TRT. Their reconstruction follows a multi-staged process. In the pre-processing, information from Pixel and SCT hits are translated into clusters and phase space points and TRT timing information is converted into drift circles. Track fitting is performed by first constructing track seeds using only data from the Pixel and the first SCT layer, thus exploiting the information from the most granular subdetectors. These initial seeds are extended by taking into account all SCT layers, forming track candidates. At this stage ambiguities in attributing clusters to track candidatess are resolved and fake tracks are removed. The remaining track candidates are then extended to the TRT region, and the association with drift-circle information enables resolving the left-right ambiguities. At the post-processing stage primary vertices are reconstructed. They represent hard interactions between proton constituents in colliding bunches. This procedure is followed by the reconstruction of photon conversion vertices and of secondary vertices in each collision event.

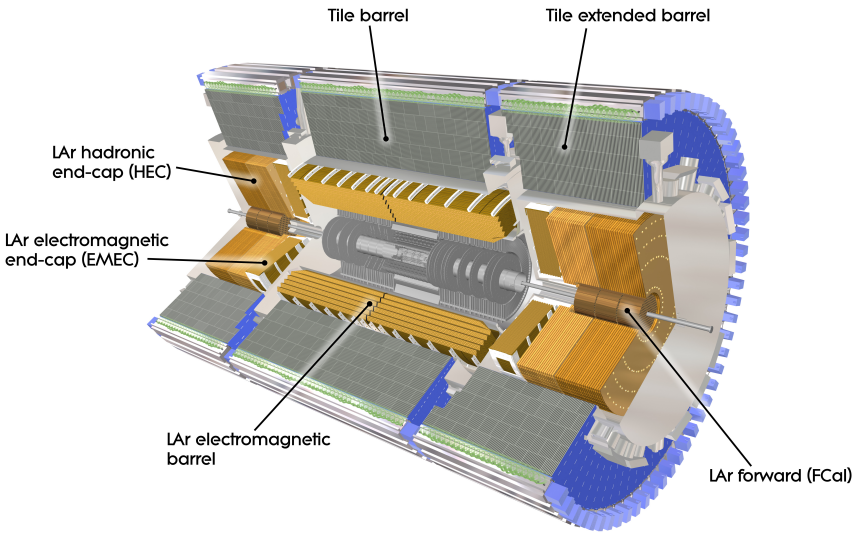

Figure 3.5: Illustration of ATLAS Calorimeters. Picture from Ref. [26]

3.2.2 Calorimeters

The purpose of calorimeters is to measure energies and positions of showers of particles (as shown in Fig.3.3). Electromagnetic showers are initiated by either an electron (positron) or a photon and deposit their energy in the electromagnetic calorimeter. Hadronic showers originate from QCD radiation off protons, neutrons, or their constituents: quarks and gluons and are called jets. They deposit energy further away from the interaction point than electromagnetic showers, which dictates the relative layout of the two calorimeter subsystems.

The calorimeters used by ATLAS are composed of alternating layers of an active sensing material and an energy absorber. This design, called a sampling calorimeter, enables measuring energies of entire electromagnetic and hadronic showers by computing it from the sum of the energy deposits in each sampling layer. In order to provide precise measurements, calorimeter measurements of both energy and positions of showers are calibrated using corrections, which are derived from Monte Carlo simulations and validated using test beam data. From precise measurements of energies and positions of jets and electromagnetic objects, the so called missing transverse energy

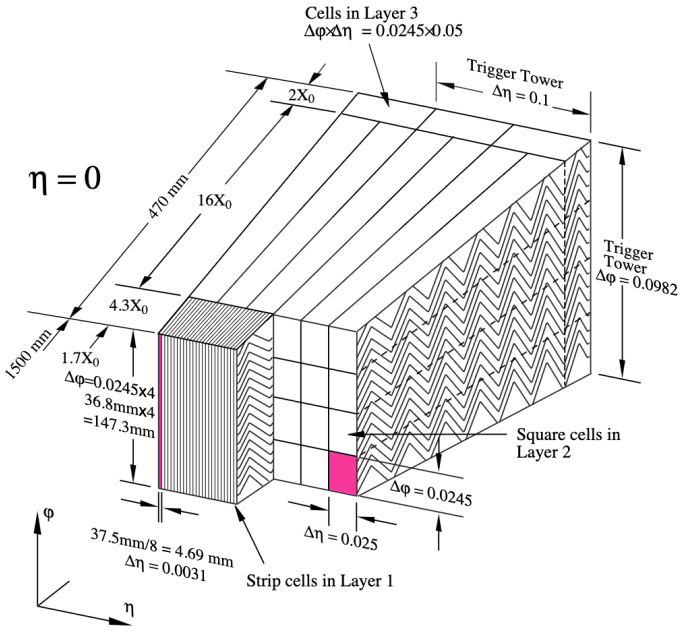

Figure 3.6: Illustration of ATLAS EM calorimeter module with accordion shape of lead absorbers and electrodes. Picture from Ref. [27]

is inferred. This quantity, representing the momentum imbalance in every collision event, is used to measure momenta of weakly interacting neutral particles, such as SM neutrinos, or other hypothesised objects in BSM theories.

ATLAS calorimeters are composed of two subsystems, depicted in Figure 3.5: the electromagnetic calorimeter (ECAL), arranged immediately outside the TRT, and the hadronic calorimeter (HCAL), situated outside of the ECAL.

The electromagnetic calorimeter covers the pseudorapidity range $|\eta| < 3.2$, with precision measurements restricted to the central region, corresponding to $|\eta| < 2.5$. The calorimeter is installed in three cryostats: one containing the barrel part in the region $|\eta| < 1.475$, and two which each contain the two parts of the end-cap ($1.375 < |\eta| < 3.2$). Owing to accordion geometry of lead absorbers and electrodes of the barrel and endcap calorimeters, depicted in Figure 3.6, complete azimuthal angle symmetry is maintained in its coverage, without cracks.

The total thickness of the calorimeter is greater than 22 radiation lengths in the barrel and greater than 24 radiation lengths in the end-caps [25], so that entire showers, produced during collisions, can be encapsuled in the calorimeter. ECAL is segmented into three longitudinal layers: "front", "middle", and "back", of varying granularity. The front layer, situated closest to the beam pipe, has a granularity $\Delta\eta \times \Delta\phi = 0.050 \times 0.025$, matching this of the inner detector. The back layer has a granularity $\Delta\eta \times \Delta\phi = 0.050 \times 0.025$. All these calorimeter regions are calibrated individually.

The hadronic calorimeter (HCAL) is composed of iron with scintillating tile readout in the central region ($|\eta| < 1.7$) and liquid argon as active material and copper as energy absorber in the endcap ($1.7 < |\eta| < 3.2$) and forward ($3.2 < |\eta| < 4.8$) regions. Hadronic calorimeters provide a less granular readout than ECAL, with typically $\Delta\eta \times \Delta\phi = 0.1 \times 0.1$ in at least three longitudinal segments. The total thickness of the HCAL calorimeters is at least 10 absorption lengths over the whole acceptance region.

Jet reconstruction proceeds by combining information from calorimeter cells using the so-called jet finding algorithms. Two types of reconstruction sequences are applied to calorimeter cell readouts. In the first one, cells are combined in *calo towers*, which after noise suppression are given as input to jet finding algorithms. In the second one, noise reduction algorithms are applied directly to calorimeter cells, forming *calo clusters*, from which jets are reconstructed. It was found that jets formed from cluster signals represent the transverse energy flow of particles inside a jet better than the tower jets in the central and endcap regions, while in the forward region tower-based jets are performing better [25].

3.2.3 Muon Spectrometer

The ATLAS detector has been designed to efficiently detect muons with momenta ranging from 3 GeV up to one TeV. It is located outside of the calorimeter subsystem, because muons deposit there only a small fraction of their energy. The muon spectrometer provides the coverage in pseudorapidity range $|\eta| < 2.7$.

Toroid magnets produce an azimuthal magnetic field that bends the tracks of muons, thus allowing the measurement of their momenta. The integrated bending strength is roughly constant as a function of the azimuthal angle and pseudo-rapidity except for a significant drop in the range ($1.4 \leq |\eta| \leq 1.6$), corresponding to a transition between the coils of the barrel and barrel

and endcap toroid magnets.

Muon detectors consist of four kinds of stations positioned at increasing distance from the collision region. Their layout, depicted in Figure 3.7, was optimised such that muons originating from the interaction point traverse three stations of precision chambers. Monitored Drift Tubes (MDT) and Cathode Strip Chambers (CSC) are designed for measuring muon track coordinates, Resistive Plate Chambers (RPC) and Thin Gap Chambers (TGC) are used for triggering. The MDT measure pseudorapidity, which coincides with the direction of deflection in magnetic field. The measurement precision in each layer is typically better than 100 μm. The CSC additionally provide a rough (1 cm) measurement of the azimuthal angle ϕ in the ($|\eta| > 2.0$) region. The RPC and TGC provide similarly rough measurements of both directions near selected stations.

The muon spectrometer enables stand-alone measurements of muon momenta. A combination with measurements of the tracks in inner detector and calorimetric information is used to improve the efficiency and resolution.

3.2.4 Trigger system

The interaction rates at the LHC at the design luminosity are as large as about GHz. The trigger system reduces recorded event rates to about 400 Hz. The 25-ns time separation between proton bunches at the LHC arriving at the collision point forces trigger decisions to be equally fast. The average bunch crossing contains 20−80 interactions, depending on specific beam conditions. The aim of the trigger systems is to accept candidate processes predicted by the Standard Model and selected BSM theories, featuring energetic particles, while rejecting abundant soft QCD processes.

The ATLAS detector has a three-level trigger system, operating in a sequential order: the hardware-based Level-1 (L1) trigger, software-based Level-2 (L2) trigger and Event Filter, collectively referred to as the High Level Trigger or HLT. The L1 trigger uses the information from the muon trigger chambers (RPC and TGC) and reduced-granularity towers from calorimeters. Muon triggers select high transverse momentum muons, the calorimeter provide information on high transverse momentum electrons, photons, jets and hadronically decaying τ leptons or large missing transverse energy. The L1 trigger reduces the data rate to 75 kHz. Selected events are transferred to the L2 trigger and regions of interest (RoI) are defined around the triggering

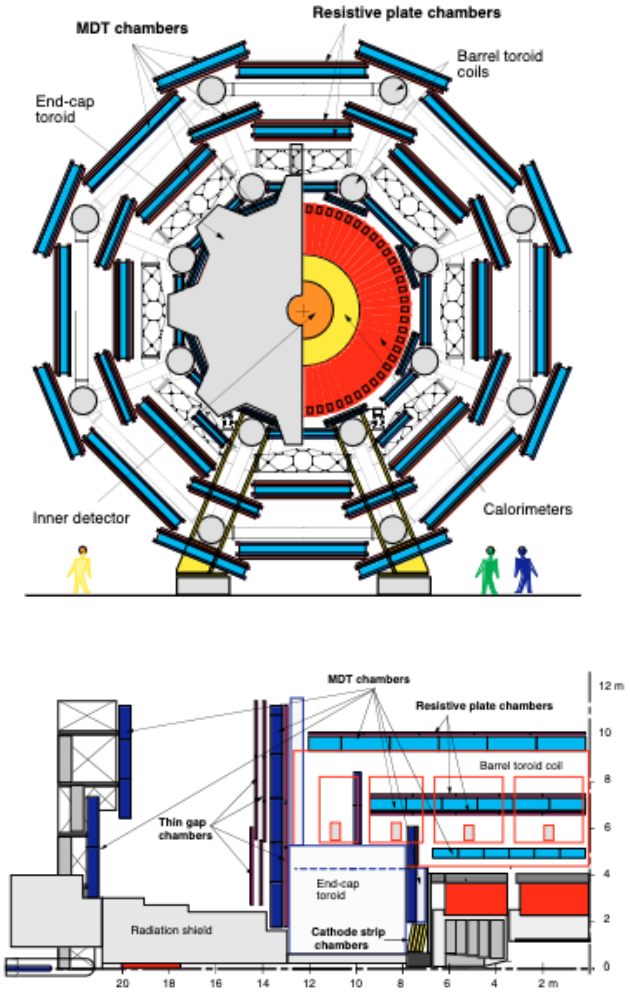

Figure 3.7: Transverse view (upper figure) of the barrel part of the muon spectrometer and side view of one of its quadrants (lower figure). Figures from Ref. [28]

objects. The size of the RoI window is determined by the L2 algorithms depending on the type of triggered object (for example, a smaller RoI is used for electron triggers than for jet triggers). Selection algorithms for the L2 trigger run on a PC farms and provide a refined analysis of the L1 features owing to fine-grained detector data and more optimal calibrations. Each event accepted by the L2 trigger is used to seed a sequence of EF algorithms. Unlike L2, which uses specialized algorithms optimized for timing performance, the EF typically employs more complex pattern recognition algorithms and calibration developed for offline analyses. This assures the additional rejection from ∼2 kHz to the output rate of ∼ 200 Hz.

A list of triggers available for each LHC run forms a **trigger menu**. It consists of triggers with different thresholds on transverse momenta of physics objects or their combinations (in case of multi-object triggers). A trigger whose all triggered events are saved is called unprescaled. Prescaled triggers, on the other hand, accept only a pre-defined fraction of events passing trigger selection. The exact trigger thresholds and prescales depend on the LHC luminosity. Performance of the ATLAS trigger system in 2015 can be found in Ref [29].

Candidate physics objets, such as electrons, muons, or jets are reconstructed based on trigger and subdetector responses. Exact identification requirements have varied with data taking periods and I will describe them in each analysis section.

3.2.5 Luminosity measurements

In order to correctly evaluate the probabilities of interesting processes and determine their cross-sections, a precise determination of instantaneous luminosity received at ATLAS is crucial. The luminosity is the number of particles in a surface unit. It is expressed in cm^{-2}, or units of inverse barns, $\mathrm{b}^{-1} = 10^{24}\mathrm{cm}^{-2}$. Instantenuous luminosity is typically expressed in $\mathrm{cm}^{-2}\mathrm{s}^{-1}$. Its measurement in collisions involves counting the number of collisions per bunch crossing. This number is determined independently by several luminosity-sensitive sub-detectors, which apply different algorithms [30, 31] using quantities proportional to instantenuous luminosity.

The instantaneous luminosity $\mathcal{L}_b$ produced by a single pair of colliding proton bunches is defined as

$$\mathcal{L}_b = \frac{\mu f_r}{\sigma_{inel}}, \tag{3.1}$$

where μ is the average number of inelastic interactions per bunch crossing (also called the pileup parameter), and f_r is the LHC bunch revolution frequency (11246 Hz for protons). It can be measured using

$$\mathcal{L}_b = \frac{\mu_{vis} f_r}{\sigma_{vis}}, \tag{3.2}$$

where σ_{vis} is the algorithm-specific visible cross-section representing the absolute luminosity calibration of the given algorithm, and can be determined via the vdM calibration method. The pileup parameter μ can be determined from $\mu = \mu_{vis}\sigma_{inel}/\sigma_{vis}$. To approximate σ_{inel}, a reference value of $\sigma_{inel} = 80$ mb is used by all LHC experiments for proton-proton collisions at $\sqrt{s} = 13$ TeV. The rate μ_{vis} is measured over a finite time interval called a luminosity block (LB, typically of a duration of one minute), during which data-taking conditions are assumed to remain stable.

The instantaneous luminosity for each LB was calculated from the sum of per-bunch luminosities:

$$\mathcal{L}_{inst} = \sum_{b=1}^{n_b} \mathcal{L}_b = n_b < \mathcal{L}_b >= \frac{< \mu > f_r}{\sigma_{inel}}, \tag{3.3}$$

where n_b is the number of colliding bunches (typically $\sim$ 2000 for Run 2), $< \mathcal{L}_b >$ is the mean per-bunch luminosity and $< \mu >$ is the pileup parameter averaged over all colliding bunch pairs. The per-bunch μ_{vis} is measured within a LB. The integrated luminosity is obtained by multiplying $\mathcal{L}_{inst}$ by the duration of the LB and summing over all LBs in the run.

During Run 2, the primary $\mathcal{L}_b$ measurement is provided by the LUCID-2 Cherenkov detector [32], localised 17 m away from the interaction point, thus in the far forward region of the ATLAS detector. LUCID-2 is equipped with two sets of photomultiplier tubes and detects Cherenkov light emitted by charged particles originating from collisions. This measurement is complemented by counts of the number of charged particle tracks provided by the Inner Detector. In addition, ATLAS calorimeters enable for bunch-integrated measurements (i.e. summed over all bunches), based on quantities proportional to instantaneous luminosity: liquid-argon (LAr) gap currents in the case of the endcap electromagnetic (EMEC) and forward (FCal) calorimeters, and photomultiplier currents from the scintillator-tile hadronic calorimeter (TileCal). The above methods provide *relative* measures of the luminosity. The measurements of the *absolute* luminosity are performed during special

low-luminosity LHC conditions using the van der Meer (vdM) method [33,34] and their results are extrapolated to the data-taking conditions. The total uncertainties on the integrated luminosities for each individual year of data-taking range from 2.0-2.4%. The full Run 2 proton-proton collision data sample corresponds to an integrated luminosity of 139 fb^{-1} , with an uncertainty of 1.7%.

3.3 The discovery of the Higgs boson

The Higgs boson was discovered by the ATLAS and CMS collaborations at the LHC in 2012 [16,17]. This observation crowns many years of experimental efforts to detect it. The Higgs boson was sought after using combined precision electroweak results [35] as well as through direct searches: at LEP [36], the Tevatron [37–39] and the LHC [40, 41] with the centre-of-mass energy of $\sqrt{s} = 7$ TeV. These last LHC searches were performed in the Higgs boson decay channels $h \to ZZ^* \to 4l$, $h \to \gamma\gamma$, $h \to WW^*(\to e\nu\mu\nu)$, $h \to b\bar{b}$ and $H \to \tau\bar{\tau}$ in 2011, yet did not provide statistically significant hints of the existence of a new particle. The discovery was finally accomplished by combining the 2011 datasets with 5.8fb^{-1} at $\sqrt{s} = 8$ TeV collected in 2012 using $h \to ZZ^* \to 4l$, $h \to \gamma\gamma$ and $h \to WW^*(\to e\nu\mu\nu)$ Higgs decays. These three channels have provided sufficient sensitivity to claim discovery, while the first two offered additionally high resolution in the invariant mass of the new particle.

The ATLAS discovery paper measured the Higgs mass to be 126.0 ± 0.4 (stat.) ± 0.4 (syst.) GeV, the combination of ATLAS and CMS results of ref [42] resulted in $m_h = 125.09 \pm 0.21$ (stat.) ± 0.11 (syst.) GeV, compatible with 124.97 ± 0.24 GeV measured at $\sqrt{s} = 13$ TeV by ATLAS in a study published in ref. [43]. Figure 3.8 lists measurements of the Higgs boson mass performed over the years including most recent results. The value has been fluctuating over the years, depending on the dataset and the final states used, and converging to $m_h = 125.11 \pm 0.09$ (stat) ± 0.06 (syst) GeV $= 125.11 \pm 0.11$ GeV with the combination of Run 1 and Run 2 data. In the measurements described througout this monograph a value of $m_h = 125.0$ GeV is used for simplicity.

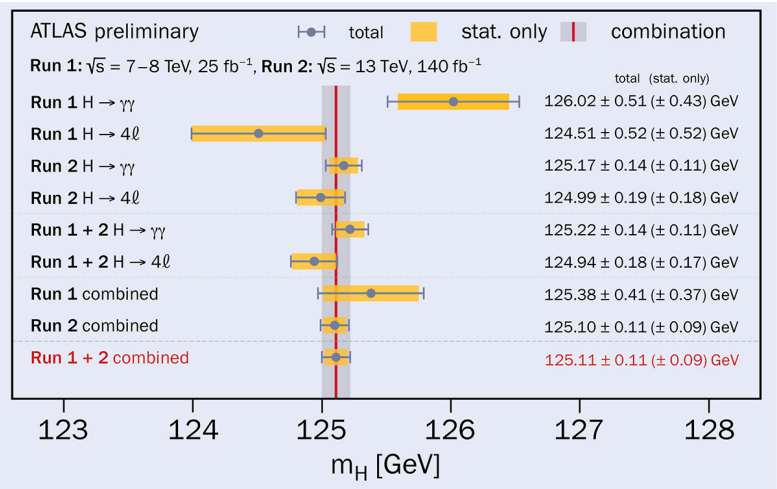

Figure 3.8: Higgs boson (here denoted as H) mass measurements with LHC Run 1 and Run 2 data using Higgs boson decays to two photons ($\gamma\gamma$) and four leptons ($ZZ^* \rightarrow 4l$) and their statistical combinations, performed by the ATLAS experiment. Figure taken from [44]

.

3.4 Properties measurements

Following the mass determination, ATLAS and CMS measured other fundamental properties of the new particle and compared them with SM prediction for a boson of a mass of m_h =125 GeV. Observations of its decays to pairs of bosons established that its spin cannot be fractional and therefore the new particle is indeed a boson. The measurements of both experiments provided strong hints for the spin and CP states to be $J^P = 0^+$ [45–47], proving a scalar nature of the new boson. Subsequent measurements of Higgs boson production strengths and couplings to fermions and bosons, summarised in Fig 3.9 have confirmed it has properties predicted by the BEH mechanism.

3.5 Outlook

The Higgs boson was discovered by the ATLAS and CMS at the LHC, crowning many years of its experimental searchers by various experiments. The mass of the new boson is measured to be $m_h = 125.11 \pm 0.11$ GeV. It is a

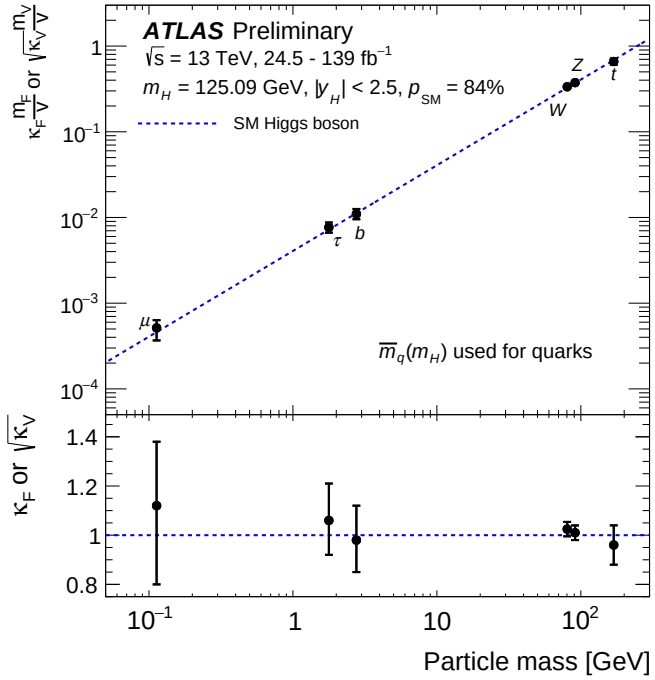

Figure 3.9: Reduced coupling strength modifiers $\kappa_F m_F/v$ for fermions (F denoting: top quark, bottom quark, τ lepton and muon) and $\sqrt{\kappa_V} m_V/v$ for weak gauge bosons ($V = W, Z$) as a function of their masses m_F and m_V, respectively, and the vacuum expectation value of the Higgs field v=246 GeV. The SM prediction for both cases is shown with a dotted. Figure taken from [48]

.

CP-even scalar boson. So far, all measured properties of the new boson are (within uncertainties) consistent with the SM Higgs boson.

With more data, further measurements are being undertaken in order to search for more subtle effects, that could reveal its BSM nature. For example, the Higgs boson can be a part of a larger sector of bosons that either take part in electroweak symmetry breaking or not. These hypothetical additional Higgs bosons which can be neutral (CP even, CP odd, or featuring the superposition of CP eigenstates) and charged may have masses similar to the discovered one. Details depend on a particular model, amongs which the electroweak singlet model [49], supersymmetric theories, such as the (h)MSSM [50–52], the two Higgs doublet model (THDM) [53] and the Higgs portal model [54] are currently being investigated experimentally. These theories are particularly attractive extensions of the SM because they predict the existence of particles that could provide explanation for Dark Matter in the Universe or provide additional sources of CP violation to solve the matter-anti-matter asymmetry puzzle, not accounted for in the SM itself.

An important question that needs to be answered regarding the Higgs boson (sector), is whether the electroweak symmetry breaking mechanism follows exactly the one presented by Brout, Englert and Higgs, with a single scalar particle with a customised potential. Precise measurements of parameters of this potential can be done by measuring both Higgs couplings (that are related to the potential vacuum) to other SM particles and its self-interactions (that determine the global shape of the Higgs potential). Deviations from the scaling of couplings with particles masses would hint for example at Higgs compositeness models [55, 56], that offer an alternative explanation of electroweak symmetry breaking. The exact form of the Higgs field potential, on the other hand, can have significant cosmological implications, related to predictions of Higgs vacuum stability or models in which the Higgs boson acts as the inflation field [57–60].

Selected measurements related to the Higgs potential through its interactions with electroweak bosons and self-interactions will be reviewed in this monograph. These studies aim at more precise determination of the Higgs boson potential and investigate possible beyond Standard Model features of the Higgs boson.

4 Measurements using $h \to WW^*(\to e\nu\mu\nu)$ decays

This chapter presents measurements performed using Higgs boson decays to a pair of W bosons. Only W bosons that decay to light leptons of different flavours and neutrinos are selected, hence the investigated Higgs signal is $h \to WW^*(\to e\nu\mu\nu)$. These measurements are based on collision events, amounting to 39 fb^{-1} of integrated luminosity, that were recorded by the ATLAS detector at a centre-of-mass energy$\sqrt{s} = 13$ TeV. Measurements of the Higgs boson production cross-section times branching ratio in leading production channels are discussed. Cross-section measurements in gluon fusion (ggF) with up to two jets are presented in Section 4.8, while the main focus of this Chapter is on studies in vector boson fusion (VBF) Higgs production. In Section 4.9.6 the VBF cross-section measurement is detailed. It is performed assuming no beyond Standard Model (BSM) physics. Next, in Section 4.10 a search of BSM effects in Higgs couplings to massive electroweak bosons is presented. It is performed studying effects of W and Z bosons polarisations on coupling strengths to the Higgs boson. Both analyses share a dataset and event selection; improvements specific to the polarisation-dependent measurement will be addressed in Section 4.10.

This chapter is based on two publications: [7] and [61] that I co-authored.

4.1 Introduction

Example Feynman diagrams contributing to Higgs boson production via gluon fusion (ggF) and vector boson fusion (VBF) are depicted in Figure 4.1. The Higgs decays to a pair of oppositely charged W bosons, $H \to W^+W^-$. This decay is typically denoted with $H \to WW^*$, where charges are skipped,

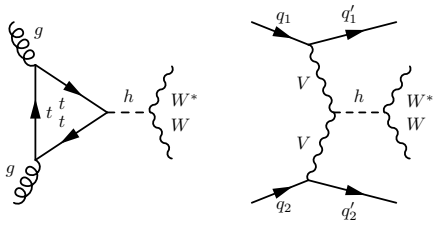

Figure 4.1: Example Feynman diagrams contributing to ggF (left) and VBF (right) Higgs boson production. V denotes either a W or a Z boson.

and the off-shellness of one W is highlighted by an asterisk. Indeed, a particle of a mass of 125 GeV at rest does not have phase space sufficient for creating two bosons of mass $\sim$ 80 GeV. The Higgs branching fraction to W^+W^-, amounting to $\sim 20\%$, is the second largest branching fraction of the Higgs particle. Therefore it is an interesting channel to use for measuring Higgs boson properties, offering large abundance of events. In the following I focus on the decays of the W bosons to light leptons, electrons or muons and neutrinos, which are experimentally easier to reconstruct than their decays to τ leptons and hadrons. The leptonic final state, despite amounting to only $\sim$20% of all W boson decays, offers an interesting insight into the Higgs boson spin and parity properties. [1]

In the Higgs boson centre of mass frame, the W bosons are emitted back-to back, as shown in Fig 4.2. Each W boson has spin 1, which is conserved in its decays to fermions of spin $\frac{1}{2}$: charged light leptons and neutrinos. Neutrinos (anti-neutrinos) are massless, and therefore their helicities (marked with thick arrows next to their momenta) are left (right) handed. Due to the spin-0 nature of the Higgs, the polarisations of the W bosons are correlated: they are either both transverse- or both longitudinal in the Higgs boson centre-of-mass frame. Consequently, charged leptons originating from the W bosons are aligned. If the Higgs boson is not produced at rest, its boost in the detector reference frame causes momenta of W bosons to form an angle

[1] These spin properties can also be elegantly accessed using ten times less abundant Higgs decays to two Z bosons and correlations between decay planes span by charged light leptons originating from Z bosons. Additional advantage of the $H \to ZZ^*$ channel comes from the ability to reconstruct the Higgs boson centre-of-mass frame.

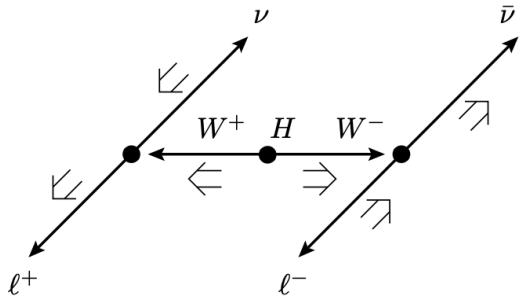

Figure 4.2: Kinematics of $H \to WW(\to e\nu\mu\nu)$ decays in the Higgs boson rest frame.

and the charged leptons momenta to form a small opening angle (ϕ_{ll}).

Due to the presence of two neutrinos in the final state, and unknown energy fractions of colliding quarks or gluons, reconstruction of the energy of two decaying W bosons cannot be done without additional assumptions and approximations. Instead, the transverse mass m_T can be measured by taking into account energy and momentum deposits of the charged leptons as well as observed momentum imbalance in the plane transverse to the colliding bunches. I will discuss other kinematical properties of the $H \to WW^*(\to e\nu\mu\nu)$ experimental signature after more details on data selection and particle reconstruction are given.

4.2 Monte Carlo and data samples

The candidate events in data were selected from the $\sqrt{s} = 13$ TeV proton-proton collision dataset collected by ATLAS in 2015 and 2016 and corresponding to total integrated luminosity of 36.1 ± 0.8 fb^{-1} [30]. All ATLAS sub-detectors have been fully operational [62].

Details on the Monte Carlo generators used to simulate samples of all relevant processes are given in Table 4.1. MC modeling was used to study properties of the SM and BSM signals and to optimise signal selection criteria.

The modeling of Higgs production through ggF process was realised with Powheg NNLOPS interfaced with Pythia 8 [63] with AZNLO tune for underlying event, showering and hadronization [64]. Its prediction includes

Table 4.1: Overview of the simulation tools used to generate signal and background processes. Information given in consecutive columns refers to: matrix elements, modeling the underlying event and parton showers, PDF as well as the prediction order (in QCD and if relevant in EW) of the total cross-section. Alternative event generators and configurations used to estimate systematic uncertainties are shown in parentheses. Samples specific to the generation of BSM signals in the polarisation dependent Higgs couplings study, are marked with (*).

Process	Matrix element (alternative model)	UEPS	PDF set	Prediction order for total cross-section
ggF	Powheg NNLOPS	Pythia 8	PDF4LHC15 NLO	NNLO QCD + NLO EW
VBF	Powheg-Box v2	Pythia 8.212	PDF4LHC15 NLO	NNLO QCD + NLO EW
	(MG5_aMC@NLO v2.3.3 + Pythia 8.212)			
	(Powheg-Box v2 + Herwig 7.0.1)			
VBF (*)	MG5_aMC@NLO v2.4.2	Pythia 8.212	NNPDF3.0 NLO	NNLO QCD + NLO EW
VH	Powheg-Box v2	Pythia 8.186	PDF4LHC15 NLO	NNLO QCD + NLO EW
ggF $H \to \tau\tau$	Powheg-Box v2	Pythia 8.186	PDF4LHC15 NLO	NNLO QCD
VBF $H \to \tau\tau$	Powheg-Box v2	Pythia 8.186	PDF4LHC15 NLO	NNLO QCD
$t\bar{t}$	Powheg-Box v2	Pythia 8.210	NNPDF3.0 NLO	NNLO+NNLL QCD
	(Sherpa v2.2.1)			
	(Powheg-Box v2 + Herwig 7.0.1)			
Wt	Powheg-Box v2	Pythia 6.428	CT10	NLO QCD
	(MG5_aMC@NLO v2.2.2 + Herwig++)			
	(Powheg-Box v2 + Herwig++)			
$WZ/\gamma^\star$, $ZZ/\gamma^\star$	Sherpa v2.2.2		NNPDF3.0 NNLO	NLO QCD
	(MG5_aMC@NLO v2.3.3 + Pythia 8.212)			
$W\gamma, Z\gamma$	Sherpa v2.2.2		NNPDF3.0 NNLO	NLO QCD
	(MG5_aMC@NLO v2.3.3 + Pythia 8.212)			
$qq, qg \to WW$	Sherpa v2.2.2		NNPDF3.0 NNLO	NLO QCD
	(MG5_aMC@NLO 2.3.3 + Pythia 8.212)			
$gg \to WW$	Sherpa v2.1.1		CT10	NLO QCD
$Z/\gamma^\star$	Sherpa v2.2.1		NNPDF3.0 NNLO	NNLO QCD
	(MG5_aMC@NLO v2.2.2 + Pythia 8.186)			

QCD corrections at perturbative orders: NNLO for 0-jet events, NLO for 1-jet events and LO for 2-jet events. The overall normalization of the Powheg NNLOPS/Pythia 8 produced samples are taken from a calculation at N3LO. The ggF+2j signal events were generated with the MadGraph5_aMC@NLO 2.4.2 generator [65, 66], which provides a calculation of the matrix element at next-to-leading-order (NLO) precision for ggF events with up to two additional partons in the final state. The calculations of the matrix element are based on the predictions of the Higgs Characterisation model [67],

while the parton shower, hadronisation and underlying-event activity were simulated with the Pythia 8.212 generator using the A14 set of tuned parameters [68]. Parton distribution function (PDF) sets NNPDF3.0 [69] are used in the cross-section calculation. In total, three different Monte Carlo samples were produced, corresponding to a CP-even, a CP-odd or a CP-mixed coupling between Higgs bosons and gluons, using the FeynRules model HC_NLO_X0_UFO-heft [70]. The Higgs boson decay $H \to WW^*(\to e\nu\mu\nu)$ was modelled according to the SM.

VBF process was modelled with POWHEG, interfaced with PYTHIA 8, normalised to the NLO (in both QCD and QED) cross section with an approximate NNLO QCD correction applied [71]. The PDF4LHC15 PDF set [72] was used. For the measurement of the Higgs boson couplings to longitudinally and transversely polarised W and Z bosons, the VBF production of the Higgs boson and its subsequent decays into W bosons were simulated at leading order (LO) in QCD using MadGraph5_aMC@NLO 2.4.2. This generator was chosen because it allows to modify Higgs coupling strengths to longitudinally and transversely polarised bosons, both in the Higgs boson production and in its decay. In these (BSM) samples, parton shower effects were simulated with the PYTHIA 8.212 generator using the A14 set of tuned parameters [68]. The renormalisation and factorisation scales were both set to the sum of the transverse momenta of the jets, and the shower scale was set to 0.25 times the maximum p_T of the radiated partons. In this way kinematical properties of the simulated event samples were similar to NLO samples generated with MadGraph5_aMC@NLO 2.4.2, thus decreasing theoretical uncertainty on signal modeling. More details on technical aspects of generating these samples will be given in Section 4.10.1.

The Higgs associated production events with W and Z bosons, WH and ZH, were fully generated with POWHEG-Box v2 MinLO [73] interfaced to PYTHIA 8.186, with the AZNLO set of tuned parameters.

The $\tau\tau$ decays of the Higgs boson, with τ leptons decaying to electrons or muons and their associated neutrinos have experimental signature identical to the signal processes because two additional neutrinos escape detection. These processes feature no HWW couplings and are considered as backgrounds. Both ggF and VBF Higgs productions were simulated using POWHEG-Box interfaced to PYTHIA 8 parton shower. Their cross-section was fixed to the SM predictions at NLO. The processes of Higgs associated production with $t\bar{t}$ and $b\bar{b}$ pairs were neglected due to their insignificant contributions to the phase-space regions probed by the studies presented in this chapter.

The top-quark pair ($t\bar{t}$) production process was modelled using POWHEG-Box. The matrix elements were calculated at NLO precision in QCD using the NNPDF3.0 NLO PDF set with a top-quark mass of 172.5GeV, while the hdamp parameter [40] is set to 1.5 times the top-quark mass. Matrix element calculation was interfaced to PYTHIA 8 with the parton shower tune A14. The $t\bar{t}$ production cross section was normalised to the next-to-next-to leading order (NNLO) predictions in perturbative QCD, The associated production of a single top-quark and a W boson (Wt) was generated with POWHEG-Box interfaced to PYTHIA 6.428 for parton shower, using the Perugia2012 tune [74] and the CT10 PDF set [75]. The diagram removal scheme [76] is used to remove overlaps with the top-quark pair production process that occur at NLO in QCD.

The production of diboson processes with $q\bar{q}$ and qg initial states leading to dilepton final states: $l\nu l\nu$, $l\nu ll$ and $llll$ were modeled with Sherpa v2.2.2 for both the matrix element as well as the underlying event and parton showers. The matrix element calculations include all off-shell components with up to one jet at NLO in QCD, while diagrams with up to 3 jets are described at LO accuracy. The different jet-multiplicity final states are merged using the MEPS@NLO formalism at a merging scale of Qcut = 20GeV. The samples are normalized using an NLO calculation of the inclusive cross section.

All simulated events were generated at a centre-of-mass energy of $\sqrt{s} = 13$ TeV. They passed the ATLAS detector simulation [77, 78] and were overlaid with additional inelastic pp interactions that were generated with PYTHIA 8.153 in order to match the pile-up conditions observed in the ATLAS data.

4.3 Object definitions and event preselection

In the described analyses the reconstruction of all physics objects: electrons, muons, jets and the missing transverse momentum, are calculated with respect to primary vertices (PV). In the LHC runs in 2015 (2016) an average of 13.4 (25.1) interactions between protons were observed in each crossing of colliding proton bunches.

PV candidates are reconstructed by applying an iterative vertex finding algorithm [79] to tracks with $p_T > 400$MeV and originating from the interaction region [80]. The primary vertex candidates are required to consist of at least two reconstructed tracks. From all PV candidates, the one with the highest p_T^2 sum of the associated tracks is chosen to be the primary vertex of

the event.

Electron candidates are selected from a reconstructed track in the ID that is matched with topological clusters of energy deposits in the electromagnetic (EM) calorimeter. Electrons can be resonstructed in the rapidity range $\eta \in (-2.47, 2.47)$, with the region between the $1.37 < |\eta| < 1.52$) excluded due to a gap between the barrel and endcaps in the liquid argon (LAr) calorimeter. In addition, the transverse energy E_{T} of electron candidates has to exceed a value of 15GeV. Electrons with $E_{\mathrm{T}} < 25$GeV have to pass the *TightLH* likelihood-based identification criteria, while electrons with $E_T > 25$GeV must pass the *MediumLH* identification definition, whose technical details are given in [81]. The absolute value of the longitudinal impact parameter of each electron track, calculated with respect to the primary vertex, is required to fulfil $|z_0 \sin\theta| < 0.5$mm, whereas the transverse impact parameter significance ($|d_0|/\sigma_{d_0}$), calculated with respect to the beam line, is required to be lower than 5. Furthermore, objects that have been reconstructed as both electron candidates and as converted photons are rejected. Electron candidates are additionally required to be sufficiently isolated from hadronic activity to reduce the background from hadrons faking electron signatures or heavy-flavour decays inside jets. The isolation conditions are imposed based on electron candidate transverse energy E_T, measured in the calorimeter, and the magnitude of its transverse momentum, p_T, determined in the Inner Detector. For electron candidates with $E_{\mathrm{T}} < 25$GeV, the energy sum within a radius of $\Delta R = 0.2$ in the calorimeter system around the electron cluster has to be smaller than 0.11 times the transverse energy of the electron. Angular separation ΔR between objects is computed taking into account differences in their azimuthal angles ($\Delta\phi$) and pseudorapidities ($\Delta\eta$): $\Delta R = \sqrt{\Delta\phi^2 + \Delta\eta^2}$. In addition, the transverse momentum sum around the electron track in a radius $\Delta R = 0.4$ in the Inner Detector is required to be smaller than 0.06 times the electron E_{T}. For candidates with $E_{\mathrm{T}} > 25$GeV, the E_T and η dependent *Gradient* isolation criterion is applied. A summary of electron selection requirements is given in Table 4.2.

Muon candidates are reconstructed from combined tracks using information from both the Muon Spectrometer and the Inner Detector (ID). This combination is based on an overall fit using the hits of the track in the ID, the energy loss in the calorimeter, as well as the hits of the track in the muon system. The pseudorapidity is required to be lower than 2.5, while the transverse momentum must exceed 15GeV. Based on the quality of the reconstructed objects, muon candidates are defined as either *Loose*, *Medium* or *Tight* [82],

with increasing purity of prompt muons. In both analyses, muon candidates are required to comply with *Tight* quality criteria. The requirements on the longitudinal and transverse impact parameters are $|z_0 \sin\theta| < 0.5$mm and $|d_0|/\sigma_{d_0} < 3$, respectively. As for electron candidates, muons are required to be sufficiently isolated from hadronic activity: The energy sum within a radius ΔR equal to 0.3 in the calorimeter system around the combined track has to be smaller than 0.09 times the transverse muon momentum. In addition, the transverse momentum sum around the muon track in a radius $R = 0.2$ in the Inner Detector is required to be smaller than 0.06 times the muon p_T. A summary of the various muon selection requirements are given in Table 4.2.

Jets are reconstructed from topological clusters of energy deposits in the calorimeter system using the anti-k_T algorithm [83] with a distance parameter of $R = 0.4$. The topological clusters are calibrated to the electromagnetic scale using p_{T} and η dependent correction factors, which account for losses in passive material, the non-compensating response of the calorimeters, and contributions from pile-up interactions [84]. The absolute value of the pseudorapidity is required to be lower than 4.5 and the transverse momentum has to be at least 30GeV.

An object based definition of the **missing transverse momentum,** $\vec{E}_{\mathrm{T}}^{\mathrm{miss}}$, with magnitude $E_{\mathrm{T}}^{\mathrm{miss}}$ (a.k.a. missing transverse energy), is used in this analysis. It is defined as the negative vector sum of two components: calibrated calorimeter cells belonging to identified high-p_T objects (such as electrons, photons, jets and muons) and the track-based soft term. The latter includes reconstructed tracks not associated with these objects, that originate from the same primary vertex [85]. A similar variable, also named missing transverse momentum but denoted $\vec{p}_T^{miss}$, uses the tracks associated with the jets instead of the calorimeter-measured jets. Here, the total E_T^{miss} term takes all central (forward) region jets into account if their p_T is above 20GeV (30GeV) and if they pass the corresponding JVT (fJVT) requirement.

To reduce the number of jets originating from pile-up vertices, jets with $p_{\mathrm{T}} < 60$GeV and $|\eta| < 2.4$ are required to have the jet vertex tagger (JVT) response be larger than 0.59 [86]. Furthermore, to reduce pile-up contributions in the forward regions, the forward jet vertex tagger (fJVT) is applied [87] on jets with $2.5 < |\eta| < 4.5$ with an operating point that has an overall efficiency of 90% for jets coming from the hard process.

Jets containing b-hadrons are identified using the MV2c10 b-tagging algorithm [88, 89] with an operating point that has an overall efficiency of

85%, evaluated in simulated $t\bar{t}$ events. The corresponding overall rejection rate for selecting jets originating from light-flavour hadrons or gluons is approximately 34, while the overall rejection rate for selecting jets containing c-hadrons is 3. In this note, jets recognised as b-quark-induced will be referred to as b-jets. For the purpose of finding b-jets, also sub-threshold jets are considered as long as their p_T is larger than 20GeV.

In order to avoid a multiple counting of physics objects, an overlap removal procedure is applied. It is based on the angular separation ΔR between two reconstructed objects. Jets are removed from the analyses if their separation ΔR to a charged lepton is smaller than 0.2. However, in case the charged lepton is a muon, the jet is only removed if it has less than three associated tracks with $p_T > 500$MeV or both of the following conditions are met: The p_T ratio of the muon and jet is larger than 0.5 ($p_{\mathrm{T}}^{\mu}/p_{\mathrm{T}}^{jet} > 0.5$) and the ratio of the muon p_T to the sum of p_T of tracks with $p_T > 500$MeV associated to the jet is larger than 0.7. Electron and muon candidates, with transverse momentum p_T, are removed from the two analyses if they are within $0.2 < \Delta R < \min(0.4, 0.04 + 10\mathrm{GeV}/p_T)$ of any jet passing the previously stated overlap removal procedures. In addition, electron candidates are removed if they share an ID track with a muon candidate. However, if a calorimeter-tagged muon shares an ID track with an electron, the muon is removed instead.

Table 4.2: Object definition requirements for electron and muon candidates.

Electrons		Muons	
$15\mathrm{GeV} < p_T < 25\mathrm{GeV}$	$p_T > 25\mathrm{GeV}$	$15\mathrm{GeV} < p_T < 25\mathrm{GeV}$	$p_T > 25\mathrm{GeV}$
$z_0 \sin\theta < 0.5\mathrm{mm}$		$z_0 \sin\theta < 0.5\mathrm{mm}$	
$d_0/\sigma(d_0) < 5$		$d_0/\sigma(d_0) < 3$	
$\lvert\eta\rvert < 2.47$ excluding $1.37 < \lvert\eta\rvert < 1.52$		$\lvert\eta\rvert < 2.5$	
TightLH	*MediumLH*	*Tight*	
$E_{\mathrm{T}}^{\Delta R=0.2} < 0.11 \cdot E_{\mathrm{T}}$	Gradient isolation	$E_{\mathrm{T}}^{\Delta R=0.3} < 0.09 \cdot p_T$	
$p_{\mathrm{T}}^{\Delta R=0.4} < 0.06 \cdot E_{\mathrm{T}}$		$p_{\mathrm{T}}^{\Delta R=0.2} < 0.06 \cdot p_T$	

4.4 Trigger selection

The distribution of transverse momenta (p_T) of leptons coming from the ggF Higgs boson production peaks at small values. For this reason, the minimum allowed transverse momentum of the leading lepton was lowered with respect to Run 1 from 25 GeV to 22 GeV. This cut has been optimised in order to balance the signal acceptance efficiency on one hand, with rejection of the so called "fake lepton" backgrounds (see Section 4.6) on the other. In the fiducial region considered, "fake lepton" backgrounds stem from processes featuring a W boson accompanied by jets, that are misidentified as leptons. The estimation of the rates of these backgrounds, detailed in Section 4.6, is difficult and associated with large uncertainties. Due to negative impact of large rates of fake lepton backgrounds on the sensitivity to the Higgs boson signal, they are important processes to study while deciding on a trigger selection. In the analyses described in this chapter trigger selection was optimised using the logical OR between single- and di-lepton triggers.

A combination of single and double leptons triggers was used. Single lepton triggers with transverse momentum (p_T) thresholds for electrons ranging between 24 GeV and 26 GeV and for muons between 20 GeV and 26 GeV were used. Di-lepton triggers accepted events with minimum thresholds at 17 and 14 GeV for electrons and muons, respectively. Exact threshold as well as isolation requirements depended on data taking periods [29]. Single-lepton triggers with higher-p_T thresholds are more efficient at high lepton p_T than the lower-p_T triggers using isolation requirements. Two di-lepton triggers were available for the considered data selection: `e17_lhloose_mu14` and `e7_lhmedium_mu24`. They differ by the isolation criteria for the muon and p_T thresholds for both leptons. Their effect of the logical OR between di- and single lepton triggers was evaluated for two p_T thresholds: 22 and 25 GeV. For all channels considered, efficiency gain with respect to single lepton triggers only was evaluated in two scenarios: 1) by including both di-lepton triggers and 2) using `e17_lhloose_mu14` only. The gain was computed in percentage with respect to the usage of single lepton triggers. This optimisation was evaluated after the pre-selection in each signal category. In the "0 jets", "1 jet" categories the efficiency gain was evaluated on a ggF event sample, while in the "2 or more jets" category the evaluation was performed on both VBF and ggF samples. The efficiency gain decreases with the number of jets requested in each signal category, reaching 18.8% (17.0%) and 13.5%

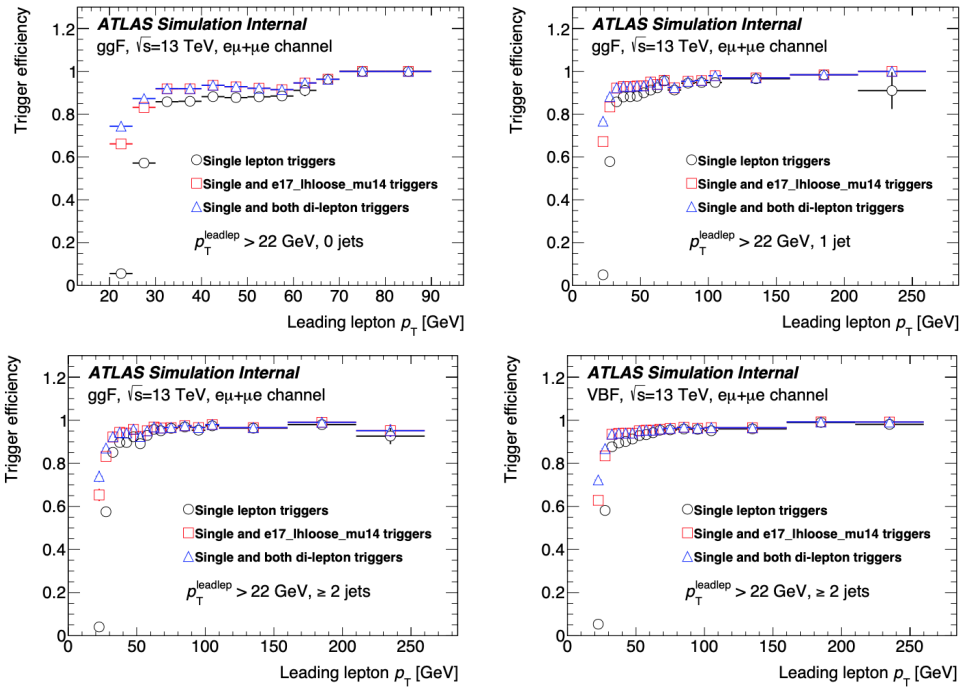

Figure 4.3: Efficiency plots for the single- and di-lepton triggers after pre-selection and cut on the leading lepton $p_T > 22$ GeV for both $e\mu$ and μe channels. The plots were made for: ggF requiring 0 jets (upper left), 1 jet (upper right), 2 jets (bottom left) and for VBF (bottom right).

(12.1%) in "0 jets", and "1 jet" categories, respectively for scenario 1) (2)). In the "2 or more jets" category, the efficiency gain for ggF is 8.8% (8.0%), while for VBF processes reaches 6.6% (6.0%). The channel, in which the electron is a leading p_T lepton, $e\mu$, is more affected by adding the `e17_lhloose_mu14` trigger, while its effect on the μe channel is about twice as low. The outcome of adding also the `e7_lhmedium_mu24` trigger is on average relatively small: it only affects the μe channel by a few percents. Therefore, only the `e17_lhloose_mu14` di-lepton trigger is used in the analyses.

The combined efficiency of the single-lepton and dilepton triggers is 95% in the fiducial regions used in these analyses, see Figure 4.3.

4.5 Event pre-selection

Candidate events consistent with the final state $H \to WW^* \to e\nu\mu\nu$ accompanied by either zero, one, or two jets are selected by requiring that an appropriate single-lepton or dilepton triggers have fired, as described in Section 4.4. Additionally, candidate events must fulfill more detailed requirements:

1. There are exactly two charged light leptons with opposite electrical charge and different flavour.
2. Two largest transverse momenta of leptons are above thresholds: $p_T^{leading} > 22\text{GeV}$, $p_T^{subleading} > 15\text{GeV}$.
3. The invariant mass of two charged leptons is above a threshold value: $m_{ll} > 10\text{GeV}$.

The requirement on the final state choice (1.) suppresses abundant Z boson backgrounds, that similarly to the signal feature two charged leptons, but of the same flavour. The requirement (2.) is dictated by experimental triggers and was optimised for best efficiency in rejecting W+jets and QCD backgrounds. The third requirement suppresses backgrounds from low-mass resonances such as Υ and J/ψ and non-resonant di-boson processes. After these cuts, events are split into jet multiplicities, see Figure 4.4. The dominant backgrounds in the "0 jets" channel are WW and Z/γ^* with a smaller contribution of top quark production and fake backgrounds. With the increasing number of jets the contribution of single- and double top quark processes increases significantly, while the contributions from di-boson and fake lepton backgrounds decrease.

Additional requirements are formulated using more complex kinematical variables, exploiting correlations among reconstructed particles. The vector sum of all transverse momenta of leptons, jets, and reconstructed tracks (not associated with these objects) in a signal-like event is typically non-zero, due to the presence of two undetected neutrinos from decays of W bosons. The negative of this vector is called missing transverse momentum, $\vec{E}_T^{miss}$, and its magnitude, denoted E_T^{miss} is transverse energy. Based on missing transverse momentum, the transverse mass, m_T, is computed: $m_{\mathrm{T}} = \sqrt{(E_{\ell\ell} + E_{\mathrm{T}}^{\mathrm{miss}})^2 - |\vec{p}_{\mathrm{T},\ell\ell} + \vec{E}_{\mathrm{T}}^{\mathrm{miss}}|^2}$ with $E_{\ell\ell} = \sqrt{|\vec{p}_{\mathrm{T},\ell\ell}|^2 + m_{\ell\ell}^2}$ and $\vec{p}_{\mathrm{T},\ell\ell}$ being the combined dilepton momentum vector in the transverse plane.

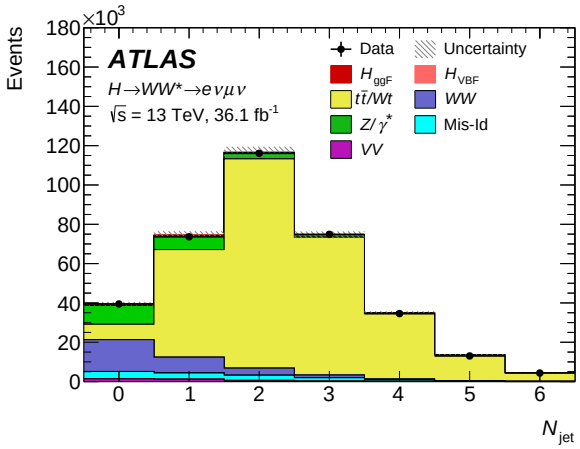

Figure 4.4: Jet multiplicity distribution after applying the preselection criteria for simulated background and signal processes (colour histograms) and data (black). The shaded band represents the experimental systematic uncertainty.

Transverse mass is related to the invariant mass of the WW^* system, since the longitudinal momenta of the two neutrinos cannot be measured. This variable is useful in distinguishing Higgs boson production in gluon fusion from other SM processes.

Selection requirements based upon these variables are specific to each signal category and were optimised individually. Details about defining signal and control regions will be described in dedicated sections. The term "preselection" will be used from now on refering to requirements $(1-3)$.

4.6 Estimation of fake lepton backgrounds

The W+jets background, despite featuring a final state that does not match preselection requirements, enters the analysis due to a misidentification of a jet as a lepton or due to the reconstruction of soft leptons originating from heavy-flavour decays inside a jet. The misidentification probability is typically relatively low and expected to be not sufficiently well described in Monte Carlo simulations. The large number of events consisting of W boson and jets, however, makes this proces a non-negligible background in the analysis.

The estimation of fake lepton backgrounds is performed using the so called fake factors method. For this purpose, a control sample is defined using events with one identified lepton and one lepton failing the nominal object definition requirements but passing looser requirements (referred to as "anti-identified"). The contribution of the misidentified-lepton background to the signal region is estimated by scaling the control sample via transverse momentum and pseudorapidity-dependent extrapolation factors, which are defined as the ratio of the identified leptons to anti-identified leptons and are determined using data samples consisting of Z + jets and multijet events.

The fake lepton background consists of events in which either one or two leptons are misidentified, "single" and "double" fakes, respectively. Their yields are estimated using a data sample defined by either one lepton (id) passing the standard selection criteria and the other lepton (anti-id) passing a loosened lepton selection or both leptons passing only a loosened selection. Anti-id leptons are not isolated and do not overlap with id leptons. Anti-id electrons are required to pass the LHLoose identification and anti-id muons are required to pass the Medium identification. Additionally, for anti-id muons the impact parameter definition is changed to $d_0/\sigma(d_0) < 15$.

This is extrapolated to the signal region using "fake factors" defined as:

$$FF = \frac{N_{\text{id}}}{N_{\text{anti-id}}}, \tag{4.1}$$

where N_{id} and $N_{\text{anti-id}}$ are number of objects passing the lepton identification selection and passing the "anti-id" requirements but failing the "id" criteria, respectively. Fake Factors are defined separately for muons and electrons. Loosened requirements result in jet-enriched samples, either di-jet or Z+jets. The Z+jets fake factors are used for the bulk of the W+jets estimation, while the di-jet fake factors are used for the W+jets events in which the fake lepton is the only object firing the trigger (QCD background).

The number of events in the signal sample, N_{id+id}, can be obtained using:

$$N_{id+id} = N_{id+id}^{EW} + N_{id+id}^{W+jets} + N_{id+id}^{QCD}$$

where N_{id+id}^{EW} denotes all events with two real leptons (including the signal ones) , single fake backgrounds are included in N_{id+id}^{W+jets} and double fake backgrounds in N_{id+id}^{QCD}. To estimate the fake backgrounds, a W+jets control sample is defined with one "id" lepton and the other lepton being anti-identified;

$$N_{id+anti-id} = N_{id+anti-id}^{W+jets} + N_{id+anti-id}^{EWMC} + N_{id+anti-id}^{QCD}. \tag{4.2}$$

The contamination of the other background processes with two real leptons, $N^{EWMC}_{id+anti-id}$ is subtracted using Monte Carlo before the fake factor calculation.

Muon and electron fake factors are measured from jets in events with a Z boson candidate, which is obtained by selecting events with exactly three loosely identified lepton candidates. Two of these leptons should be of same flavour and opposite sign with their invariant mass m_{ll} compatible with the Z boson mass: $70\text{GeV} < m_{ll} < 110\text{GeV}$. They are both required to fulfil the "id" criteria and at least one of them must be matched to one of the single lepton triggers used in the analysis. The additional third lepton is the fake candidate. To reduce the $Z + \gamma$ background in events with the third lepton being an electron, the selection for the opposite sign lepton pair is tightened to $80\text{GeV} < m_{ll} < 110\text{GeV}$. In events with two Z boson candidates, the one with invariant mass closer to the Z mass pole is chosen.

The FF is calculated as a function of the p_T and η of the anti-id lepton and is depicted in Figure 4.5. The fake factors obtained in data are also compared with the MC predictions from: POWHEG, ALPGEN [90] and SHERPA [91]. Three sources of systematic uncertainty are taken into account in the calculation of the FF in the fiducial regions of all signal categories. They are computed for electrons and muons, for different p_T ranges. The first source is the statistical uncertainty of the FF in each bin taken into account as a systematic uncertainty. The observed non-monotonic behaviour of statistical uncertainty for different p_T bins in electron FFs is a combination of two effects: differences in the bin sizes and anti-id cuts changing at $p_T = 25$ GeV. The second source of uncertainty is due to the EW background subtraction. To estimate this, the FF is recalculated with the backgrounds varied up and down by 10%. The last systematic uncertainty arises from the difference in flavour composition between the Z+jets and W+jets samples resulting in differences in jet kinematics and hence FF estimation. The correction factor is therefore applied to the Z+jets sample and the associated uncertainty is evaluated by comparing the FF in both Z+jets and W+jets MC. The systematical uncertainties are of the order of 40% for electrons and range from 30% to 150% for muons depending on their p_T. For electrons, the uncertainty is not completely dominated by one source, but at the low p_T the sample composition uncertainty is the largest, at high p_T the statistical and EW subtraction is more important. For muons, the EW subtraction uncertainty is very large at high-p_T due to the normalisation uncertainty of a large WZ tail.

By design of the fake factor method, the QCD contribution is double

counted in the VBF fiducial region unless a QCD correction is applied to the W+jets control sample. This (approximate) double counting arises due to adding QCD estimates in the anti-id+anti-id region, extrapolated with the fake factor product, once with the dijet, once with the Z+jets fake factor. The full lepton fake factor estimate is thus obtained by adding together the aforementioned QCD estimate and a W+jets estimate, from which the QCD contribution in the id+anti-id region has been subtracted. Consequently, an additional systematics is considered on the fake estimation in the VBF channel. It is defined as the total QCD correction and ranges from 15% to 33% depending on a phase space region.

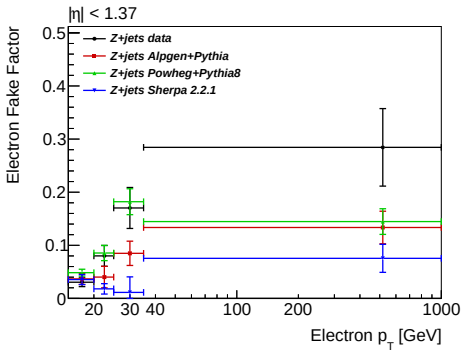

(a) e: $|\eta| < 1.37$

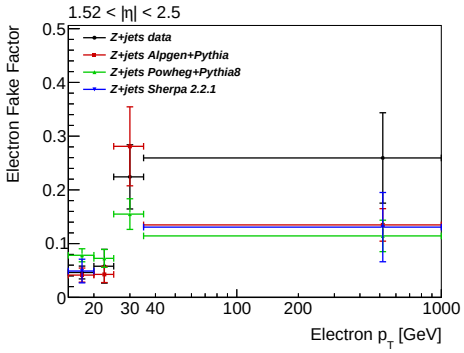

(b) e: $1.52 < |\eta| < 2.5$

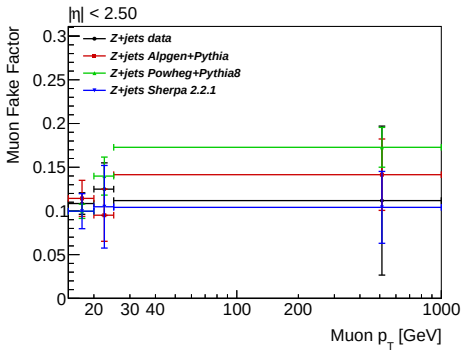

(c) μ: $|\eta| < 2.5$

Figure 4.5: Differential distributions of the electron and muon fake factors as a function of the fake candidate transverse momentum for each pseudo-rapidity bin. Monte Carlo expectations from POWHEG, ALPGEN and SHERPA are also shown. The uncertainties are statistical only. Figure taken from Reference [7].

4.7 Statistical analysis

The compatibility of the background-only hypothesis with the observed data is measured using Maximal Likelihood (ML) method with a test statistics based on profile likelihood ratio. This procedure is standard for all Higgs boson measurements in ATLAS, I will therefore outline it below.

The construction of this test statistics in the ML method proceeds as follows: The parameter of interest in the statistical fit is the signal strength μ. Signal strength is defined as the ratio between the measured cross-section of a chosen model (either SM or BSM) an its corresponding theoretical prediction. A kinematical variable x, whose distribution is a fit input, is given by a histogram X consisting of N bins. In case of analyses making use of event yields only, N=1. Systematical uncertainties are included in the fit as nuisance parameters (NPs), $\overrightarrow{\theta}$.

The likelihood function for a parameter of interest μ and a set of nuissance parameters $\overrightarrow{\theta}$ is a product of probability density functions f_i for each bin of X.

$$L(\mu, \overrightarrow{\theta}) = \Pi_{i=1}^{N} f_i(\mu, \overrightarrow{\theta}). \tag{4.3}$$

The likelihood $L(\mu, \overrightarrow{\theta})$ is the product of terms of the Poisson probabilities for all bins. Nuisance parameter constraints are given by either Gaussian, log-normal, or Poisson distributions. They have been established by other experimental measurements (for example jet energy scale), from control regions of current measurements (background normalisations) or theory calculations (QCD scale uncertainties of cross-sections). Based on (4.3), a test statistics called profiled likelihood ratio is constructed to test a given value of the signal strength μ:

$$\lambda(\mu) = \frac{L(\mu, \overrightarrow{\hat{\theta}})}{L(\hat{\mu}, \overrightarrow{\hat{\theta}})}. \tag{4.4}$$

Here, the denominator is an unconditionally maximised likelihood in terms of both μ and $\overrightarrow{\theta}$, with $\hat{\mu}$ and $\overrightarrow{\hat{\theta}}$ being ML estimators of μ and $\overrightarrow{\theta}$, respectively. The numerator is a likelihood maximised for a given value of μ with a set of nuissance parameters $\overrightarrow{\hat{\theta}}$ (conditional ML estimator for $\overrightarrow{\theta}$). This statistics is asymptotically equivalent to χ^2 [92].

Due to the presence of bins with low event yields, typical for measuring rare processes, all the NPs describing the systematic uncertainties are incor-

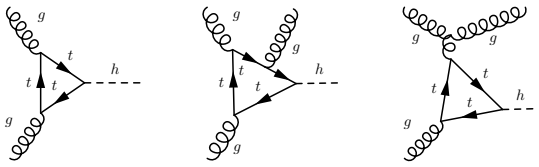

Figure 4.6: Example Feynman diagrams contributing to ggF +0j (left) and ggF+1j (middle and right) Higgs production.

porated into the fit using a log-normal constraint. In this way, the expected event counts remain positive for all values of the corresponding NPs.

In order to avoid potential biases in the data analysis, all data in the signal region is blinded until the final stage of each study. The expected performance of each fit is studied using the so-called Asimov datasets [92]. This is a "representative" dataset obtained with Monte Carlo simulations of signal and background processes, on which a ML estimate of the parameter returns exactly the median of the ensemble expectation with a single fit. The Asimov dataset allows therefore the study of the fit model, such as constraints on the nuisance parameters and their correlations, that could be obtained with the expected data distributions. In the following, all "expected" results are obtained using the Asimov dataset, whereas results of fits to data are labelled "observed".

4.8 Cross-section measurements in gluon fusion

Higgs boson production via gluon fusion (ggF) features the largest cross-section according to the SM predictions. Additional jets are produced through QCD radiation from the initial state partons or from the top quark loop, as shown in the example Feynman diagrams in Fig. 4.6. In the following I focus on the measurement of Higgs boson production through gluon fusion, accompanied by 0 and 1 jets, ggF+0j and ggF+1j, based on Ref. [7].

Event selection requirements, specific for ggF+0j and ggF+1j categories, are given in Table 4.3. They are applied after the preselection criteria described earlier. In the ggF+0j category, the track-based missing energy is required to be larger than 20 GeV. In order to supress top quark back-

ground, events featuring jets containing b-hadrons (b-jets) are vetoed in both categories. Heavy flavour jets with $|\eta| < 2.5$ and $p_T < 20$ GeV are identified based on the information on the track impact parameters and secondary vertices using a multivariate techniques [93]. The adopted working point provides an average 85% b-jet tagging efficiency, 32% and and 3% misidentification rate for c-jets and light-flavour (u-, d-, s-quark and gluon) jets, respectively. Further, the kinematical properties of leptons are exploited: the di-lepton invariant mass m_{ll} must be larger than 55 GeVand the azimuthal angle between lepton momenta, $\Delta\phi_{ll}$ cannot exceed 1.8. In the ggF+0j category, lower bounds are required on the azimuthal angle between missing transverse energy E_T^{miss} and the dilepton system, $\Delta\phi(ll, E_T^{miss})$ and the transverse momentum of the dilepton system, p_T^{ll}. The ggF+1j category is defined through $\max(m_T^l)$, which is the larger of the transverse masses of the leading and subleading lepton. In order to reject background events from $Z \to \tau\tau$ production, invariant mass of two leptonically decaying τ leptons, $m_{\tau\tau}$, is estimated from light lepton momenta using the collinear approximation [94]. This invariant mass must differ from the Z boson mass by at least 25 GeV.

Table 4.3: Event selection criteria used to define the signal regions in the ggF+0j and ggF+1j categories.

Category	$N_{\text{jet}} = 0$	$N_{\text{jet}} = 1$
Background rejection	$N_{b\text{-jet}} = 0$	
	$p_T^{miss}, > 20\text{GeV}$	
	$\Delta\phi(\ell\ell, E_T^{miss}) > \pi/2$	$\max(m_{\text{T}}^{\ell}) > 50\text{GeV}$
	$p_T^{\ell\ell} > 30\text{GeV}$	$\lvert m_{\tau\tau} - m_Z \rvert \leq 25\text{GeV}$
$H \to WW^* \to \ell\nu\ell\nu$	$m_{\ell\ell} < 55\text{GeV}$	
topology	$\Delta\phi_{\ell\ell} < 1.8$	

The largest backgrounds: WW, (single- and double-) top quark production, and $Z \to \tau\tau$ are estimated using control regions (CRs). They are defined ortogonally to the signal region (typically by inverting one or more signal selection requirements) so that the signal contribution in the control regions is negligible. Likewise, contribution from other processes should be small to achieve low extrapolarion uncertainties. From the estimate of event yields in control regions, MC simulations of the relevant processes are cor-

rected with normalisation factors. These factors are then applied to improve the estimation of backgrounds in the signal regions. Selection criteria of control regions used in both analysis are listed in Table 4.4. For the WW CR the selection on invariant di-lepton mass is inverted. The top quark CR is defined for both categories by replacing the b-jet veto with a b-jet requirement. For $Z\gamma^* \to \tau\tau$ CR corresponding to ggF+0j category $\Delta\phi_{ll}$ selection orthogonal to the SR is used. Similarly, for the CR corresponding to ggF+1j, $m_{\tau\tau}$ selection is inverted. The resulting normalisation factors are: $N^{0j}_{WW} = 1.06 \pm 0.09$, $N^{0j}_{top} = 0.99 \pm 0.17$, $N^{0j}_{Z\gamma^*} = 0.84 \pm 0.04$ and $N^{1j}_{WW} = 0.97 \pm 0.17$, $N^{1j}_{top} = 0.98 \pm 0.08$, $N^{1j}_{Z\gamma^*} = 0.90 \pm 0.12$ for the ggF+0j and ggF+1j categories, respectively.

Systematical uncertainties are classified into statistical, experimental and theoretical. Dominant sources of experimental uncertainties in this analysis are related to tagging heavy flavour jets, modelling of pile-up, jet energy scale and resolution, identification and isolation of leptons and energy scale and resolution of leptonic momenta. The largest theoretical uncertainties are related to modelling of the signal, WW and top quark processes. They are assessed by a comparison between nominal and alternative event generators, underlying event and parton shower models. Table 4.1 indicates, which simulation tools were used for each process. For the prediction of diboson processes: WZ, ZZ, $V\gamma^*$, and $V\gamma$ production (labelled collectively as VV), variations of the matching scale between matrics elements and parton showers are considered instead of an alternative generators. In addition, the effects of QCD factorisation and renormalisation scale variations and parton distribution functions (PDF) model uncertainties are evaluated.

The signal and the background modelled contributions are fitted to the data in signal and control regions simultaneously using the profile likelihood method. The fit maximises a likelihood function using scaling parameters that multiply predicted event yields of the signal processes. Systematical uncertainties enter the fit as the nuissance parameter.

Transverse mass is used as a discriminant variable in both categories. Figures 4.7 and 4.8 present the m_T distribution in signals and backgrounds for the signal and control regions, respectively.

Table 4.4: Event selection criteria used to define the control regions (CRs), in addition to "preselection" defined earlier.

CR	$N_{\text{jet}} = 0$	$N_{\text{jet}} = 1$
WW	$55 < m_{\ell\ell} < 110$GeV $\Delta\phi_{\ell\ell} < 2.6$ $N_{\text{b-jet, }(\ p_T > 20\text{ GeV})} = 0$	$m_{\ell\ell} > 80$GeV $\lvert m_{\tau\tau} - m_Z \rvert > 25$GeV $N_{\text{b-jet, }(\ p_T > 20\text{ GeV})} = 0$ $m_{\text{T}}^{\ell} > 50$GeV
top quark	$N_{\text{b-jet, }(20\text{ GeV} < p_T < 30\text{ GeV})} > 0$ $\Delta\phi(\ell\ell, E_T^{miss}) > \pi/2$ $p_T^{\ell\ell} > 30$GeV $\Delta\phi_{\ell\ell} < 2.8$	$N_{\text{b-jet, }(\ p_T > 30\text{ GeV})} = 1$ $N_{\text{b-jet, }(20\text{ GeV} < p_T < 30\text{ GeV})} = 0$ $\max(m_{\text{T}}^{\ell}) > 50$GeV $m_{\tau\tau} < m_Z - 25$GeV
$Z\gamma^* \to \tau\tau$	no p_T^{miss} requirement $m_{\ell\ell} < 80$GeV $\Delta\phi_{\ell\ell} > 2.8$	no p_T^{miss} requirement $m_{\ell\ell} < 80$GeV $m_{\tau\tau} > m_Z - 25$GeV $N_{\text{b-jet, }(\ p_T > 20\text{ GeV})} = 0$

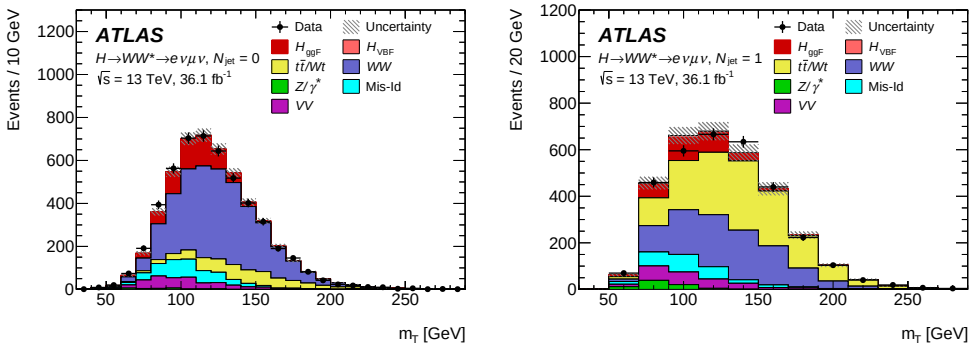

(a) (b)

Figure 4.7: Post-fit m_T distributions in the ggF +0j (a) and ggF+1j (b) signal regions. Signal and background yields are fixed from the fit. The shaded areas depict the statistical and systematical uncertainty of both signal and background contributions.

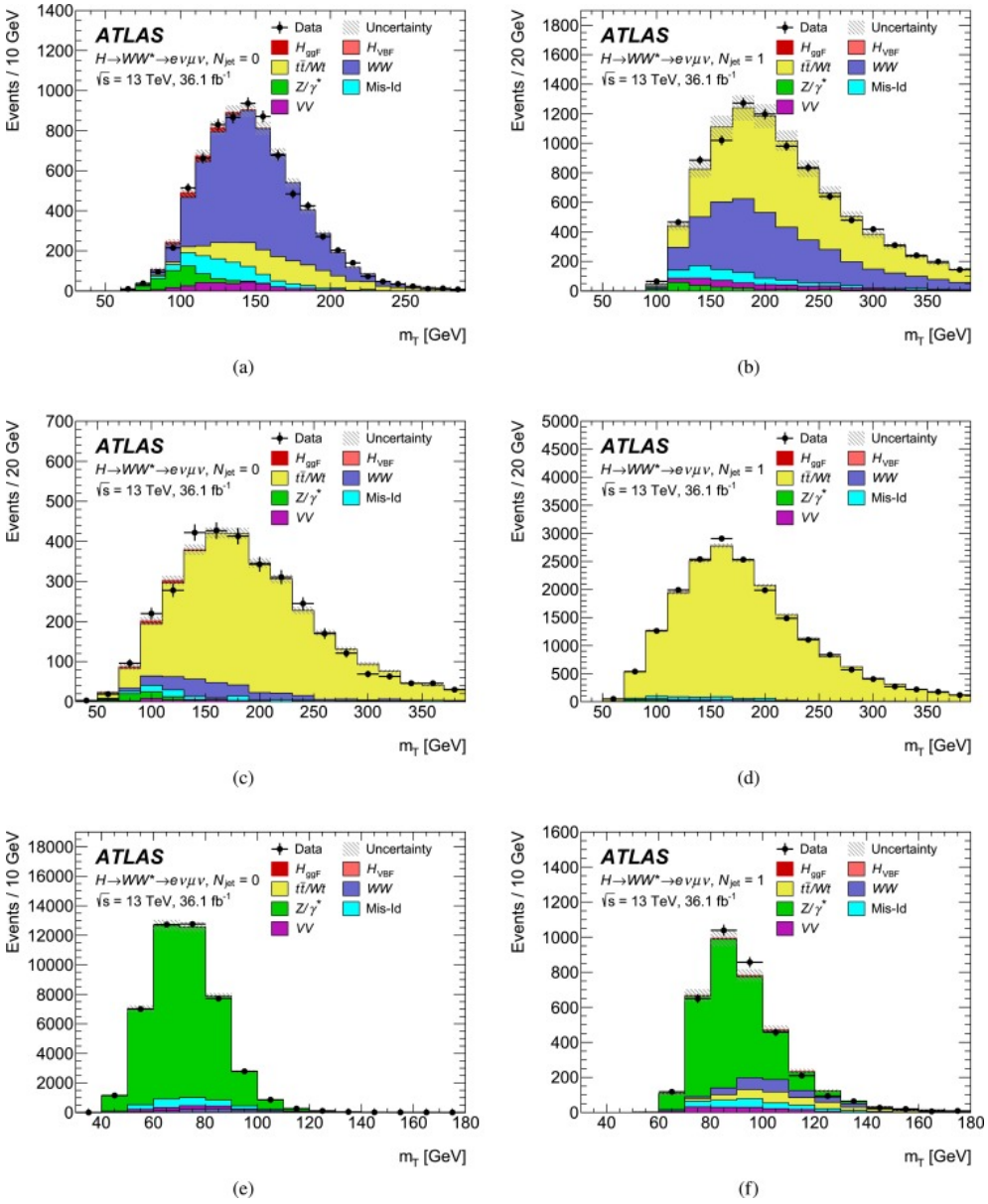

Figure 4.8: Post-fit m_T distributions in (from top to bottom) top, WW and Z+jets control regions in ggF +0j (left) and ggF+1j (right) categories. The shaded areas depict the statistical and systematical uncertainty of both signal and background contributions.

Table 4.5: Post-fit event yields in MC and data in the ggF +0j and ggF+1j signal regions.

Process	ggF +0j			ggF +1j		
ggF Higgs boson production	629	±	110	285	±	51
VBF Higgs boson production	7	±	1	31	±	2
WW	3016	±	203	1053	±	206
VV	333	±	38	208	±	32
Single and double top quark	588	±	130	1397	±	179
Misidentified (fakes)	447	±	77	234	±	49
$Z\gamma^*$	27	±	11	76	±	24
Total	5067	±	80	3296	±	61
Data	5089			3264		

4.8.1 Results

For the cross-section measurement the two channels were combined and the resulting post-fit m_T distribution is shown in the upper panel in Fig. 4.9. The lower panel demonstrates the difference between the data and the estimated background (black dots) overlaid on the corresponding distribution for a SM Higgs boson with $m_H = 125$ GeV(red histogram). The dashed band shows the total uncertainty of the simulated signal and background contributions.

Event yields obtained after fitting procedure together with these observed in data are given in Table 4.5. The sum of all simulated contributions may differ from the total value due to rounding. The quoted uncertainties include the theoretical and experimental systematic sources and those due to sample statistics. Due to correlations among uncertainties, the total uncertainty differs from the sum in quadrature of the uncertainties of individual processes. Measured inclusive cross-section times branching ratio yields:

$$\begin{aligned}\sigma_{ggf} \cdot \mathcal{B}(H \to WW^*) &= 11.4^{+1.2}_{-1.1}(\text{stat.})^{+1.2}_{-1.1}(\text{theo syst.})^{+1.4}_{-1.3}(\text{exp syst.})\ \text{pb} \\ &= 11.4^{+2.2}_{-2.1}\text{pb}\end{aligned}$$

In the second line all uncertainties were added. This measurement is in agreement with the SM prediction.

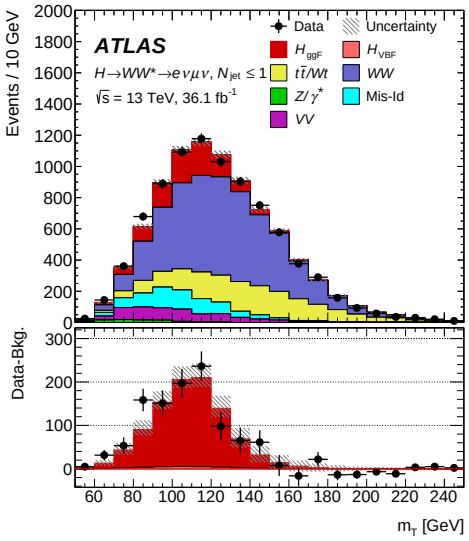

Figure 4.9: Combined post-fit m_T distribution in the ggF +0j and ggF+1j signal regions (top panel) and the difference between the data and the estimated background compared to the SM Higgs boson prediction (bottom panel).

4.9 Measurements in the VBF channel

This section presents two measurements related to the VBF Higgs boson production: the cross-section times $H \to WW^*$ branching ratio and the measurement of Higgs couplings to polarised W and Z bosons. Datasets and event selection will largely be common, whenever analysis techniques of the latter measurement differ, is indicated.

4.9.1 Event selection

The dominant backgrounds in the VBF signal category are (see Figure 4.4): top quark production (single top and $t\bar{t}$), amounting to $\sim 55\%$ of the events after preselection, WW ($\sim 20\%$), Drell-Yan $Z\gamma^* \to \tau\tau \to \ell\nu\nu\ell\nu\nu$($\sim 15$ %). Other important contributions originate from di-boson (such as WZ, ZZ and $W\gamma^*$), $Z\gamma^* \to ee/\mu\mu$ and W+jets processes. In this section I will discuss kinematical properties of the signal and dominant background processes, present the signal selection requirements and the construction of control re-

gions for top-quark and Z+jets backgrounds will be outlined.

4.9.2 Kinematics of the VBF process

VBF Higgs boson production features two energetic jets in the forward regions (in opposite directions) and no QCD emissions in the central region of the detector. The leptons from the final state, on the other hand, are located in a central part of the detector. Using this property of the signal, the following kinematical variables have been constructed in order to separate signal-like from background-like events:

- Pseudorapidity gap: $\Delta\eta_{jj} = \eta_{j_1} - \eta_{j_2}$.

  It is large for the signal and small for the background processes.

- Invariant di-jet mass m_{jj}, large in the VBF Higgs production processes.

- The emission of the two charged leptons from the $H \to WW^* \to e\nu\mu\nu$ decay into the central part of the detector is translated into an observable which is called the outside lepton veto (OLV) and is defined via:

$$\text{OLV} = 2 \cdot \left| \frac{\eta_\ell - \bar{\eta}}{\eta_{j_1} - \eta_{j_2}} \right|,$$

  where $\bar{\eta} = (\eta_{j_1} + \eta_{j_2})/2$ is the average η of the two leading jets. OLV < 1 for leptons within the (pseudo)-rapidity gap between the two VBF jets and OLV > 1 for leptons outside the (pseudo)-rapidity gap between the VBF jets.

  The motivation behind using this variable is the following: OLV measures if each lepton is more central than “the average of the two jets" by comparing its OLV with 1. Since in the VBF both jets have typically opposite sign pseudorapidities, $\bar{\eta}$ is close to 0 and the denominator is large (typically larger than 1). The larger the denominator, the larger η-space is allowed for a central lepton. If, on the other hand, $|\eta_\ell| > |\bar{\eta}| + |\eta_{j_1} - \eta_{j_2}|/2$, this lepton lies in more forward region than both jets and its OLV is larger than 1.

- Evaluating the OLV for both charged leptons allows a determination of the lepton centrality:

$$\eta_{\text{lep}}^{\text{centrality}} = \text{OLV}_{\ell_1} + \text{OLV}_{\ell_2}. \tag{4.5}$$

  For the VBF signal OLV_{ℓ_1} and OLV_{ℓ_2} are small and therefore $\eta_{\text{lep}}^{\text{centrality}}$ smaller than 1 is preferred for the signal topology.

- Central Jet Veto (CJV).

  VBF Higgs boson production is mediated by exchange of electroweak bosons. Therefore, soft QCD radiation is suppressed in this process, resulting in no additional jets in the central rapidity region. CJV means that all events featuring with additional jets (whose transverse momenta are larger than 20 GeV) in the rapidity gap between the two leading jets are rejected.

- The total transverse momentum, p_T^{tot}, defined as the vectorial sum over transverse momenta of the two leptons, jets passing the good-jet definition criteria, and the missing transverse energy: $p_T^{tot} \equiv \mathbf{p}_T^{l_1} + \mathbf{p}_T^{l_2} + E_T^{miss} + \sum \mathbf{p}_T^{jet}$. This variable is efficient in discriminating against dileptons associated with soft jets.

- The sum of the invariant masses of all four possible lepton-jet pairs, $\sum_{l,j} M_{lj}$. It has a higher value for the VBF signal than for the backgrounds due to a large opening angle between leptons and the jets in the VBF.

- The mass of di-τ system is estimated based on the reconstructed charged leptons.

  Under the assumptions of the Collinear Approximation Method [94], valid for heavy resonances with large transverse momenta decaying into τ leptons, the charged leptons and neutrinos emitted in the decay of τ leptons are collinear with each other. For the actual τ decays, the missing transverse momentum vector lies between the two observable light leptons. Therefore, the τ momentum fractions carried by an electron or muon must yield $0 < x_{\tau_{1,2}} < 1$. For non-resonant backgrounds, such as the WW and $t\bar{t}$ the collinear approximation is not valid because the

decaying heavy particles do not receive large boosts with respect to their rest frame. In this case, attempting to reconstruct a $\tau^+\tau^-$ pair results in either $x_{\tau_1} < 0$ or $x_{\tau_2} < 0$ for a significant fraction of the events.

If $x_{\tau_{1,2}}$ are physical, the invariant mass $m_{\tau\tau}$ is computed as:

$$m_{\tau\tau} = \frac{m_{ll}}{\sqrt{x_{\tau_1} x_{\tau_2}}}. \tag{4.6}$$

In such cases, restricting $m_{\tau\tau}$ from above helps to suppress $Z \to \tau\tau$ and $H \to \tau\tau$ backgrounds.

4.9.3 Signal Region

After preselection criteria listed in Section 4.5, the signal region is defined by the following additional equirements:

- outside lepton veto (OLV) for all leptons,
- central jet veto (CJV) for all jets with $p_T > 20$ GeV,
- $m_{\tau\tau} < m_Z - 25$ GeV.

For the final signal selection, boosted decision trees (BDTs) are used. A BDT uses a collection of phase space cuts resulting in non-linear phase-space boundaries. These cuts are optimised to classify given events as originating from the signal or one of the background processes. Cuts optimisation is done iteratively in a phase called training. Signal events should be placed in a signal-dominated leaf, while background events should end up in a background-dominated leaf. After the initial tree is built, each consecutive tree is supposed to improve misidentifications encountered in a previous one. This procedure is applied iteratively until there is a collection of a specified number of trees. Combining single trees into a stronger classifier is known as boosting. A BDT output discriminant is taken from all grown trees. The output distribution of the BDT is used as discriminant variable in the VBF cross-section measurement. In this analysis the BDT binning has been found iteratively in order to optimise signal significance S defined as:

$$S = \frac{N_S}{\sqrt{N_S + N_B + \Delta N_B^2}}, \tag{4.7}$$

where N_S denotes the number of signal events, N_B the total number of background events and ΔN_B is the statistical uncertainty of the backgrounds. The term ΔN_B is included in the definition of significance because the analysis was found to be highly affected by statistical uncertainty of the Monte Carlo simulations. This procedure has led to the four bins, within the range $[-1, 1]$, with bin boundaries $[-1, 0.26, 0.61, 0.86, 1]$. Background-like events are classified in the lower bins of the BDT distribution, while signal-like events are placed in the fourth and third bin. The expected signal-to-background ratio in the last bin is approximately 0.6.

For the implementation of the BDT in the measurements in the VBF channel described in this section, the scikit-learnhas been used. This is an open-source library for the Python programming language, featuring several machine learning algorithms[2]. Simulated VBF signal events, and top-quark, WW and Z/γ^*+jets and ggF Higgs production backgrounds are used for training. The associated production (VH) as well as W+jets events are not included in the training due to their very low statistics. The optimal set of learning parameters is summarised in Table 4.6. In order to avoid overtraining, the events are split in two sub-sets and the BDT is trained twice.

Table 4.6: Optimised BDT parameters used in the training.

Parameter	Value	Range
Boosting algorithm	Gradient	–
Maximum tree depth	5	[3,16]
Number of trees	200	[200,100]
Minimum number of events required per node	5%	[5%,20%]
Learning rate	0.1	–

BDTs are applied after preselection of events. Eight kinematical variables are used as input variables in the BDT: $\Delta\phi_{\ell\ell}$, $m_{\ell\ell}$, m_{T}, Δy_{jj}, m_{jj}, p_T^{tot}, $\sum_{\ell,j} m_{\ell j}$, and $\eta_{\mathrm{lep}}^{\mathrm{centrality}}$. These variables were ranked by counting in how many nodes each variable was used and by weighting these usages by both the gain in separation at each node and the number of events in each node. The resulting ranking is summarised in Table 4.7. The most discriminating variables, m_{jj} and Δy_{jj}, are related to the VBF signal topology. Other

[2]The library can be downloaded from https://scikit-learn.org/ .

variables are related to the kinematical properties of leptons originating from the Higgs boson decay to WW^*, as discussed in the previous section.

Table 4.7: Ranking of the BDT training variables for the BDT trained on the even numbered events.

Ranking	Variable	Importance [%]
1	$\mathrm{m_{jj}}$	19
2	$\Delta \mathrm{y_{jj}}$	16
3	$\mathrm{m_{ll}}$	14
4	m_T	14
5	$\eta_{\mathrm{lep}}^{\mathrm{centrality}}$	13
6	$\Delta\phi_{\mathrm{ll}}$	10
7	$\sum_{\mathrm{l,j}} \mathrm{M_{lj}}$	8
8	$\mathrm{p_{tot}^{T}}$	7

4.9.4 Estimation of backgrounds

Estimation of fake lepton backgrounds from $W+$ jets processes in the VBF fiducial region follows a data driven technique described in Section 4.6. The normalisations of backgrounds due to $Z/\gamma^* \to \tau\tau$ production in association with two jets (featuring both QCD and EW Z production) as well as single- and double- top quark production are estimated using control regions defined in Table 4.8. The number of b-quark jets, N_{b-jets}, used to define signal and control regions, is estimated in each phase space region using a multivariate algorithm MV2C10 with 85% working point. These regions were constructed in a way to maximise the contribution of the relevant background process and make them orthogonal to the signal region and to each other. Number of events in control regions allows the extraction of normalization factors that are then applied to both the signal and control regions. Other backgrounds are evaluated using the Monte Carlo predictions only. Unlike the ggF analysis, the use of a dedicated control region for the WW production processes did not improve the estimation of this background.

Table 4.8: Event selection criteria, applied after preselection, used to define the signal and control regions in the VBF analysis. Definitions of symbols and abbreviations are given in the text.

	Signal region	$Z \to \tau\tau$ CR	top-quark CR
Number of b-jets	$N_{b-jets} = 0$	$N_{b-jets} = 0$	$N_{b-jets} = 1$
Selection	$m_{\tau\tau} < 66.2$GeV	$\lvert m_{\tau\tau} - m_Z \rvert < 25$GeV	–
	–	$m_{ll} < 80$GeV	–
	OLV applied	OLV applied	
	CJV applied	CJV applied	–

Top quark control region

The top control region (CR) is defined as exactly the same as the SR, with a b-jet veto replaced by a requirement of one and only one b-tagged jet ($N_{b-jet} = 1$) identified using the MV2C10 algorithm at 85% efficiency. While there are typically 2 b-jets present in the top-quark background, composed predominantly of $t\bar{t}$ pairs, the requirement of a single b-tagged jet brings the flavour composition of tag jets closer to the one in the SR. The purity of the top control region is of about 96%.

The top background in the SR is corrected by the normalization factors (NF) derived in the top CR. The resulting NF is $1.00^{+0.06}_{-0.05}$.

$Z(\to \tau\tau)$+jets control region

The $Z \to \tau\tau$ control region definition differs from the signal region by the inversion of the cut on the invariant mass of the two tau leptons and is required to be $|m_{\tau\tau} - m_Z| \leq 25$ GeV.

Furthermore, the invariant mass of the two leptons: $m_{ll} < 80$ GeV. The OLV and CJV vetos are applied in the same way as in the signal region.

The resulting NF is $0.94^{+0.21}_{-0.18}$.

4.9.5 Estimation of uncertainties

The effects of the systematic uncertainties on the expected signal and background yields in the signal and control regions are evaluated. In addition,

the effects of the uncertainties on the shapes of the BDT response and $\Delta\phi_{jj}$ distributions are considered. These effects are evaluated by individually comparing the nominal distribution with those corresponding to up and down variations of a particular uncertainty.

Experimental uncertainties The dominant experimental uncertainties for both analyses are related to the b-tagging efficiency [93], the jet energy scale and resolution [95], the modelling of pile-up activity, and the estimation of the misidentified-lepton background [7]. Smaller uncertainties are due to the lepton momentum scale and resolution, the lepton identification and isolation criteria [82, 96, 97], the measurement of missing transverse momentum [98], and the luminosity measurement [31]. The luminosity uncertainty is only applied to those processes that are normalised to theoretical predictions.

Theory uncertainties The theoretical uncertainties are assessed by a comparison between nominal and alternative event generators, underlying event and parton showers models, as indicated in Table 4.1. For the prediction of di-bosons (WZ, ZZ, $W\gamma^*$, $Z\gamma^*$, $W\gamma$ and $Z\gamma$) production, variations of the matching scale are considered instead of an alternative generator. In addition, the effects of QCD factorisation and renormalisation scale variations and PDF model uncertainties are evaluated.

Uncertainties related to MC mismodeling It is observed that MC simulations overestimate the data for high invariant di-jet mass, m_{jj}, after event pre-selection. Therefore, all background events are reweighted such that the data and MC agree in the m_{jj} distribution at this event selection stage. The resulting shape difference of BDT distribution between the original and reweighted datasets is used to compute the uncertainty on the m_{jj} modeling. This additional shape systematic is applied in the VBF SR for all the background processes and added as an additional nuisance parameter to the fit. This non-closure is on the order of a few percent at low m_{jj} values and ranges up to 15% for m_{jj} values above 1 TeV. The impact of this uncertainty on the final results is small with respect to the statistical uncertainties.

Table 4.9: Post-fit event yields in MC and data in the VBF inclusive signal region.

Process	Event yields in the SR
VBF Higgs boson production	28 ± 16
ggF Higgs boson production	42 ± 16
WW	400 ± 60
VV	70 ± 12
Single and double top quark	1270 ± 80
Misidentified (fakes)	90 ± 30
$Z\gamma^*$	280 ± 40
Total	2170 ± 50
Data	2164

4.9.6 Cross-section measurement

The VBF cross-section is obtained from a simultaneous statistical analysis of the data samples in the SR and all CRs. The results are obtained by maximising a likelihood function in a fit using scaling parameters multiplying the predicted total production cross-section of each signal process and applying the profile likelihood method. The systematic uncertainties enter the fit as nuisance parameters in the likelihood function.

Table 4.9 shows the post-fit event yields in the SR. In Figure 4.10 the post-fit distribution of BDT score with the signal and the background modelled contributions is shown. The signal-rich bins 3 and 4 are shown in a separate scale.

The result of the log likelihood minimization in data in four BDT bins as well as in the control regions yields a best-fit value for the signal strength of $\mu_{VBF} = 0.69^{+0.31}_{-0.29}$ (stat.) ± 0.24(sys.) $= 0.69^{+0.39}_{-0.37}$. This corresponds to an observed (expected) signal significance of 1.9 (2.7), assuming a SM signal.

Those numbers were obtained by assuming SM event yields of gluon fusion Higgs production (ggF). Allowing the normalisation of this background to float in the fit results in the best-fit value of vector boson fusion Higgs production signal strength $\mu_{VBF} = 0.87^{+0.31}_{-0.29}(\text{stat.})^{+0.57}_{-0.55}(\text{sys.}) = 0.87^{+0.63}_{-0.65}$. The resulting normalisation factor for ggF equals 0.12 ± 2.41. This corresponds

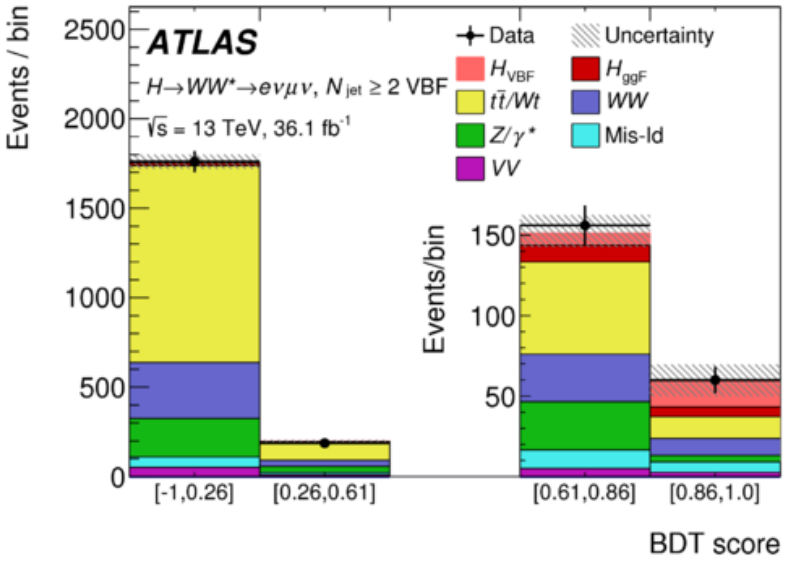

Figure 4.10: Post-fit distribution of BDT score in the VBF signal region. Signal and background yields are fixed from the fit. The shaded areas depict the statistical and systematical uncertainty of both signal and background contributions.

to an observed (expected) signal significance of 1.4 (1.6), in case of a SM signal.

4.10 Polarisation measurement

4.10.1 Parametrisations of Higgs couplings to polarised W and Z bosons

While measurements of $\sigma_{\text{VBF}} \cdot \mathcal{B}_{H\to WW}$, described in Section 4.9.6, are consistent with the SM, the couplings of the Higgs boson to the massive electroweak gauge bosons that are polarisation-dependent, have so far not been studied directly. $W^{\pm}$ and Z^0 bosons have three polarisations: two transverse and one longitudinal. By contrast, photon has only two transverse polarisations in physical gauges (Coulomb gauge for example). Longitudinal polarisations of the massive bosons cannot be “gauged away". In fact, they emerge from massless degrees of freedom of the Higgs boson and are therefore closely re-

lated to the mechanism of electroweak symmetry breaking. The electroweak symmetry breaking already fixes the gauge in such a way that the longitudinal polarisations are non-vanishing. The strength of the Higgs boson coupling to longitudinally polarised W bosons ensures the unitarity of the SM. The SM predicts no difference between transverse and longitudinal couplings. Therefore, any deviation from the SM values in either coupling is a hint that the Higgs field is not associated with a fundamental scalar particle but is an effective field arising from new dynamics. For example, Higgs compositeness models [56, 99] predict more degrees of freedom, allowing the Higgs boson couplings to electroweak bosons to deviate from their SM values.

To parametrise BSM effects in the Higgs boson couplings to longitudinally and transversally polarised massive electroweak bosons, polarisation-dependent coupling-strength scale factors are used as defined in Ref. [20] as

$$a_{\mathrm{L}} = \frac{g_{HV_{\mathrm{L}}V_{\mathrm{L}}}}{g_{HVV}}\,,\ a_{\mathrm{T}} = \frac{g_{HV_{\mathrm{T}}V_{\mathrm{T}}}}{g_{HVV}}\,. \tag{4.8}$$

The parameter g_{HVV} is the SM HVV coupling strength and $g_{HV_{\mathrm{L}}V_{\mathrm{L}}}$ and $g_{HV_{\mathrm{T}}V_{\mathrm{T}}}$ are the measured polarisation-dependent couplings. In the SM, $g_{HV_{\mathrm{L}}V_{\mathrm{L}}} = g_{HV_{\mathrm{T}}V_{\mathrm{T}}} = 1$ as the Higgs boson couplings are insensitive to polarisations. The polarisations of the vector bosons in equation (4.8) are defined in the Higgs boson rest frame so that mixed-polarisation couplings $HV_{\mathrm{L}}V_{\mathrm{T}}$ do not contribute to $\sigma_{\mathrm{VBF}} \cdot \mathcal{B}_{H\to WW}$. Other BSM effects, such as the presence of new particles, or other couplings modifications, are not considered. Within the SM ($a_{\mathrm{L}} = a_{\mathrm{T}} = 1$).

This set of couplings is convenient for experimental measurements and Monte carlo simulations. Dedicated MC signal samples have been generated in MadGraph5_aMC@NLO 2.4.2 generator [66, 100]. Helicity amplitudes used in the matrix element generation of the Higgs boson production and decay were internally boosted in the Higgs boson rest frame, modified, and boosted back to the detector frame following the prescription in Ref. [20]. Signal samples were produced for the following benchmark scenarios: $(a_L, a_T) \in \{(1,1), (1,1.3), (1.3,0.7), (1.3,1), (0.7,1.3)\}$.

The polarisations depend on the measurement frame and therefore the above description is not Lorentz invariant and as such cannot be described in the Lagrangian framework. Instead, the coupling strength modifiers a_{L} and a_{T} can be related to (Lorentz invariant) pseudo-observables (POs). Pseudo Observables provide a parametrisation of possible variations from the SM in Higgs boson production and decay processes, expressed in terms of measur-

able, well defined in terms of quantum field theory quantities [9, 101–105]. The Higgs POs are defined based on a decomposition of on-shell amplitudes involving the production and/or decay of the Higgs boson and a momentum expansion, which is valid under the assumption that there are no new light particles (and thus no additional poles of the new propagators need to be considered).

The mapping is performed using approximations described below. The most general parametrisation of the VBF $h \to WW^*(l\nu l\nu)$ process includes six POs affecting HVV vertices: $\kappa_{WW}, \kappa_{ZZ}, \epsilon_{WW}, \epsilon_{ZZ}$, ϵ^{CP}_{WW}, ϵ^{CP}_{ZZ}. Assuming a CP even Higgs, $\epsilon^{CP}_{WW} = \epsilon^{CP}_{ZZ} = 0$. Under the assumptions of custodial symmetry, the following identities hold (see Ref [105]):

(*) $\epsilon_{WW} = \cos(\theta_W)^2\epsilon_{ZZ} + 2\sin(\theta_W)\cos(\theta_W)\epsilon_{Z\gamma} + \sin(\theta_W)^2\epsilon_{\gamma\gamma}$

(**) $\kappa_{WW} - \kappa_{ZZ} = -2/g(\sqrt{2}\epsilon_{W_L^{e_i}} + 2\cos(\theta_W)\epsilon_{Z_L^{e_i}})$

Additionally assuming no new physics in boson-fermion couplings Wff and Zff one gets $\epsilon_{W_L^{e_i}} = \epsilon_{Z_L^{e_i}} = 0$ and from (**) it follows that $\kappa_{WW} - \kappa_{ZZ} = 0$. Since neither $H\gamma\gamma$ nor $HZ\gamma$ couplings are present in the signal and background process, we can assume a single coupling, namely: $\epsilon_{\gamma\gamma} = \epsilon_{ZZ} = \epsilon_{Z\gamma}$. As a result, $\epsilon_{WW} = \epsilon_{ZZ}$. We will denote in the following $\kappa_{WW} = \kappa_{ZZ} \equiv \kappa_{VV}$ and $\epsilon_{WW} = \epsilon_{ZZ} \equiv \epsilon_{VV}$. The corresponding effective Lagrangian describing VBF Higgs boson production has the form:

$$\mathcal{L} = \kappa_{VV}\left(\frac{2m_W^2}{v}HW^+_\mu W^{-\mu} + \frac{m_Z^2}{v}HZ_\mu Z^\mu\right) - \frac{\varepsilon_{VV}}{2v}\left(2HW^+_{\mu\nu}W^{-\mu\nu} + HZ_{\mu\nu}Z^{\mu\nu} + HA_{\mu\nu}A^{\mu\nu}\right), \tag{4.9}$$

where v is the Higgs vacuum expectation value. In the SM $\kappa_{VV} = 1$ and $\varepsilon_{VV} = 0$.

The Pseudo Observables are related to the coupling-strength scale factors a_{L} and a_{T} via the following equations:

$$\kappa_{VV} = a_{\mathrm{L}} - \Delta_{\mathrm{L}}(q_1, q_2)\varepsilon_{VV}\,, \quad \varepsilon_{VV} = \frac{a_{\mathrm{T}} - a_{\mathrm{L}}}{\Delta_{\mathrm{T}}(q_1, q_2) - \Delta_{\mathrm{L}}(q_1, q_2)}\,.$$

The functions $\Delta_{\mathrm{L}}(q_1, q_2)$ and $\Delta_{\mathrm{T}}(q_1, q_2)$ depend on the momenta of electroweak bosons q_1 and q_2 (either in the production or in the decay) according to:

$$\Delta_{\mathrm{L}} = \frac{m_H^2}{2m_W^2}\frac{4q_1^2q_2^2}{m_H^2(m_H^2 - q_1^2 - q_2^2)}\,, \quad \Delta_{\mathrm{T}} = \frac{m_H^2}{2m_W^2}\frac{m_H^2 - q_1^2 - q_2^2}{m_H^2}\,. \tag{4.10}$$

For this mapping to be exact for constant parameters a_L and a_T, $\Delta_{L,T}$ must be independent on the bosons' kinematics. In the approximate mapping adopted in this study, the estimation of values of parameters $\Delta_{L,T}$ was

based on simulations of the VBF signal discussed in Section 4.2. For every event, the values of q_1^2 and q_2^2 were extracted and inserted in formulae (4.10), forming distributions (histograms) of both formfactors. The maxima of the distributions were found at $\Delta_{\mathrm{L}}(q_1, q_2) = 0$ and $\Delta_{\mathrm{T}}(q_1, q_2) = 2$. This leads to the mapping adopted in the analysis:

$$\kappa_{VV} \simeq a_{\mathrm{L}}\,, \quad \varepsilon_{VV} \simeq 0.5 \cdot (a_{\mathrm{T}} - a_{\mathrm{L}})\,.$$

The above mapping was applied in the statistical analysis in the parametrisation of maximal log-likelihoods. Simulated signal events for various BSM coupling modifications in terms of Pseudo Observables was not yet available.

The above POs description focusses on VBF production and thus differs from the one used in Refs. [106, 107], in which couplings to leptons (ε_L, ε_R) and to Z bosons (κ_{ZZ}) are constrained using Higgs boson decays into four leptons, inclusively with respect to the production channels. Due to these technicalities, the two measurements cannot be statistically combined.

4.10.2 Kinematical properties of signals with modified couplings

Modifications of a_L and a_T coupling strength scale factors results in cross-section changes. For allowed polarisation combinations[3], $\sigma_{\mathrm{VBF}} \cdot \mathcal{B}_{H\to WW}$ is proportional to a linear combination of terms $a_{L,T}^4$ and $a_L^2 a_T^2$. The cross sections dependence on (a_L, a_T) couplings is shown in two dimensions Figure 4.11. The Standard Model prediction, $a_L = a_T = 1$, is marked with a star. The larger sensitivity to a_L stems from the fact that in the considered phase space helicity amplitudes with longitudinal polarisation vectors of the massive electroweak bosons are largest. Modifications to a_T, on the other hand, can be distinguished by shapes of kinematical distributions. The distribution sensitive to W and Z bosons polarisations in the initial state is the angular difference between two leading jets in the plane perpendicular to the beam, $\Delta\Phi_{jj}$. It is defined as $\Delta\Phi_{jj} = \phi_{j_1} - \phi_{j_2}$ if $\eta_{j_1} > \eta_{j_2}$, and $\Delta\Phi_{jj} = \phi_{j_2} - \phi_{j_1}$ otherwise, where j_1 is the highest-p_{T} jet and j_2 is the next-highest-p_{T} jet in the event.

The shape of $\Delta\Phi_{jj}$ distribution differs with $a_T - a_L$ as shown in Figure 4.12: the cases where $a_L = a_T$ resemble the SM distribution; for $a_L > a_T$,

[3]In the Higgs rest frame, only HV_LV_L and HV_TV_T, where V denotes either W or Z bosons, are kinematically allowed.

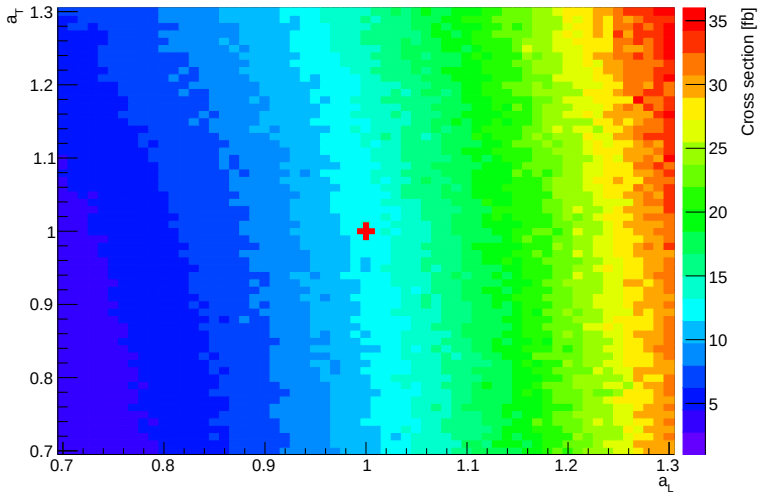

Figure 4.11: The effect of (a_L, a_T) coupling modifications on $\sigma_{\text{VBF}} \cdot \mathcal{B}_{H\to WW}$ before analysis selection cuts. Red cross in (a) corresponds to the SM point (with $a_L = a_T = 1$).

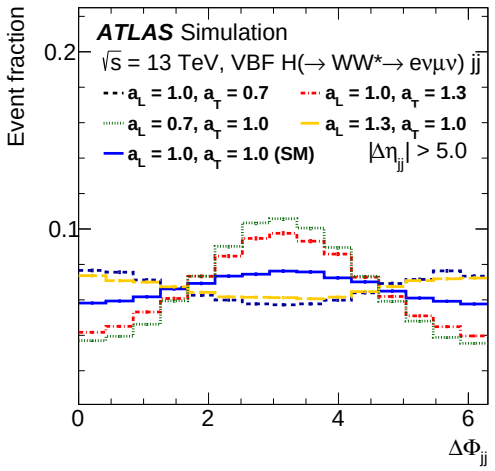

Figure 4.12: $\Delta\Phi_{jj}$ for selected couplings combinations.

the jets tend to be more collinear in the transverse plane; in cases where

$a_L < a_T$ back-to-back geometries are favoured.

The insight into the Higgs boson decay vertex can be provided by observables related to correlations between final state charged leptons, such as m_{ll} and $\Delta\phi_{ll}$. Due to ambiguities in reconstructing the Higgs boson rest frame from the final state particles including two neutrinos, these variables demonstrate much worse discriminating power for the BSM scenarios. The distributions probed in Ref. [20], such as the azimuthal angle between leptons, $\Delta\phi_{ll}$, and observables related to the transverse momenta of the forward jets, were instead used in the construction of the BDT distinguishing the properties of the SM signal from backgrounds.

4.10.3 Moment morphing

BSM signals with arbitrarily chosen (a_L, a_T) coupling combinations are obtained using histogram morphing presented in Refs. [108, 109]. In this way, the distributions corresponding to relevant (continuous) coupling combinations can be obtained from a small set of generated benchmarks. Morphing is a procedure of linear interpolation or extrapolation that takes into account both event yields and kinematical properties of the benchmark samples. An implementation of morphing has been developed within the `RooFit` package [110], making use of `HistFactory` [111]. The provided signal model is implemented in the `RooLagrangianMorphing` class in RooFit. The described analysis is one of the first applications of the morphing method in high energy physics data analysis.

An advantage of moment morphing is that analytical properties of the lagrangian are taken into account by weighting all input distributions based on the matrix element of the process they describe. Unlike the the matrix element reweighting procedure (which is a standard technique in high energy phycics), that requires a single input sample, morphing requires several input samples, depending on the number and types of BSM couplings. The beneficial property of morphing is its capability of morphing entire distributions of observables rather than providing a translation on an event-by-event basis.

In the following, the construction of a morphed distribution is outlined in the example of Higgs-related processes, at the leading order in QCD and electroweak couplings. This rather technical introduction is followed by the application of signal morphing in the polarisation measurement.

Morphing describes the dependence of a given physical observable $T(\vec{g}_{\text{target}})$ on a BSM signal. This signal is assumed to have an effect of modified scalar

couplings $\vec{g}_{\text{target}} \equiv \{g_{SM,1}, \cdots, g_{SM,m}, g_{BSM,1}, \cdots, g_{BSM,n}\}$, without modifications to the particles content of the SM. In general, the observable T depends on m SM and n BSM couplings. This dependence is described by a morphing function

$$T(\vec{g}_{\text{target}}) = \sum_i w_i(\vec{g}_{\text{target}}; \vec{g}_i) T_{\text{in}}(\vec{g}_i), \tag{4.11}$$

which is a linear combination of the values or observables T_{in} at a number of discrete coupling configurations $\vec{g}_i = \{\tilde{g}_{SM,1}, \cdots, \tilde{g}_{SM,m}, \tilde{g}_{BSM,1}, \cdots, \tilde{g}_{BSM,n}\}$. The input distributions T_{in} are obtained from the Monte Carlo (MC) simulation of the signal process for a given coupling configuration $\vec{g}_i$.

Morphing relies on a narrow width approximation for (in this case) the Higgs resonance. Therefore, at lowest order observables T are second orders polynomial in coupling parameters affecting both Higgs production and decay.

The contribution of each simulated T_{in} is weighted by w_i based on the assumption that the value of a physical observable is proportional to the squared matrix element for the studied process

$$T \propto |\mathcal{M}|^2 = \underbrace{\left(\sum_{x \in p,s} g_x \mathcal{O}(g_x)\right)^2}_{\text{production}} \cdot \underbrace{\left(\sum_{x \in d,s} g_x \mathcal{O}(g_x)\right)^2}_{\text{decay}}. \tag{4.12}$$

In the above, operators appearing only in the production vertex are labeled with p, operators only appearing in the decay vertex with d, and operators shared between both vertices with s. A visual representation of the idea for a one-dimensional case is shown in Figure 4.13. Here, histograms labeled "SM", "BSM" and "Mix" are simulated T_{in} histograms, and the red histogram is a result of morphing at a chosen (continuous) parameter configuration.

The number N of input base samples required to construct the morphing function of eq. (4.11) depends on how many coupling parameters enter the only production (n_p), only the decay vertex (n_d), and are shared in production and decay (n_s):

$$N = \frac{n_p\,(n_p+1)}{2} \cdot \frac{n_d\,(n_d+1)}{2} + \binom{4+n_s-1}{4}. \tag{4.13}$$

In eq. (4.13) large parenthesis denote the combination formula: $\binom{n}{k} \equiv \frac{n!}{(n-k)!k!}$.

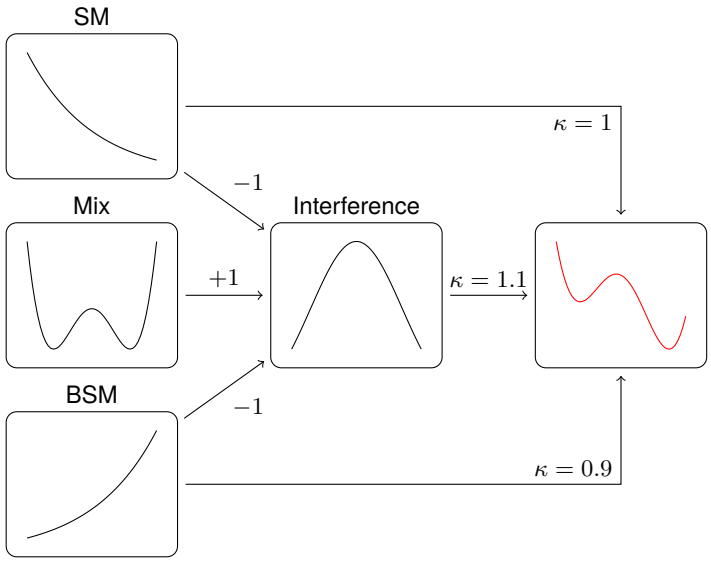

Figure 4.13: Illustration of the morphing procedure in a one-dimentional showcase.

In case of the VBF Higgs boson production with subsequent decay into vector bosons, modified with respect to the SM by a set of two couplings $\{a_L, a_T\}$, affecting both the production and the decay vertex, $n_p = 0$ and $n_d = 0$ and $n_s = 2$. The number of input samples given by equation 4.13 is 5. The morphed distribution is $\Delta\Phi_{jj}$ distribution in all four BDT bins in the signal region, as discussed in section 4.10.2.

In order to estimate uncertainties related to the morphing method, the following tests have been performed. The expected $\Delta\Phi_{jj}$ distribution resulting the morphing method in all four BDT bins in the signal region has been compared with the same distribution obtained directly from the Matrix Element generator. Additionally, the morphing performance has been validated by changing the combination of the input samples used in the construction of the morphing function. As a result, the normalisation uncertainties of morphed distributions are found to be negligible (lower than 1%). Shape differences between morphed and simulated distributions have been added as a shape uncertainty on the signal sample in the likelihood fit.

4.10.4 Results

Fits are performed simultaneously in both the SR and CRs, largely following the methodology of cross-section measurement described earlier. The difference lies in using the distribution of the signed $\Delta\Phi_{jj}$ observable in each BDT bin in addition to event counts in this bin. In control regions only total event yields are used in the fit.

Several types of likelihood scans are performed to constrain either a single parameter of interest or both of them simultaneously. Each type of fit is performed in both parametrisations: $(a_{\mathrm{L}}, a_{\mathrm{T}})$ and $(\kappa_{VV}, \varepsilon_{VV})$. In one-dimensional fits over a single parameter of interest (POI), with the other one being fixed to its SM value the following information was exploited in the fits:

- the dependence of the input distribution's shape on the selected parameter of interest, or
- information on both shape of selected distribution and total event rates.

Setting κ_{VV} to 0 is equivalent to $a_L = 0$, while $\epsilon_{VV} = 0$ imposes $a_L = a_T$. In the other variant of fits the other parameter is profiled. This means that the profiled parameter is fixed to its unconditional maximum likelihood value for each value of the POI. Then, the POI is fixed to its conditional maximum likelihood value. By construction, in this second ensemble of fits both parameters may vary independently and are therefore probed in a model-independent way.

The post-fit event yields in the signal and the control regions are presented in Table 4.10 together with the number of events measured in data. The uncertainties quoted in Table 4.10 include those from theoretical and experimental systematic sources and those due to sample statistics. The presented numbers were taken from the fit to ϵ_{VV}, but are consistent within statistical errors with these from fits to κ_{VV}, a_L and a_T. Small differences (within errors) with respect to cross-section measurement originate from two factors. Firstly, the signal samples are simulated with independent MC generators which lead to small event counts in the phase space considered. Secondly, the cross-section measurement corresponds to a fit to κ_{VV} with ϵ_{VV} fixed to 0.

Figure 4.14 depicts the weighted $\Delta\Phi_{jj}$ distribution in all four BDT bins of the VBF signal region (upper panel). Events are weighted by a significance

of the BDT bin they were categorised to. Each bin significance was evaluated taking into account the number events classified as originating from either signal or backgrounds, N_S and N_B, respectively and expressed as $\ln(1 + N_S/N_B)$. The lower panel presents the ratio between data and MC predictions within uncertainties.

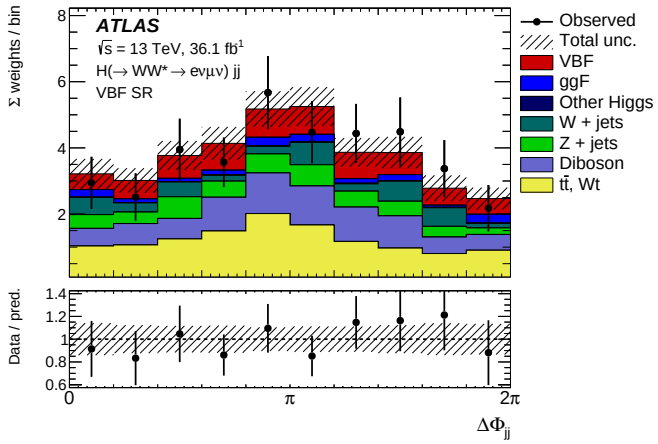

Figure 4.14: The weighted $\Delta\Phi_{jj}$ distribution in the VBF signal region, with signal and background yields fixed from the fit for ε_{VV} using shape and rate information. Data-to-simulation ratios are shown at the bottom of the plot. The shaded areas depict the total uncertainty.

Table 4.10: Post-fit event yields in the signal and control regions obtained from a scan over ε_{VV} exploiting both shape and rate information. The fit constrains the total expected yields to the observed yields.

Process	Top CR	$Z \to \tau\tau$ CR	SR
VBF	3.2 ± 2.2	2.6 ± 1.8	34 ± 22
ggF	3.9 ± 1.7	2.4 ± 1.0	28 ± 12
Other Higgs	1.5 ± 0.7	6.2 ± 3.1	6.0 ± 3.0
$t\bar{t}$, Wt	7400 ± 100	53 ± 7	1220 ± 100
WW	51 ± 6	21.8 ± 2.9	360 ± 70
Z + jets	54 ± 10	370 ± 24	320 ± 70
W + jets	190 ± 40	23.0 ± 2.4	115 ± 27
Non-WW dibosons	14.3 ± 1.8	20.8 ± 3.3	83 ± 11
Observed	7668	501	2164

In the following, the results of fits will be presented in both parametrisations. The central values and uncertaities of the fit will be accommpanied by plots of maximal log likelihood scans (LLH). Leading uncertainties will be listed in selected cases, because they are similar among the fits.

(a_L, a_T) parametrisation

The results of the likelihood scans are given in Figure 4.15. The scan over a_{L} (a_{T}) is shown in the upper (lower) panel. Blue lines represent fits to signal simulation (expected), while red lines the fit to data (observed). The LLH curves shown in Figures 4.15(b) and 4.15(c) are the results of the fit in which both the shape and normalisation of the signal are taken into account, while the LLH curves in Figure 4.15(a) are obtained using only the shape information. The asymmetry of the curves results from the asymmetric behaviour of the cross section with respect to the changes in the parameter values (see Ref. [20]). The largest sensitivity to a_{L} stems from the rate information and this parameter cannot be constrained using the shape information alone. The sensitivity to a_{T}, on the other hand, comes predominantly from the shape information, as the likelihood ratio increases only slightly when adding the normalisation information. The resulting best-fit values and their uncertainties computed at 68% CL are presented in Table 4.11. Measurement of a_{L} features smaller overall uncertainties than the fit to a_{T}. Fits, in which values of the other parameter are fixed are consistent with fits allowing the other parameter to vary (profiling). All measurements are consistent with the SM expectations.

The dominant sources of uncertainty for fits involving both shape and rate information, are listed in Table 4.12. Individual sources of uncertainties as well as their groups are shown. The dominant ones are related to the limited data yields (data statistic) and to the quality of modeling the dominant top-quark and WW backgrounds. Statistical uncertainties are more pronounced in the fits to a_T, because shape information is more important in constraining this parameter. Dominant experimental uncertainties are related to pile-up and jet energy scale and resolution.

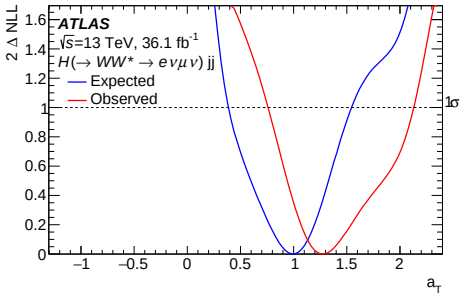

(a) a_{T} shape-only fit with $a_{\mathrm{L}} = 1$

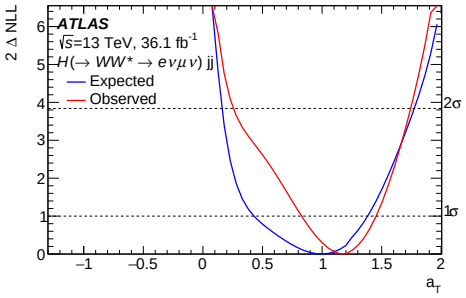

(b) a_{T} shape+rate fit with $a_{\mathrm{L}} = 1$

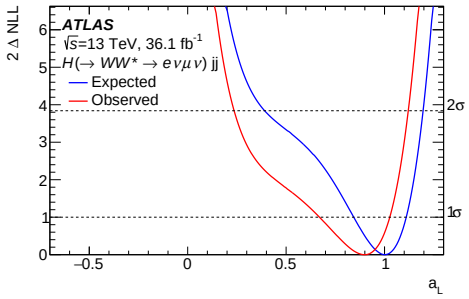

(c) a_{L} shape+rate fit with $a_{\mathrm{T}} = 1$

Figure 4.15: Likelihood scans over the transversely (a, b) and longitudinally (c) polarised couplings. Fits using shape-only (a) and shape+rate (b, c) information are shown. All relevant experimental and modeling systematic uncertainties are considered in the fits.

Table 4.11: Best-fit values and their uncertainties as obtained from the shape-only and shape-plus-rate likelihood fits to the Asimov dataset and to ATLAS data. Results of both the shape-only and shape+rate fits for a_{L} and a_{T} are shown. Results of fits to one parameter with the other one fixed or profiled are presented.

Type	Expected	Observed
a_{T} shape-only fit ($a_{\mathrm{L}} = 1$)	$1.0 \pm 0.5(\mathrm{stat.})^{+0.3}_{-0.4}(\mathrm{syst.})$	$1.3^{+0.8}_{-0.4}(\mathrm{stat.})^{+0.3}_{-0.2}(\mathrm{syst.})$
a_{L} shape + rate fit ($a_{\mathrm{T}} = 1$)	$1.00^{+0.08}_{-0.10}(\mathrm{stat.})^{+0.07}_{-0.13}(\mathrm{syst.})$	$0.90^{+0.09}_{-0.13}(\mathrm{stat.})^{+0.08}_{-0.18}(\mathrm{syst.})$
a_{T} shape + rate fit ($a_{\mathrm{L}} = 1$)	$1.00^{+0.36}_{-0.49}(\mathrm{stat.})^{+0.19}_{-0.27}(\mathrm{syst.})$	$1.19^{+0.27}_{-0.32}(\mathrm{stat.})^{+0.12}_{-0.14}(\mathrm{syst.})$
a_{L} shape + rate fit (a_{T} profiled)	$1.00^{+0.08}_{-0.10}(\mathrm{stat.})^{+0.08}_{-0.13}(\mathrm{syst.})$	$0.91^{+0.10}_{-0.18}(\mathrm{stat.})^{+0.09}_{-0.17}(\mathrm{syst.})$
a_{T} shape + rate fit (a_{L} profiled)	$1.0^{+0.4}_{-0.5}(\mathrm{stat.})^{+0.2}_{-0.4}(\mathrm{syst.})$	$1.2 \pm 0.4(\mathrm{stat.})^{+0.2}_{-0.3}(\mathrm{syst.})$

Table 4.12: The contributions of the leading individual systematic uncertainties together with the data statistical uncertainties, in the one-dimensional fit for a_L (a) and a_T (b) for electroweak-boson polarisation in the VBF $H \to WW$ channel. Both the shape and rate information is exploited in the fit. The theoretical and experimental uncertainties are subdivided further into categories.

(a) a_L fit, $a_T = 1$

Source	Δa_L
Total data statistical uncertainty	0.11
SR data statistical uncertainty	0.11
CR data statistical uncertainty	0.018
MC statistical uncertainty	0.037
Total systematic uncertainty	0.13
Theoretical uncertainty	0.10
Top-quark bkg.	0.072
WW bkg.	0.061
ggF bkg.	0.035
Z/γ^* bkg.	0.018
VBF signal	0.019
Experimental uncertainty	0.054
Modeling of pile-up	0.040
Jet	0.026
b-tagging	0.014
Luminosity	0.010
Total	0.18

(b) a_T fit, $a_L = 1$

Source	Δa_T
Total data statistical uncertainty	0.29
SR data statistical uncertainty	0.29
CR data statistical uncertainty	0.013
MC statistical uncertainty	0.037
Total systematic uncertainty	0.13
Theoretical uncertainty	0.10
Top-quark bkg.	0.076
WW bkg.	0.072
ggF bkg.	0.026
Z/γ^* bkg.	0.022
VBF signal	0.022
Experimental uncertainty	0.044
Modeling of pile-up	0.042
Jet	0.032
Misidentified leptons	0.010
b-tagging	0.002
Total	0.33

$(\kappa_{VV}, \varepsilon_{VV})$ parametrisation

The results of the LLH scans in the parametrisation using pseudo-observables are shown in Figure 4.16. This time the plots illustrate fits, in which the other parameter was profiled. Blue lines represent fits to signal simulation (expected), while red lines the fit to data (observed). Central values of the fits are shown in Table 4.13. They are consistent with the results obtained in (a_L, a_T) parametrisation. The breakdown of uncertainties is presented in Table 4.14.

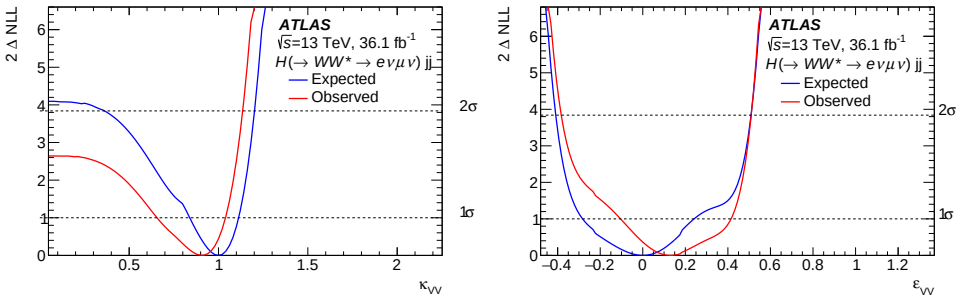

(a) (b)

Figure 4.16: Likelihood scans of shape+rate fits over (a) κ_{VV} and (b) ε_{VV}, with the other parameter profiled. Blue lines represent fits to signal simulation (expected), while red lines the fit to data (observed). All relevant experimental and theoretical systematic uncertainties are considered in the fits.

Table 4.13: Best-fit values and their uncertainties as obtained from the shape-only and shape-plus-rate likelihood fits to the Asimov dataset and to ATLAS data. Results of both shape-only and shape+rate fits for ε_{VV} and κ_{VV} are shown. Results of fits to one parameter with the other one fixed or profiled are presented.

Type	Expected	Observed
ε_{VV} shape-only fit ($\kappa_{VV} = 1$)	$0.00^{+0.23}_{-0.25}(\text{stat.})^{+0.14}_{-0.17}(\text{syst.})$	$0.14^{+0.39}_{-0.22}(\text{stat.})^{+0.16}_{-0.12}(\text{syst.})$
κ_{VV} shape + rate fit ($\varepsilon_{VV} = 0$)	$1.00^{+0.08}_{-0.10}(\text{stat.})^{+0.08}_{-0.13}(\text{syst.})$	$0.91^{+0.09}_{-0.12}(\text{stat.})^{+0.09}_{-0.18}(\text{syst.})$
ε_{VV} shape + rate fit ($\kappa_{VV} = 1$)	$0.00^{+0.18}_{-0.24}(\text{stat.})^{+0.08}_{-0.13}(\text{syst.})$	$0.09^{+0.13}_{-0.16}(\text{stat.})^{+0.06}_{-0.07}(\text{syst.})$
κ_{VV} shape + rate fit (ε_{VV} profiled)	$1.00^{+0.08}_{-0.10}(\text{stat.})^{+0.08}_{-0.13}(\text{syst.})$	$0.91^{+0.10}_{-0.18}(\text{stat.})^{+0.09}_{-0.17}(\text{syst.})$
ε_{VV} shape + rate fit (κ_{VV} profiled)	$0.00^{+0.22}_{-0.24}(\text{stat.})^{+0.11}_{-0.15}(\text{syst.})$	$0.13^{+0.28}_{-0.20}(\text{stat.})^{+0.08}_{-0.10}(\text{syst.})$

Table 4.14: The contributions of the leading individual systematic uncertainties together with the data statistical uncertainties, in the one-dimensional fit for the pseudo-observables κ_{VV} (a) and ε_{VV} (b) for electroweak-boson polarisation in the VBF $H \to WW$ channel. Both the shape and rate information is exploited in the fit. The theoretical and experimental uncertainties are subdivided further into categories.

(a) κ_{VV} fit, $\varepsilon_{VV} = 0$

Source	$\Delta\kappa_{VV}$
Total data statistical uncertainty	0.11
SR data statistical uncertainty	0.10
CR data statistical uncertainty	0.019
MC statistical uncertainty	0.035
Total systematic uncertainty	0.12
Theoretical uncertainty	0.10
Top-quark bkg.	0.072
WW bkg.	0.062
ggF bkg.	0.033
Z/γ^* bkg.	0.017
VBF signal	0.019
Experimental uncertainty	0.050
Jet	0.026
b-tagging	0.014
Luminosity	0.011
Misidentified leptons	0.007
Total	0.17

(b) ε_{VV} fit, $\kappa_{VV} = 1$

Source	$\Delta\varepsilon_{VV}$
Total data statistical uncertainty	0.14
SR data statistical uncertainty	0.14
CR data statistical uncertainty	0.011
MC statistical uncertainty	0.036
Total systematic uncertainty	0.056
Theoretical uncertainty	0.050
Top-quark bkg.	0.039
WW bkg.	0.036
ggF bkg.	0.013
Z/γ^* bkg.	0.012
VBF signal	0.010
Experimental uncertainty	0.024
Modeling of pile-up	0.022
Jet	0.018
Misidentified leptons	0.010
b-tagging	0.010
Total	0.16

4.11 Summary

Using the fully leptonic Higgs boson decays to WW^*, the measurements of inclusive cross-section of Higgs boson production via the gluon–gluon fusion (ggF) and vector-boson fusion (VBF) were performed. The cross-sections times the $H \to WW^*$ branching ratio are measured to be $11.4^{+1.2}_{-1.1}$ (stat.)$^{+1.8}_{1.7}$ (syst.) pb in the ggF production channel and $0.50^{+0.24}_{-0.22}$(stat.) ± 0.17(syst.) pb, in the VBF. The largest sources of uncertainties stem from theoretical modeling of the WW background and (in the VBF cross-section measurement) the modeling of ggF signal in the measured VBF-dominated phase space region. Both measurements, though the VBF to a larger extent, are affected by the statistical uncertainty of the Monte Carlo simulation.

Using the VBF signal selection, hints of BSM physics are searched for by means of detecting anomalies in the Higgs boson coupling-strength form factors to longitudinally and transversely polarised W and Z bosons. It is the first such measurement of the bosonic polarisation-dependent Higgs couplings. To distinguish various BSM signals from the SM, the distribution of azimuthal angle between forward jets in the plane perpendicular to the beam axis, $\Delta\Phi_{jj}$, is utilised together with the information on event yields. The couplings are parametrised in two different ways and results of both parametrisations are extracted. Each measurement is performed in two settings: one-dimensional (where it was assumed that the other parameter is equal to its SM value) and two-dimensional, where the other parameter is profiled.

In the first type of fits the shape of $\Delta\Phi_{jj}$ alone is sufficient to constrain the coupling to transversely polarised bosons, a_{T}, while to constrain a_{L} the additional information about event rates is necessary. Profiling the other coupling-strength scale factor results in measured values: $a_{\mathrm{L}} = 0.91^{+0.10}_{-0.18}$(stat.) $^{+0.09}_{-0.17}$(syst.) and $a_{\mathrm{T}} = 1.2 \pm 0.4$(stat.) $^{+0.2}_{-0.3}$(syst.), while $a_{\mathrm{L}} = 1.00^{+0.08}_{-0.10}$(stat.) $^{+0.08}_{-0.13}$(syst.) and $a_{\mathrm{T}} = 1.0^{+0.4}_{-0.5}$(stat.) $^{+0.2}_{-0.4}$(syst.) are expected in the SM. With an approximate mapping to pseudo-observables κ_{VV} and ϵ_{VV} the following constraints are obtained in two-dimensional fits: $\kappa_{VV} = 0.91^{+0.10}_{-0.18}$(stat.)$^{+0.09}_{-0.17}$(syst.) and $\epsilon_{VV} = 0.13^{+0.28}_{-0.20}$ (stat.)$^{+0.08}_{-0.10}$(syst.), while $\kappa_{VV} = 1.00^{+0.08}_{-0.10}$(stat.)$^{+0.08}_{-0.13}$(syst.) and $\epsilon_{VV} = 0.00^{+0.22}_{-0.24}$ (stat.)$^{+0.11}_{-0.15}$(syst.) are expected. In this parameterisation the sensitivity to the on-shell coupling κ_{VV} stems predominantly from the event yields, while the off-shell coupling ε_{VV} is extracted using both shape and rate information. These measurements are statistically limited, which

means that statistical uncertainties of the signal are larger than any single source of systematical uncertainty.

All these measurements are consistent with the expectations for the SM Higgs boson.

5 Higgs boson self-coupling

The Brout-Englert-Higgs mechanism [13, 15], presented in Chapter 2, is responsible for generating non-zero masses of electroweak vector bosons. In this chapter I focus on another consequence of the Higgs mechanism, namely the Higgs boson self-interactions.

After spontaneous symmetry breaking, and gauge fixing, the Higgs field is a real scalar field $\phi = (v + h^0)/\sqrt{2}$, where h^0 is the (real) excitation from its vacuum expectation value (v, VEV). The Higgs boson acquires mass $m_h^2 = -2\mu^2 = 2\lambda v^2$ and its potential has a form:

$$\begin{aligned} V(h^0) &= 2\lambda v^2 \frac{(h^0)^2}{2} + 6\lambda v \frac{(h^0)^3}{3!} + 6\lambda \frac{(h^0)^4}{4!} - \frac{v^4\lambda}{4} \\ &\equiv m_h^2 \frac{(h^0)^2}{2} + \lambda_{3h} \frac{(h^0)^3}{3!} + \lambda_{4h} \frac{(h^0)^4}{4!} - \frac{v^4\lambda}{4}. \end{aligned} \tag{5.1}$$

As can be explicitly read out from the second line of eq. (5.1), after spontaneous symmetry breaking, the Higgs boson acquires cubic and quartic self-interactions, whose triple and quartic couplings read:

$$\lambda_{3h} = \frac{3m_h^2}{v}, \quad \lambda_{4h} = \frac{3m_h^2}{v^2}. \tag{5.2}$$

Both λ_{3h} and λ_{4h} are parametrised with the Higgs mass and its vacuum expectation value v. They are thus not independent parameters in the SM, but closely related with each other. Higg self-interactions enable the measurement of global properties of the Higgs boson potential, thus providing a valuable consistency check of the Higgs mechanism.

In this chapter, I focus on measuring λ_{3h}. At the LHC a direct way of accessing this parameter is by observing a production of Higgs boson pairs.

Higgs pair production at proton-proton colliders occurs predominantly through gluon fusion (ggF) process. The calculation of the cross-section for

Table 5.1: Dominant cross sections for SM Higgs pair production at the LHC at $\sqrt{s} = 14$ TeV.

Process	Cross-section [fb]	Scale μ_R	Perturbative order
ggF	$16.5^{+4.6}_{-3.5}$	M_{hh}	LO [112–114]
	$32.91^{+13.6\%}_{-12.6\%}$	$M_{hh}/2$	NNLO [115]
VBF	$2.01^{+0.03}_{-0.02}$	Q_{V^*}	NLO [116]
$hhjj$	$1.94^{+0.023}_{-0.026}$	$M_{hh}/2$	NLO [2]
$hhtt$	$0.949^{+0.017}_{-0.045}$	$M_{hh}/2$	NNLO [2]
Z^0hh	$0.415^{+0.035}_{-0.027}$	M_{hhZ}	NNLO [2]
W^+hh	$0.369^{+0.033}_{-0.039}$	M_{hhW}	NNLO [2]
W^-hh	$0.198^{+0.012}_{-0.013}$	M_{hhW}	NNLO [2]

this process is an extremely complicated task. It took about thirty years from calculating leading order (LO) in QCD predictions to obtaining next-to-next-to-leading (NNLO) order with resummed next-to-next-to-leading-logarithmic (NNLL) result. This chapter outlines the efforts that led to its most accurate computation to date as well as a journey of creative endeavours aiming at improving approximated computations. Inefficiencies of previous results will also be outlined as well as complications related to estimating complete theoretical uncertainties.

As shown, based on leading-order calculations, in Section 5.2, sensitivity of the Higgs pair production cross-section at the LHC to its self-coupling is small. Therefore, finding phase space regions where the contribution of Higgs self-coupling to Higgs pair production is enhanced is crucial for future measurements. En example construction of such optimisation is given in Section 5.3.3.

This chapter is based upon the publications [1, 2], that I co-authored.

5.1 Cross-sections

Fixed order Higgs pair production cross-sections for 14 TeV proton-proton collisions are listed in Table 5.1. Results of the highest available perturbative

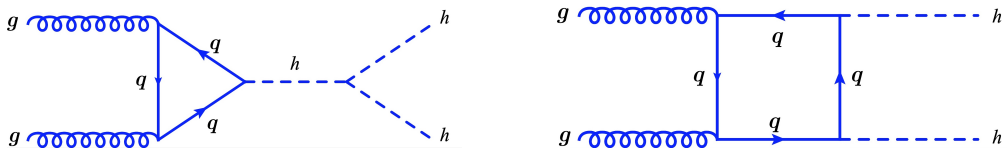

Figure 5.1: Feynman diagrams contributing to the leading order amplitude for SM Higgs pair production in gluon-gluon fusion: the "triangle" diagram (left) and the "box" diagram (right).

order in QCD are shown for all channels. In case of gluon fusion additionally the leading order (LO) is given. These cross-sections were performed at renormalisation scales μ_R indicated in the third column, which are specific to a given process. They are related to the invariant mass of produced Higgs pairs, or triplets: hhW and hhZ. In case of the VBF, Q_{V^*} denotes the momentum transfer of the exchanged off-shell weak boson. Among processes contributing to events with two Higgs bosons in the final state the largest cross-sections have: the production through gluon fusion (ggF) with $\sigma_{ggF} \sim$ 33 fb, vector boson fusion, $\sigma_{VBF} \sim 2$ fb, and associated production with: a pair of light flavour jets ($\sigma_{hhjj} \sim 2$ fb), top– anti-top quark pair ($\sigma_{tthh} \sim$ 1 fb) a Z^0 boson ($\sigma_{Zhh} \sim 0.4$ fb), W^+ ($\sigma_{W^+hh} \sim 0.4$ fb) and associated production with a W^- ($\sigma_{W^-hh} \sim 0.2$ fb). The production cross sections for the Higgs pairs are thus at least a factor of 10^3 smaller than for the single Higgs boson. Higgs pair production through gluon-gluon fusion is by a factor of about 20 larger than second-largest vector boson fusion. Quoted errors reflect the uncertainties related to varying renormalisation scale μ_R in the range $[\mu_R/2, 2\mu_R]$. The production cross-section of triple Higgs bosons at the LHC, for a comparison, amounts to ∼80 ab at 14 TeV [117]. This process is therefore beyond measurement capabilities of the LHC and will not be discussed here.

The dominant Higgs pair production channel at the LHC, is gluon fusion. The leading order cross-section for this process was computed already in the 1980s [112, 114]. The corresponding Feynman diagrams are shown in Fig. 5.1. They feature massive quark loops, with the dominant contribution from the heaviest of them, the top quark. First attempts to compute higher order corrections were performed in the Higgs Effective Field Theory (HEFT) [118–120]. This approximation takes the limit of the top quark mass becoming infinitely large, which simplifies calculations of loop diagrams. Consequently, the top-quark loops are not resolved but treated as

Table 5.2: Predicted Higgs pair production cross section via gluon fusion for different LHC centre-of-mass energies and $m_h = 125$ GeV.

LHC Energy (TeV)	Cross-section [fb]	scale unc. [%]	PDF unc. [%]	α_S unc. [%]
7	7.078	$^{+4.0}_{-5.7}$	$\pm$ 3.4	$\pm$ 2.8
8	10.16	$^{+4.1}_{-5.7}$	$\pm$ 3.1	$\pm$ 2.6
13	33.53	$^{+4.3}_{-6.0}$	$\pm$ 2.1	$\pm$ 2.3
14	39.64	$^{+4.4}_{-6.0}$	$\pm$ 2.1	$\pm$ 2.2

multiplicative form factors for the higher order QCD corrections. The result of HEFT-based NLO calculations presented in Ref [114] revealed that the (approximate) NLO cross-section was about twice as large as the LO result. In other words, NLO approximate K-factors were equal to about two. Such a large value indicates large theoretical uncertainty of the LO cross-section calculation. A complete NLO cross-section was computed only in 2016 in Refs [115, 121, 122]. Its value confirms the overall large NLO K-factors and differs by about 15% from the HEFT approximation. Between this NLO result and NNLO corrections computed using HEFT beyond NLO, there is another $\sim$20% increase in the rates. The threshold resummation corrections for Higgs boson pair production at NNLL [123, 124] further increase the cross-section.

The results of this last technique, $\sigma^{NNLO+NNLL}_{ggF\to hh}$ are given in Table 5.2 for different centre-of-mass energies at the LHC. The numbers are based on NNLL matched to NNLO calculations including top quark mass effects to NLO [2]. The mass of the Higgs boson asummed in the cross-section calculations is m_h =125 GeV, the numerical variations of the cross-section when using the measured Higgs boson mass is negligible. The cross-sections at 7 and 8 TeV centre-of-mass energies of colliding protons are comparable. There is a noticeable growth of a factor of three from 8 to 13 TeV and of a factor of four between 8 and 14 TeV. The theoretical uncertainties of this calculation are split into effects related to the choice of renormalisation scale, parton distribution functions, running strong coupling constant α_S and the mass of the top quark. Scale uncertainties are estimated by varying renormalisation scale up and down by a factor of two with respect to the central scale $\mu_R = M_{hh}/2$.

PDF and running α_S uncertainties are evaluated using the PDF4LHC recommendation [2] and are based on the PDF4LHC15_nnlo_mc set of parton distribution functions. Top mass uncertainty from unknown top quark mass effects at NNLO is arbitrarily assumed at $\pm 5\%$.

Searches in the early data of the LHC and first feasibility studies for the High Luminosity LHC, presented in Chapters 6–8, consider only the gluon fusion production channel. In each following chapter, the assumed value of Higgs pair production cross-section is stated explicitly, because the best computations available at the time of each analysis slightly differed from results in Table 5.2.

5.2 Higgs pair production through gluon fusion at the Leading Order

All Higgs pair production channels listed in Table 5.1 include both types of Feynman diagrams: these featuring the Higgs boson self-coupling and others, in which two Higgses are produced separately. To obtain the gauge invariant di-Higgs cross-section, squares of both diagrams and their interference need to be evaluated. In case of diagrams for the amplitude of ggF, presented in Fig.5.1, only the "triangle" diagram contains the trilinear Higgs coupling, while the "box" one does not.

In the previous section, the numerical differences in computing Higgs pair cross-sections in the exact way and using HEFT were highlighted. In this section, the origin of these differences will be demonstrated at the LO in QCD using analytical formulae. Exact and approximate leading order matrix elements are evaluated to understand both total cross-sections and kinematical properties of the two predictions. This section follows the analytical comparison between exact and HEFT matrix elements for a light Higgs boson ($m_h = 125$ GeV $\ll 1$ TeV) performed in Ref [1, 112, 114].

The analytical expression for the partonic cross-section is given by:

$$\hat{\sigma}^{(LO)}_{gg\to hh} = \int d\hat{t}\, \frac{\alpha^2 \alpha_S^2}{2^{15}\pi M_W^4} \left(|C_\triangle F_\triangle + C_\square F_\square|^2 + |C_\square G_\square|^2 \right), \tag{5.3}$$

where the terms denoted as "$\triangle$" and "$\square$" correspond to the individual contributions from the diagrams in Fig. 5.1. Functions $F_\triangle$, $F_\square$ and $G_\square$ contain all dependence on fermionic masses in the loops, whereas the coefficients $C_\triangle$

and $C_\square$ express the resonance behaviour of the Higgs propagators. The scale in α_S has been set to the invariant mass of the two incoming partons, $\sqrt{\hat{s}}$. The Mandelstam variable $\hat{t}$ is defined as:

$$\hat{t} = -\frac{1}{2}\left[\hat{s} - 2m_h^2 - \hat{s}\sqrt{1 - \frac{4m_h^2}{\hat{s}}}\cos\theta,\right], \tag{5.4}$$

where θ is the angle between the two final state Higgs bosons in the centre of mass frame. The term $G_\square$ is non-negligible only in the limit of large transverse momentum of the Higgs boson [112] and will therefore be omitted in the following. The term in the matrix element squared (MES) reduces to

$$|C_\triangle F_\triangle + C_\square F_\square|^2. \tag{5.5}$$

The coefficients C are equal to:

$$C_\triangle = \frac{\lambda_{3h} v}{\hat{s} - m_h^2},\ C_\square = 1. \tag{5.6}$$

$C_\triangle$ contains the Higgs boson self-coupling $\lambda_{3h} = \frac{3m_h^2}{v}$. Computing MES requires the calculation of the form factors $F_\triangle$ and $F_\square$ stemming from the triangle and box loops. They can be calculated either exactly or by applying HEFT approximation, e.g. the limit where the top quark mass becomes infinite.

The exact formula for $F_\triangle$ in eq. (5.5) is given by [112] and [113]:

$$F_\triangle = 2\frac{m_q^2}{\hat{s}}\left[2 + \left(4 - \frac{\hat{s}}{m_q^2}\right) m_q^2 C_{ab}\right] = \tau_q[1 + (1 - \tau_q) f(\tau_q)], \tag{5.7}$$

where $\tau_q = \frac{4m_q^2}{\hat{s}}$ and m_q is the mass of the fermion in the loop. In the above computations only the top quark is considered as the contribution from bottom and lighter quarks is negligible, so that τ_q represents a single contribution with $m_q = m_t$. The function $f(\tau_q)$ stems from the scalar integral, in which $C_{ab} = -\frac{2}{\hat{s}} f(\tau_q)$ with

$$f(\tau_q) = \begin{cases} \arcsin^2\left(\frac{1}{\sqrt{\tau_q}}\right) & \tau_q \geq 1, \\ -\frac{1}{4}\left[\log\frac{1+\sqrt{1-\tau_q}}{1-\sqrt{1-\tau_q}} - i\pi\right]^2 & \tau_q < 1. \end{cases} \tag{5.8}$$

$F_\Box$ is given by:

$$\begin{aligned} F_\Box = -4m_q^2\big[&m_q^2(8m_q^2-\hat{s}-m_h^2)(D(p_1,p_2,p_3)+D(p_2,p_1,p_3)+D(p_1,p_3,p_2)) \\ &+\frac{\hat{u}\hat{t}-m_h^4}{\hat{s}}(4m_q^2-m_h^2)D(p_1,p_3,p_2)+2+4m_q^2C(p_1,p_2) \\ &+\frac{2}{\hat{s}}(m_h^2-4m_q^2)[(\hat{t}-m_h^2)C(p_1,p_3)+(\hat{u}-m_h^2)C(p_2,p_3)]\big], \end{aligned} \tag{5.9}$$

where p_1 and p_2 denote the momenta of gluons, p_3 is the momentum of one of the Higgs bosons, C's and D's are the three- and four point functions, respectively, defined as usually:

$$C(p_1,p_2)=\int\frac{dq^4}{i\pi^2}\frac{1}{(q^2-m_q^2)((q+p_1)^2-m_q^2)((q+p_1+p_2)^2-m_q^2)} \tag{5.10}$$

and

$$D(p_1,p_2,p_3)= \int\frac{dq^4}{i\pi^2}\frac{1}{(q^2-m_q^2)((q+p_1)^2-m_q^2)((q+p_1+p_2)^2-m_q^2)((q+p_1+p_2+p_3)^2-m_q^2)} \tag{5.11}$$

After series expansion of the first term in eq. (5.8), $f(\tau_q)$ can be written as

$$f(\tau_q)=\frac{1}{\tau_q}+\frac{1}{3\tau_q^2}+\mathcal{O}\left(\left(\frac{\hat{s}}{4m_q^2}\right)^3\right). \tag{5.12}$$

In the infinite top mass approximation, $\tau_q\to+\infty$ and $F_\triangle$ becomes

$$F_\triangle^{EFT}=2/3, \tag{5.13}$$

while [113]

$$F_\Box^{EFT}=-2/3. \tag{5.14}$$

Both factors in the HEFT approximation are just constant numbers, insensitive to the process kinematics. Therefore computing NLO corrections results in K-factors (ratios between NLO and LO computations), that are flat in the phase space od the process [114]. The MES expression in (5.5) in HEFT reduces to:

$$\left|F_\triangle^{EFT}C_\triangle+F_\Box^{EFT}C_\Box\right|^2=(2/3)^2\left(\frac{\lambda_{3h}^2v^2}{(\hat{s}-M_h)^2}-\frac{2\lambda_{3h}v}{\hat{s}-M_h}+1\right). \tag{5.15}$$

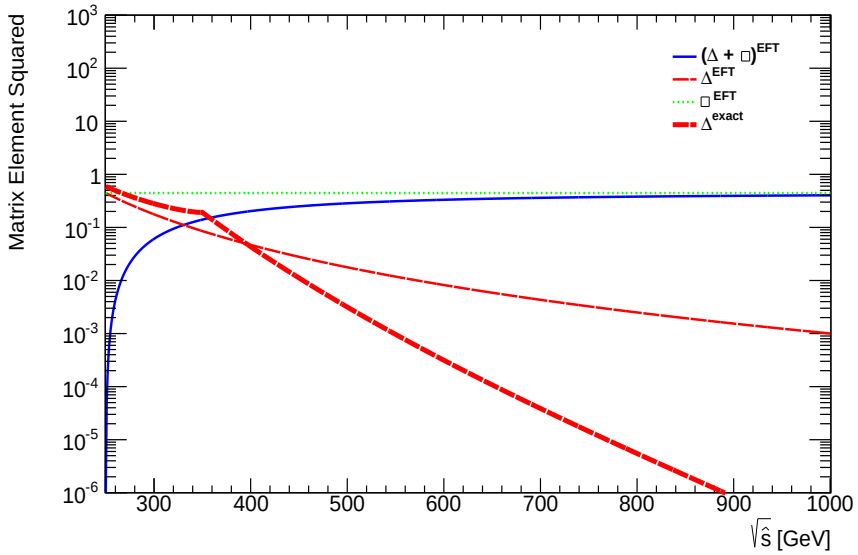

Figure 5.2: Comparison between: $\triangle^{EFT} \equiv |C_{\triangle} F_{\triangle}^{EFT}|^2$ (red-dashed), $\square^{EFT} \equiv |C_{\square} F_{\square}^{EFT}|^2$ (green-dotted), $(\triangle + \square)^{EFT} \equiv |C_{\triangle} F_{\triangle}^{EFT} + C_{\square} F_{\square}^{EFT}|^2$ (blue-solid), $\triangle^{\text{exact}} \equiv |C_{\triangle} F_{\triangle}|^2$ (thick red-dot-dashed).

5.2.1 Kinematical distributions

Next, we compare the exact and HEFT calculations of the leading order Higgs pair production cross-section. To do so, matrix elements squared are convoluted with gluon density functions CTEQ6l [125]. The factorisation scale equal to the renormalisation scale is set dynamically to $\mu_R = \mu_F = \sqrt{\hat{s}}$. The exact calculations are obtained using Madgraph5 DiHiggs model [126] out-of-the-box. [1] To perform the HEFT calculations Madgraph5 [65] was adapted by adding the effective quartic *gghh* coupling using Feynman rules in Ref. [114]. Because both *ggh* and *gghh* vertices were added separately in the code, individual contributions for the triangle and box diagrams in HEFT could be extracted by setting either of the couplings *ggh*=0 or *gghh*=0.

In Fig. 5.2 the behaviour of various terms entering matrix element squared of eq.(5.5) as a function of centre-of-mass energy $\sqrt{\hat{s}}$ is displayed. The contri-

[1] At the time when this study was performed, the MC generation of double Higgs production was not a part of the default Madgraph5 distribution and was available from the web page https://cp3.irmp.ucl.ac.be/projects/madgraph/wiki/HiggsPairProduction

bution sensitive to Higgs self-coupling, $|C_{\triangle}F_{\triangle}^{EFT}|^2$, is shown in dashed line, the box contribution $|C_{\square}F_{\square}^{EFT}|^2$ in dotted line, and the full MES $|C_{\triangle}F_{\triangle}^{EFT} + C_{\square}F_{\square}^{EFT}|^2$ in solid line. In addition, the non-approximated $|C_{\triangle}F_{\triangle}|^2$ term is depicted in dot-dashed line. This figure demonstrates that the genuine self-coupling contribution is only important for centre-of-mass energy smaller than 400 GeV, thus close to the threshold energy of the two Higgs bosons. The box contribution however, dominates over almost the full range for $\sqrt{\hat{s}}$. Near $\sqrt{\hat{s}} \simeq 2 \times m_h$ the interference between the triangle and box leads to sizeable cancellations in the total matrix elements. The reason behind the self-coulping contribution term being restricted in the narrow energy ranges is the presence of three Higgs boson propagators. The intermediate one is probed far off-shell at $\sqrt{\hat{s}} \gg m_h$. Therefore, the size of the triangle term decreases much faster than the size of the box term, in which this propagator is absent. The figure also demonstrates a large discrepancy between exact and approximate calculations of the triangle contribution for $\sqrt{\hat{s}} \gg 2m_q$.

To further asses the quality of the HEFT approximation we compare the kinematical distributions of the two Higgs bosons: the opening angle between the two Higgs momenta and the inclusive Higgs pseudorapidity. In the first case the comparison is made for the triangle and box contributions separately, while in the second the full cross-section is analysed. The results are shown in Fig. 5.3. For the triangle, both exact and approximate calculations give similar shapes. For the box, the difference between exact and HEFT calculations decreases when the Higgses get more back-to-back. The exact calculations show a larger preference for the two Higgses to have a small opening angle. This effect is less pronounced in the EFT calculations and can be explained by analysing the bottom graph in Fig. 5.3. Here, the rapidity of each Higgs is presented. Loop calculations result in a broader distribution which, is caused by larger differences between the Bjorken x of the colliding gluons. As a result, the di-Higgs system receives a larger longitudinal boost despite lower mean value of $\sqrt{\hat{s}}$. HEFT calculations do not represent well the kinematics of Higgs pair production. The oversimplification is most pronounced in the dominant contribution to the cross-section stemming from the box diagram.

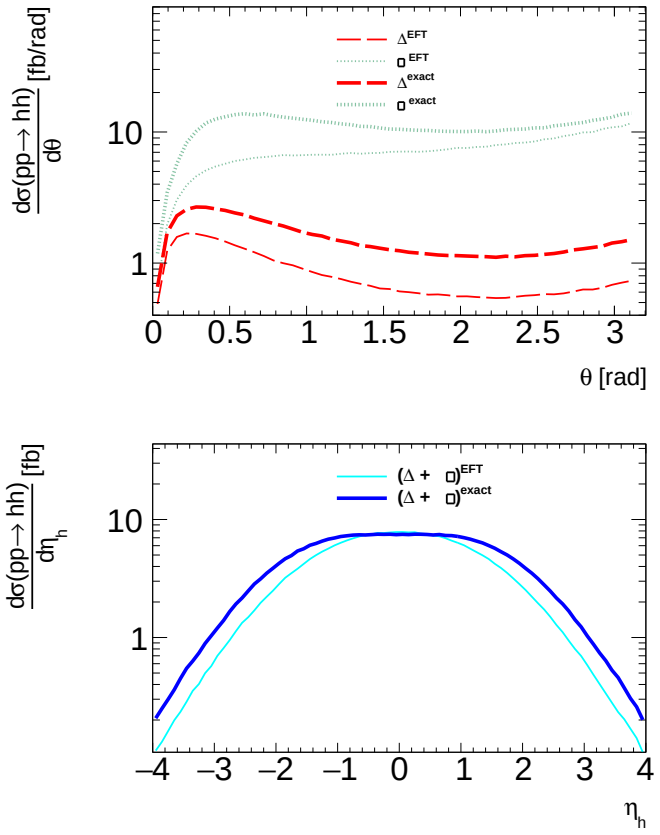

Figure 5.3: Top plot: comparison between the distributions of the opening angle between the two Higgs momenta in EFT (thin lines) and exact calculation (thick lines) for the triangle (red lines) and box (green lines). Bottom plot: Comparison between the inclusive Higgs pseudorapidity distributions for EFT (thin light line) and exact (thick dark line) calculation.

5.3 Sensitivity to trilinear coupling

The main motivation behind studying double Higgs boson production is the measurement of the Higgs self coupling parameter. If the magnitude of the Higgs self-coupling is not in accordance with its SM value, the electroweak symmetry breaking is not, or only in part, a result of the SM Higgs potential of eq. (2.7). As a consequence, m_h, VEV and λ_{3h} in eq. (5.2) are decoupled and the observed 125 GeV resonance is not the SM Higgs. It may instead be a member of a more extended sector (see for instance [127]) or be composite and strongly interacting [8, 128].

In the following, λ_{3H}^{BSM} denotes the BSM modifications to the value of λ_{3h} and is a free parameter in the cross-section calculation. I do not focus on any model in particular and therefore do not modify any other SM parameter. The range of variation of the Higgs trilinear coupling is parametrised using the ratio $\kappa_\lambda \equiv \frac{\lambda_{3H}^{BSM}}{\lambda_{3h}}$. Coupling modifier κ_λ is probed in the range $[-10, 10]$. This range is broad given that EFT is a small modification to the SM, but as will be shown in later chapters, it matches experimental constrains.

5.3.1 Cross-section sensitivity

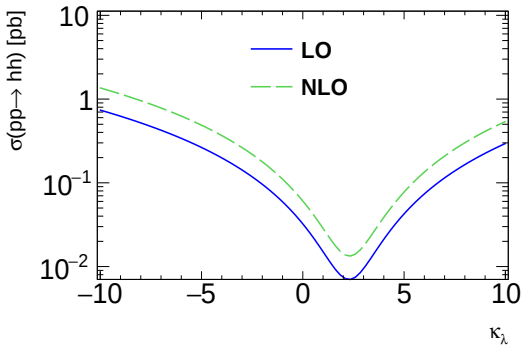

Figure 5.4: Higgs pair production cross-sections at $\sqrt{s} = 14$ TeV for different values of κ_λ.

The Higgs pair production cross-section depends on κ_λ through the triangle contribution and the triangle-box interference. The former changes quadratically with κ_λ, while the latter shows a linear dependence. This be-

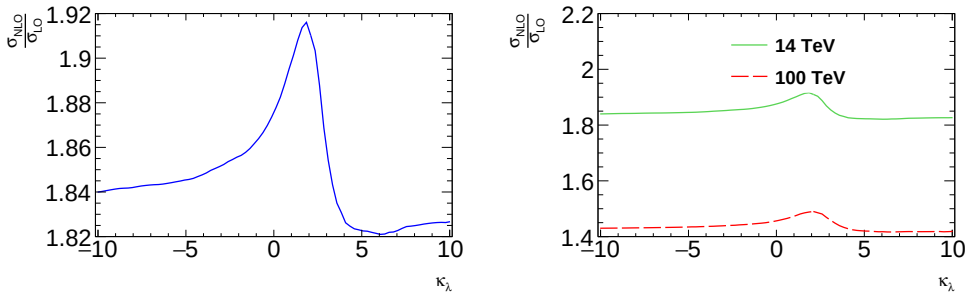

Figure 5.5: NLO K factors as a function of κ_λ at $\sqrt{s} = 14$ TeV (left plot) and for $\sqrt{s} = 14$ and 100 TeV (right plot).

haviour is depicted in Fig. 5.4 showing the di-Higgs cross-section at $\sqrt{s} = 14$ TeV as a function of κ_λ at LO (solid line) and NLO (dashed line). The results were obtained using [113, 114]. At NLO the Born term was computed with exact quark loop and the QCD corrections were included in EFT approximation.

For $\kappa_\lambda = 0$ only the box contribution is present and the cross-section is larger than for $\kappa_\lambda = 1$. For $\kappa_\lambda < 0$ the interference term flips sign, which is why the cross-section becomes larger than for corresponding positive κ_λ. To quantitatively determine the size of the individual contributions I compare LO cross-sections for $\kappa_\lambda = 1, 0$ and -1. In this way I find that $\sigma^{\Box} \simeq 35$ fb, $\sigma^{int} \simeq -25$ fb, $\sigma^{\triangle} \simeq 5$ fb, while the total SM cross-section $\simeq 17$ fb. Due to the large box contribution the sensitivity of the total cross-section to κ_λ is small. Fig. 5.4 shows large differences between LO and NLO. The NLO K-factor ($\equiv \sigma^{NLO}/\sigma^{LO}$) is displayed in Fig. 5.5 (left) as a function of κ_λ. For $\kappa_\lambda = 1$ the K-factor becomes rather large $\simeq$1.92 [2] (see Table 5.3). It slightly dependends on κ_λ due to different QCD corrections to box and triangle contributions. In the right plot in Fig. 5.5 the K-factors at $\sqrt{s} = 14$ TeV and 100 TeV are compared. The numbers are obtained from HPAIR [129] program with CTEQ6 [130] PDFs. As expected, the role of NLO corrections is smaller at higher $\sqrt{s}$. The absolute value of the di-Higgs cross-section at 100 TeV is over a factor of 100 larger than at 14 TeV (see Table 5.3). The sensitivity to different values of κ_λ is, however, smaller.

The discussion above was limited to the largest Higgs pair production

[2] This value is larger than quoted in [114] (1.92 instead of 1.86) as I used a more recent set of PDFs.

channel, gluon fusion, in view of experimental application of these findings. The sensitivity of different di-Higgs production channels to different values of κ_λ can be found for example in ref. [116]. While the Higgs pair production cross-sections in some of these channels present stronger variations as a function of κ_λ, gluon fusion remains the most sensitive one to κ_λ parameter.

5.3.2 Particle level assessment

Since the overal cross-section only weakly depends on the Higgs trilinear coupling, it is worth to find experimentally accessible phase space, in which this dependence might be enhanced.

At first, let us look at expected event yields in selected di-Higgs decays. In Table 5.3 the total event yields for $b\bar{b}b\bar{b}$, $b\bar{b}W^+W^-$, $b\bar{b}Z^0Z^0$, $b\bar{b}\gamma\gamma$, and 4γ final states are given. They are based on the LO [126] (NLO [114]) Higgs pair production cross section: 3.58 (9.22) fb, 16.23 (33.86) fb, and 877 (1350) fb at 8, 14, and 100 TeV, respectively and LO Higgs branching ratios. The following three variants are compared: ATLAS and CMS LHC Run I conditions of proton-proton centre-of-mass energy of 8 TeV with an integrated luminosity of 20 fb^{-1}, High Luminosity LHC with 3000 fb^{-1} at 14 TeV, and 3000 fb^{-1} at a possible future 100 TeV hadron collider. The numbers are based on Higgs pair production cross-sections at LO and NLO [114] taking into account the proper Higgs branching ratios [131]. I select final states in which one Higgs boson decays to a pair of bottom quarks to maximise event yields. Except for both Higgses decaying into bottom quarks, the choice of decay channels of the other Higgs boson is motivated by experimental capabilities of separating the signal from multi-jet and multi-lepton backgrounds.

The 4γ channel suffers from lack of statistics and is not prospective for the LHC and HL-LHC. One might argue, however, that this final state poses a real challenge at a 100 TeV hadron collider (21 events). To provide sufficient statistics at the HL-LHC, at least one Higgs decay should have a large branching ratio, for instance $b\bar{b}$ or $\tau^+\tau^-$. The $b\bar{b}b\bar{b}$, $b\bar{b}W^+W^-$ and $b\bar{b}Z^0Z^0$ channels suffer from large backgrounds. The $b\bar{b}\gamma\gamma$ final state compromises between reasonable statistics and a relatively clean experimental signature. I examine whether this signal can be distinguished from irreducible $b\bar{b}\gamma\gamma$ backgrounds resulting from QCD, QED and single Higgs production ($Z^0h(\gamma\gamma)$, $b\bar{b}h(\gamma\gamma)$).

I study $pp \to hh \to b\bar{b}\gamma\gamma$ neglecting initial and final state radiation. Moreover, possible dilution effects due to reconstruction inefficiencies or mis-

Table 5.3: Branching ratios to various di-Higgs decay channels, expected event yields in these channels for di-Higgs production in gluon fusion, based on the LO [126] (NLO [114]) Higgs pair production cross sections

hh final state	Br. Ratio	8 TeV(20 fb^{-1}) LO (NLO)	14 TeV (3000 fb^{-1}) LO (NLO)	100 TeV (3000 fb^{-1}) LO (NLO)
$b\bar{b}b\bar{b}$	32.5%	23 (60)	16×10^3 (33×10^3)	0.85×10^6 (1.3×10^6)
$b\bar{b}W^+W^-$	23.9%	17 (44)	12×10^3 (24×10^3)	0.63×10^6 (0.97×10^6)
$b\bar{b}Z^0Z^0$	3.0%	2.2 (5.5)	1.5×10^3 (3×10^3)	0.08×10^6 (0.12×10^6)
$b\bar{b}\gamma\gamma$	0.26%	0.19 (0.48)	128 (264)	6800 (10500)
$\gamma\gamma\gamma\gamma$	0.001%	0 (0)	0.25 (0.53)	14 (21)

reconstruction are not taken into account. Therefore other (reducible) backgrounds containing for instance two photons and two light quark jets, top anti-top pairs, top anti-top pairs with single photons, and top anti-top pairs with Higgses decaying into two photons are not included in the study.

There have been several phenomenological studies on the feasibility of measuring Higgs pair production in the $b\bar{b}\gamma\gamma$ channel, see for instance [116, 132, 133]. In [132] the angular separation between photons were proved to be an efficient discriminant between the signal and the background. Ref. [133] demonstrated the usefulness of transverse momentum spectra in distinguishing signals with BSM self coupling values. Using these findings, I search for kinematical regions, in which the sensitivity to the trilinear coupling is largest by analysing individually the box and triangle contributions to differential cross-sections of Higgs pair production. Additionally, I discuss the feasibility of separating the genuine self-coupling from the irreducible $bb\gamma\gamma$ background.

In order to maintain reasonable acceptance of small di-Higgs signal, the number of selection requirements should be small. Therefore, they are limitted to lower cuts on transverse momentum and rapidity (motivated by trigger capabilities and detector coverage), narrow windows around the invariant mass of each of the two Higgs bosons reconstructed from its decay products, and correlations among momenta of these final state particles. The momenta

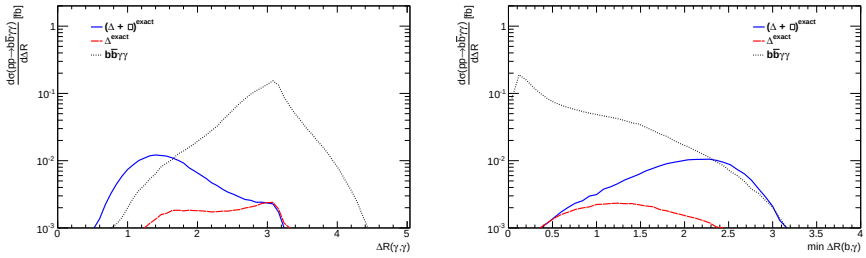

Figure 5.6: The distributions of $\Delta R(\gamma,\gamma)$ (left plot) and $\Delta R(b,\gamma)_{\text{min}}$ (right plot) for the two contributions to the LO SM Higgs pair production (blue-solid line), for the self-coupling part (red-dashed line) and for the irreducible $b\bar{b}\gamma\gamma$ background (black-dotted line). Plots obtained with Madgraph5.

of photons and b-quarks from each Higgs boson decay tend to be close together and well separated from decay products of the other Higgs boson. On the other hand, non-resonant $bb\gamma\gamma$ background features often photons radiated colinearly off b-quarks. This property is expressed in terms of $\Delta R(k,l)$ separation between two particles k and l:

$$\Delta R(k,l) = \sqrt{(\eta_k - \eta_l)^2 + (\phi_l - \phi_k)^2}, \tag{5.16}$$

where η and pseudo-rapidities and ϕ are azimuthal angles of the particles' momenta. Optimising angular separations among b-quarks and photons will be the main concern of this study.

The following requirements are applied to the $bb\gamma\gamma$ samples [132]:

$$\begin{aligned} &p_T(b) > 45 \text{ GeV},\ |\eta(b)| < 2.5,\ \Delta R(b,b) > 0.4, \\ &p_T(\gamma) > 20 \text{ GeV},\ |\eta(\gamma)| < 2.5,\ \Delta R(\gamma,\gamma) > 0.4, \end{aligned} \tag{5.17}$$

and

$$|m_{bb} - m_H| < 20 \text{ GeV}, |m_{\gamma\gamma} - m_H| < 2.3 \text{ GeV}. \tag{5.18}$$

Fig. 5.6 shows the ΔR separation between the two photons (left plot) and between the photon and the b-quark that are closest in phase space (right plot). The individual distributions for the full cross-section (blue-solid line), the genuine self-coupling contribution (red-dashed line), and $bb\gamma\gamma$ background (black dotted line) are presented. The background consists of both non-resonant production and single Higgses processes. The latter are calculated using the HEFT approximation [65]. The distribution of ΔR between

photons for the Higgs pair reaches a maximum at $\Delta R(\gamma,\gamma) \simeq 1.5$ due to the large boost of the di-Higgs system. It is well separated from the background, in which the two photons do not stem from the same parent. The kinematical properties of the triangle and triangle+box samples are different due to the domination of the box. The former favours $\Delta R(\gamma\gamma) \simeq 3$ while the latter has a maximum for small values of ΔR. The minimum separation between a photon and a b ($\bar{b}$) quark, shown in the right plot in Fig. 5.6, in the background is small as most photons are emitted from the quarks and hence prefer to be collinear with their parents. In the two di-Higgs samples on the other hand, photons are the Higgs decay products and are much more separated. The relatively large contribution from the box increases the separation between the decay products of the two Higgs bosons. Fig. 5.6 demonstrates additionally that kinematical shapes of the genuine self-coupling contribution and the irreducible background are very similar, making this signal extremely challenging to isolate.

Fig. 5.7 presents the differential cross-sections for the processes $pp \to hh \to b\bar{b}\gamma\gamma$ and $pp \to b\bar{b}\gamma\gamma$ after applying the cuts of eqs. (5.17) and (5.18). The SM Higgs pair production is displayed as solid line, the genuine self-coupling as dashed, BSM Higgs pair production with $\kappa_\lambda = 10$ as dotted, and irreducible $b\bar{b}\gamma\gamma$ background as dashed-dotted line. I choose a BSM model with $\kappa_\lambda = 10$ because its cross-section is approximately 60 times larger than that of the pure triangle and two times larger than the irreducible background, reaches the maximum at $\sqrt{\hat{s}} = 270$ GeV and decreases exponentially for large $\sqrt{\hat{s}}$. Unlike the SM cross-section at $\sqrt{\hat{s}} < 400$ GeV, at large values of κ_λ the cancelations due to negative interference are negligible. On the other hand, at $\sqrt{\hat{s}} > 750$ GeV SM and BSM cross-sections become about equal as all sensitivity to Higgs trilinear coupling is lost.

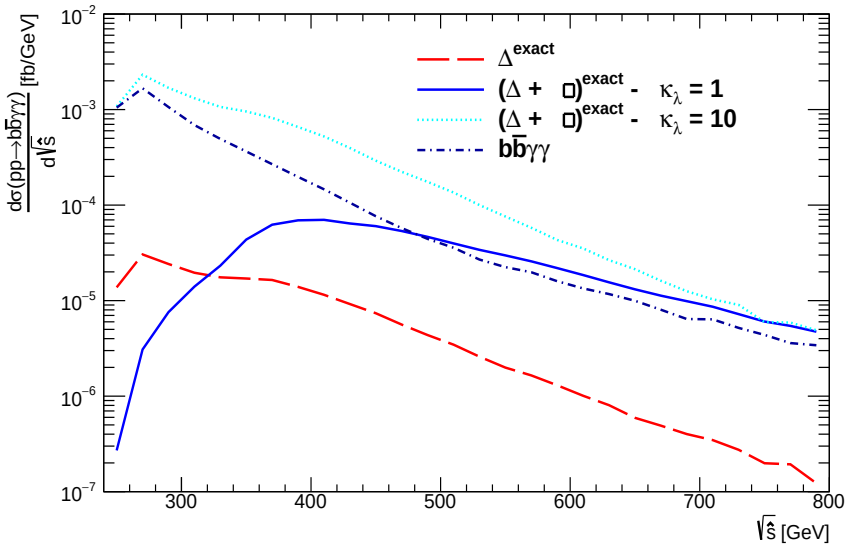

Figure 5.7: The differential di-Higgs production cross-section for $\kappa_\lambda = 1$ (dark blue-solid line), $\kappa_\lambda = 10$ (light blue-dotted line) and genuine self-interactions (red-dashed line) and $b\bar{b}\gamma\gamma$ background differential cross-section (black dash-dotted line). The cuts of eq. (5.17) and (5.18) are applied.

5.3.3 Feasibility studies for future measurements

The upgrade of the LHC to higher luminosities (HL-LHC) offers potentially sufficient amount of data to observe pairs of Higgs bosons. It is therefore vital to study the feasibility of observing pairs of Higgs bosons and measuring their self-couplings in the anticipated conditions of a modernised ATLAS detector. In the following I continue the investigation of the trilinear coupling in Higgs pair production in gluon fusion with the Higgs bosons decaying into $b\bar{b}\gamma\gamma$.

The aim of this study is to improve a separation between the κ_λ-dependent part of the di-Higgs signal and irreducible background. Both the SM scenario, as well as the one with κ_λ increased by a factor of 10 are analysed. Using kinematical selection proposed originally in ref. [132] I optimise it to improve sensitivity specifically to the Higgs self-coupling. This study is performed on particle level. Further investigation, including assumed particle reconstruction efficiency in the upgraded ATLAS detector will be left out for Chapter 8.

In Fig. 5.8 ΔR distributions are shown for the decay products of the SM and BSM Higgs pairs and for the irreducible $bb\gamma\gamma$ background. The red dashed line corresponds to $\kappa_\lambda = 10$, blue dash-dotted line to $\kappa_\lambda = 0$, solid line to the SM and black dotted line to the $b\bar{b}\gamma\gamma$ background. As the triangle contribution dominates at small $\sqrt{\hat{s}}$ mean separation between the two photons (upper plot) is larger for $\kappa_\lambda = 10$ than for $\kappa_\lambda = 0$. The shape of the pure box sample resembles the SM and its larger cross-section is due to the absence of negative interference. The minimum separation $\Delta R(b, \gamma)$ (bottom plot) is on average smaller for $\kappa_\lambda = 10$ than for pure box. The larger cross-section for $\kappa_\lambda = 10$ with $\Delta R(b, \gamma) > 0.4$ on the other hand, separates the triangle from the kinematically similar background. For $\kappa_\lambda = 0$ the signal exceeds the background for $\Delta R(b, \gamma) > 2$.

Three variants of kinematical selection based upon ΔR distribution are analysed and sensitivity for each type of signal is computed. I consider only the largest background originating from $b\bar{b}\gamma\gamma$ processes, that kinematically resembles the self-coupling contribution. The addition of other relevant backgrounds will be addressed in Chapter 8. The centre-of-mass energy is set to the value of $\sqrt{s} = 14$ TeV, and the integrated luminosity of 3000 fb, following expected HL-LHC conditions. To estimate sensitivity, I apply the formula $\frac{N_{signal}}{\sqrt{N_B}}$, because both the expected number of signal (N_S) and background events (N_B) are sufficiently large in these conditions. The proposed three

Table 5.4: The number of events in: $b\bar{b}\gamma\gamma$ background, SM and BSM with $\kappa_\lambda = 10$ predicted for the luminosity upgraded LHC ($\mathcal{L} = 3000$ fb^{-1}) together with their respected sensitivities, computed as ratios of the number of signal events over square root of number of background events.

Cuts	N_B	$N_{S(\kappa_\lambda=1)}$	$N_{S(\kappa_\lambda=10)}$	$N_{S(\kappa_\lambda=1)}/\sqrt{N_B}$	$N_{S(\kappa_\lambda=10)}/\sqrt{N_B}$
Before cuts	–	128	2280	–	–
eq. (5.17)	166950	48	726	0.12	1.78
eq. (5.18)	395	48	726	2.43	36.53
eq.(5.19a)	26	35	189	6.80	36.85
eq.(5.19b)	41	39	256	6.10	40.16
eq.(5.19c)	240	48	679	3.08	43.84

phase space selections are as follows:

$$\Delta R(\gamma,\gamma) < 2, \quad \Delta R(b,\gamma) > 1.0; \tag{5.19a}$$

$$\Delta R(\gamma,\gamma) < 2.2, \quad \Delta R(b,\gamma) > 0.4; \tag{5.19b}$$

$$\text{no cut on } \Delta R(\gamma,\gamma), \quad \Delta R(b,\gamma) > 0.4; \tag{5.19c}$$

Table 5.4 shows the event yields after applying signal selection in the three variants. The background is generated with the cuts of eq. (5.17) excluding potential soft and collinear singularities. The invariant mass cuts of eq. (5.18) significantly reduce the background and retain the SM and BSM signal. The separation between photons and b-type quarks and between two photons, $\Delta R(b,\gamma)$ and $\Delta R(\gamma,\gamma)$, must be chosen differently to optimise for the SM and BSM signals. The requirements of eq. (5.19a) give the best results for SM di-Higgs production and are less efficient for large values of κ_λ. The selection dictated by eq. (5.19c), on the other hand, are optimised for $\kappa_\lambda = 10$.

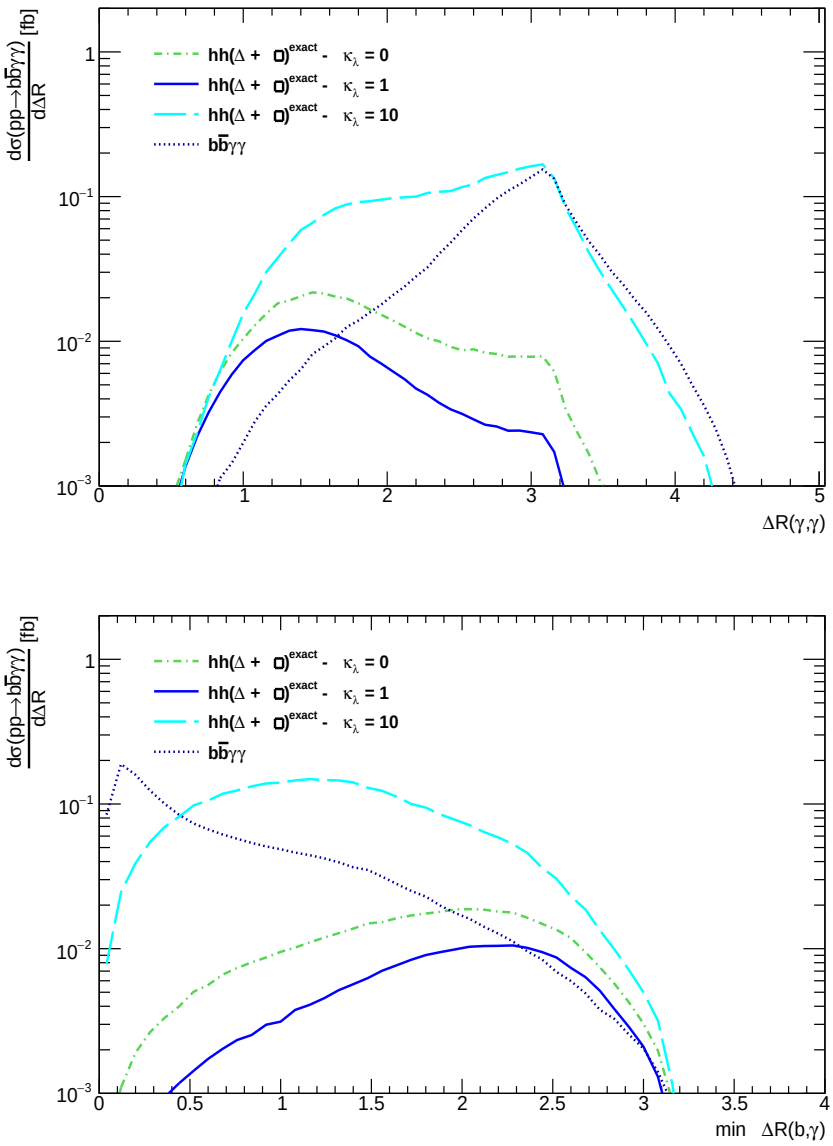

Figure 5.8: $\Delta R(\gamma,\gamma)$ (upper plot) and $\Delta R(b,\gamma)_{\text{min}}$ (lower plot) for SM di-Higgs production (dark blue-solid line), BSM with $\kappa_\lambda = 10$ (dark blue-dashed line), BSM with $\kappa_\lambda = 0$ (green dash-dotted line) and irreducible background (black-dotted line). The cuts of eqs. (5.17) and (5.18) have been applied.

5.4 Summary

The production of pairs of Higgs bosons enables the measurement of their self-couplings, and thus provides a direct measurement of the Higgs boson potential. The cross-section for this process is about three orders of magnitude smaller than in case of a single Higgs boson production, making it a challening to observe even at the High Luminosity LHC. In this Chapter Higgs pair production in gluon fusion with the Higgs bosons decaying into $b\bar{b}\gamma\gamma$ is investigated.

As the di-Higgs cross-section is small, detailed knowledge on the kinematics is required to improve signal extraction. Several cross-section predictions in the literature propose kinematical selections based upon HEFT approximation (infinite top quark mass) [114, 116, 124]. In this Chapter these approximations are compared with an exact calculation of signal matrix element at leading order. At $\sqrt{\hat{s}} \simeq 2m_q$ the differences between two calculations are large. HEFT neglects part of the complicated structure of the box contribution to the cross-section, increasing significantly the discrepancy of cross-sections present already in the computation of the triangle contribution. For the exact calculation a larger longitudinal boost and on average smaller opening angle between the Higgs bosons is obtained, in agreement with previous studies [134–136].

The behaviour of both triangle and box contributions was studied over a large interval of $\sqrt{\hat{s}}$. At large values of $\sqrt{\hat{s}}$ the cross-section does not depend on the trilinear coupling, as it is dominated by the box contribution. This is in agreement with the observations presented in [133]. The main finding of this Chapter is that the sensitivity of the total di-Higgs production cross-section to κ_λ is largest at its threshold, $\sqrt{\hat{s}} \simeq 2m_h$. In order to find experimental selection criteria maximising sensitivity to anomalous κ_λ in the $b\bar{b}\gamma\gamma$ final state, I optimised the kinematical cuts proposed in ref. [132]. I found that kinematical selection of (5.19c) maximises sensitivity to anomalous $\kappa_\lambda = 10$.

The study presented in this Chapter inspired feasibility study of measuring κ_λ at the HL-LHC, described in Chapter 8 as well its measurement using LHC Run 2 data, presented in Chapter 7.

6 Higgs Pair searches with the Run 1 dataset

The conclusion of the previous chapter is that the SM Higgs pair production is an extremely challenging process to observe, even with the HL-LHC gigantic dataset. During Run 1 of the LHC protons were collided at centre-of mass energy of 8 TeV and the integrated luminosity delivered in these collisions reached 20.3 fb^{-1}. The cross-section of Higgs pair production through gluon fusion at 8 TeV (10.16 fb [2]) is four times smaller than at HL-LHC energy of 14 TeV. With the luminosity about 150 times smaller, it is highly unlikely to observe SM di-Higgs events. Therefore, in Run 1 ATLAS and CMS focused on searches for BSM Higgs pair production, exploring models that predict sizeable cross-section increase with respect to the SM.

These BSM extensions can be divided into two categories: models predicting the largest enhancement in resonant double Higgs production and models postulating larger event yields only due to non-resonant processes leading to Higgs pairs in the final state. The former can be studied using simplified models that result from supplementing the SM with a scalar particle that couples to the Higgs boson as well as more complex theories, for example Minimal Sypersymmetric Standard Model (MSSM) [137]. Their experimental signature features a resonance peak in the di-Higgs invariant mass spectrum, corresponding to the mass of the unknown resonance. Non-resonant modifications of Higgs pairs production are studied using the framework of effective field theories (EFT). EFT parametrises possible subtle deviations in kinematical distributions related to di-Higgs production with coefficients of dimension-6 operators added to the SM.

In Run 1 analyses, the production proces through gluon-gluon fusion, dominant in the SM, is studied. SM Higgs production searches are complemented with BSM resonant models. Analyses in ATLAS focus on four

final states. The one, in which both Higgses decay to a pair of b-quarks, profiting from the largest Higgs branching fraction within the SM, was studied in Ref. [138] Two channels with one Higgs boson decaying to $b\bar{b}$ and the other Higgs required to decay to $\gamma\gamma$ [139] or $\tau\tau$ profit from smaller the SM background and enable selection of events closer to di-Higgs production threshold. The fourth channel features one Higgs decaying to WW^* with a subsequent leptonic decay and the other Higgs boson to $\gamma\gamma$. In CMS three decay channels are investigated using this dataset: $bbbb$ [140, 141], $bb\gamma\gamma$ [142] and $bb\tau\tau$ [143].

In the following I focus on results of statistical combination of ATLAS results published in Ref [3], that presents Run 1 studies in their most mature form. Each analysis sets limits on both the SM Higgs pair production (called also non-resonant analysis) and BSM Higgs pair production mediated additionally by a BSM neutral heavy scalar (resontant analysis). In the next section details on Monte Carlo generated samples are given. In Section 6.2 all analyses are briefly presented, followed by the description of the statistical procedure in Section 6.3. Results of SM and BSM searches are discussed in Sections 6.4 and 6.5.

6.1 Monte Carlo samples

Signal events are simulated using Madgraph 5 v1.5.14 matrix element at the leading order in QCD. At the time, models available for di-Higgs studies, that featured exact loop contributions, were available outside the official Madgraph release. [1] The Standard Model Higgs pair production is simulated using the "SM" and the spin-0 resonant production using the "HeavyScalar" model [144]. For the signal, as well as other simulated processes Pythia 8.175 [63] generator is used for modeling parton showering, hadronisation and underlying event. Parton distribution functions CT10 [145] and CTEQ6L1 [125] are used.

Single Higgs boson production through gluon fusion and vector boson fusion are generated with Powheg [71, 146, 147] at the next-to-leading-order in QCD (and interfaced with Pythia 8 parton shower). For generating events of associated Higgs production with a vector boson or a pair of top quarks

[1] All mentioned models are available for download from the web page https://cp3.irmp.ucl.ac.be/projects/madgraph/wiki/HiggsPairProduction.

PYTHIA 8 is used. All Higgs processes are normalised to the theoretical predictions available at the time [131, 148, 149].

Processes involving vector bosons and jets ("V+jets") enter analyses due to misidentification of a jet as a lepton. Their contributions are estimated from data.

6.2 Overview of analyses

6.2.1 The $bb\gamma\gamma$ analysis

Events selected in the $bb\gamma\gamma$ analysis are required to contain two energetic isolated photons. The largest of the photons' transverse momentum must be larger than 35% of the invariant di-photon mass $m_{\gamma\gamma}$, while the second largest must be larger than 25% of $m_{\gamma\gamma}$. The di-photon mass must be compatible with the Higgs boson mass, namely $105 < m_{\gamma\gamma} < 135$ GeV. Additional requirements impose the presence of two b-tagged jets, with transverse momenta of at least 55 and 35 GeV for the leading and subleading jets, respectively. Jets are tagged using a multivariate algorithm [150] with estimated 70% efficiency. Smaller efficiency with respect to the algorithm applied in the HL-LHC search results in lower signal acceptance (as fewer b-jets are correctly identified) and sizeable reduction of backgrounds originating from mis-tagged light-flavour or gluon jets. The invariant mass of the tagged two b-jets must be in the range of $95 < m_{bb} < 135$ GeV, compatible with the Higgs mass within experimental resolution.

Dominant background processes, related to continuum $bb\gamma\gamma$ production, are evaluated from data using events with $m_{\gamma\gamma} \in [105, 120]$ GeV and $m_{\gamma\gamma} \in [130, 160]$ GeV (sidebands of the di-photon mass). Background processes originating from a single Higgs boson production (with the Higgs boson decaying to a pair of photons) are evaluated from simulations.

In the non-resonant analysis the signal is extracted from an unbinned fit performed to signal and background on the observed $m_{\gamma\gamma}$ distribution. The background from single Higgs boson production is constrained to the SM prediction. The continuum background is modeled with an exponential function following the prescription described in Ref. [151], see bottom panel of Figure 6.1a. The shape of the background is obtained from a fit to a control region. The control region is defined using events containing a pair of photons and a pair of jets with fewer than two jets b-tagged. This region offers thus a

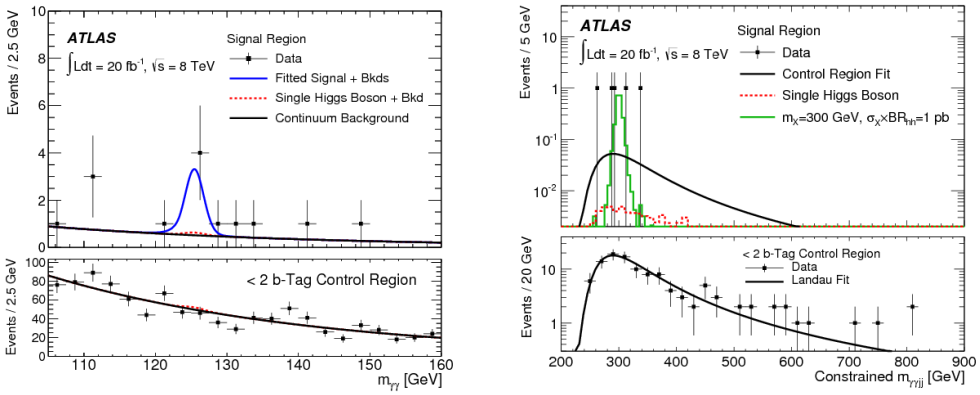

(a) Non-resonant analysis (b) Resonant analysis

Figure 6.1: Estimation of signal and background in the $bb\gamma\gamma$ analysis. Plots taken from [139]. Details are given in the text.

larger dataset than the signal, and of the same kinematical properties. This is illustrated in the lower panel of Fig 6.1b. Extrapolating the sidebands shape into the $m_{\gamma\gamma}$ window of the signal selection, see Figure 6.1a, leads to a prediction of 1.3 background events from the continuum production and 0.2 events originating from single Higgs boson production. The number of observed events in the signal region is five, representing an excess of 2.4 standard deviations (σ). A 95% confidence level (CL) upper limit of 2.2 (1.0) pb is observed (expected) for the Higgs boson pair production cross-section.

In the BSM resonant analysis total event yields in the signal region are used in the fit. The signal selection procedure is the same as the non-resonant search with an additional requirement on the reconstructed di-Higgs mass, $m_{bb\gamma\gamma}$. This requirement varies with the resonance mass hypothesis under evaluation, and is defined as the smallest window containing 95% of the signal events based on MC simulation. The continuum background is extrapolated from the sidebands of invariant mass $m_{jj\gamma\gamma}$ in the control region, see bottom panel in Fig. 6.1b. The single Higgs background is estimated from simulations. The search is performed for a range of resonance masses m_H between 260 GeV and 500 GeV. The observed (expected) upper limits on cross-section times branching ratio for producing a scalar resonance H that decays into a pair of SM-like Higgs bosons h, $\sigma(gg \to H) \times Br(H \to hh)$, are 2.3 (1.7) pb at the resonance mass $m_H = 260$ GeV and 0.7 (0.7) pb at $m_H = 500$ GeV.

6.2.2 The *bbbb* analysis

This analysis is designed to search for highly boosted pairs of Higgs bosons decaying to pairs of b-quarks. In this kinematical region, each bb system can be reconstructed either as a pair of b-quark jets (the so-called "resolved analysis") or as a large jet whose substructure reveals two b-hadrons (the so-called "boosted"), whose invariant mass is consistent with that of the Higgs boson. Both methods have been utilised in Ref. [138], yet for the combination only the selection of events from resolved analysis is used. This topology has many benefits due to the large momentum and angular separation between the two systems which provides a very distinct experimental signature. Signal acceptance benefits from highly efficient b-tagged multijet triggers and excellent rejection of all backgrounds. Additionally, the combinatorial ambiguity in reconstructing Higgs boson candidates from pairs of b-quarks is negligible. This technique offers the best sensitivity in the range of heavy resonance masses $m_H \in [500, 1000]$ GeV and was applied in the statistical combination of searches described in this Section.

In this channel events are selected if they consist of at least four jets, each with transverse momentum $p_T > 40$ GeV, that are b-tagged with a multivariate algorithm [150]. This algorithm has estimated efficiency of 70%. The four b-tagged jets of the highest transverse momenta in the event are then used to form two dijet systems. The transverse momenta of the leading and subleading dijet systems must be greater than 200 and 150 GeV, respectively and the two systems must have the angular separation ΔR smaller than 1.5. Invariant masses of the leading and sub-leading b-jet systems, m_{2j}^{lead} and $m_{2j}^{sublead}$, respectively are required do be consistent with the Higgs boson mass:

$$\sqrt{\left(\frac{m_{2j}^{lead} - 124\text{GeV}}{0.1 m_{2j}^{lead}}\right) + \left(\frac{m_{2j}^{sublead} - 115\text{GeV}}{0.1 m_{2j}^{sublead}}\right)} < 1.6. \qquad (6.1)$$

Denominators of this formula are due to dijet mass resolution that are estimated to be 10% of the dijet mass values. These requirements offer robust background suppression at the price of lowered acceptance of signal events with small masses of the heavy resonance. Therefore, the resonant *bbbb* analysis only searches for particles with masses larger than 500 GeV.

The dominant background in the *bbbb* analysis, estimated to amount to over 90% of all background events in the signal region, stems from multijet processes. Around 10% of background events originate from top quark pair

production. The former class of backgrounds is estimated using data-driven techniques, while the latter is taken from MC simulations. The dominant sources of systematic uncertainty are related to b-tagging and the modeling of the multijet background.

A total of 87 events are observed in the data, in agreement with the SM expectation of 87.0 $\pm$ 5.6 events. These numbers are used to obtain the observed and expected 95% C.L. upper limits on the Higgs pair production cross section, both of which are 202 fb. The resonant search utilises the invariant mass of the four jets as the final discriminant, from which the upper limit on the heavy resonance production cross section is extracted. The resulting observed (expected) 95% C.L. upper limit on $\sigma(pp \to H \to hh \to bbbb)$ ranges from 52 (56) fb, at $m_H = 500$ GeV, to 3.6 (5.8) fb, at $m_H = 1000$ GeV.

6.2.3 The $bb\tau\tau$ analysis

In this first iteration of the Higgs pair search with the $bb\tau\tau$ final state, only semileptonic decays of the τ lepton pairs are considered. This means that only events with one τ lepton decaying hadronically and the other leptonically, are used. Events are required to consist of exactly one light lepton (electron or muon) with transverse momentum at least 26 GeV, one hadronically decaying τ lepton with transverse momentum larger than 20 GeV meeting the medium identification criteria described in Ref. [152], and two or more jets with transverse momenta larger than 30 GeV. The electric charge of the hadronically decaying τ must be opposite to the one of the light lepton. In addition, between one and three of the selected jets must be b-tagged using the multivariate b-tagger [150]. This last requirement ensures that event selections of this and the $bbbb$ analysis are orthogonal.

This analysis has to take into account a wide variety of irreducible backgrounds from: W+jets processes, Z bosons decaying to τ lepton pairs, diboson (WW, WZ, and ZZ) production and processes containing single and double top quarks. They are estimated using both data-driven methods and simulations. Additionally, there is a class of reducible backgrounds, which stem from processes with final state not identical to that of the signal, but are identified as such due to object misreconstruction. For example, events consisting of: W+jets, multijets, Z+ jets, and top quark, in which a jet is misidentified as a hadronically decaying τ lepton, τ_{had}, are referred to as the fake τ_{had} backgrounds. They are estimated using data with a "fake-factor"

method, described in Ref. [152]. The background originating from Z boson decays, $Z \to \tau\tau$, is modeled using more abundant $Z \to \mu\mu$ events in data through embedding [63], where the muon tracks and associated energy depositions in the calorimeters are replaced by the corresponding simulated signatures of τ decays. The estimation of $Z \to \tau\tau$ background using embedding is found to be in a good agreement with the estimation obtained from the MC simulation. Top quark pairs and diboson events as well as single Higgs production are estimated using simulations.

Signal selection proceeds via the reconstruction of the invariant mass $m_{\tau\tau}$ of the two τ leptons. The four-momentum of the hadronically decaying τ (τ_{had}) is reconstructed from its decay products forming a jet. The kinematic information about leptonically decaying τ (τ_{lep}) is incomplete because τ_{lep} decays to an electron or muon and their corresponding neutrino. Neutrino momentum parallel to the beam axis is undetected and transverse momentum can be reconstructed indirectly from the measured energy imbalance E_T^{miss}. The analysis uses therefore an approximate method called the missing mass calculator (MMC) [153] that computes the most probable value of the ditau mass, assuming that the observed lepton, τ_{had} and E_T^{miss} stem from one resonance.

Additional topological requirements are applied to reduce the background originating from top quark pair decays, $tt \to WWbb$. The $tt \to WWbb \to l\nu\tau_{had}\nu bb$ process features both τ_{had} and an electron or muon, that originate from decays of different W bosons and are uncorrelated. In the signal, both τ_{lep} and τ_{had} stem from the Higgs boson. Due to the presence of more neutrinos in the τ_{lep} decays, transverse momentum of a lepton is typically smaller than a transverse momentum of τ_{had}. Thus the p_T of an electron or muon must fulfill the inequality: $p_T^{lep} < p_T^{\tau_{had}} + 20$ GeV. The semi-leptonic top quark pairs decays, $tt \to WWbb \to l\nu qq'bb$, in which either of the quarks is misidentified as a τ_{had} are constrained in the following way: From a τ_{had} candidate and its closest untagged jet its invariant mass $m_{\tau j}$ is computed. In the background events this mass should be consistent with a mass of a W boson. Further, the W boson candidate is paired with a b-tagged jet to form a top quark candidate and a mass $m_{\tau jb}$ is calculated. If $(m_{\tau j}, m_{\tau jb})$ are sufficiently close to (m_W, m_t), the event is rejected.

The last requirement states that the invariant mass of two b-jets must be consistent with the Higgs boson decay, namely $90 < m_{bb} < 160$ GeV. The dijet mass m_{bb} is calculated from the two leading b-tagged jets if two $2b$-jets are identified in the event, or using also the untagged jet of the largest

four-momentum if only one jet in the event is b-tagged.

The final discriminant used to extract the signal in the non-resonant analysis is di-tau invariant mass $m_{\tau\tau}$. For the resonant search, the resonance mass $m_{bb\tau\tau}$, reconstructed from the bb and $\tau\tau$ system, is used as the discriminant. It is calculated using MMC prescription described above, with the scale factors applied to four-momenta of the dijet and ditau systems: m_h/m_{bb} and $m_h/m_{\tau\tau}$, respectively, to improve the mass resolution of the heavy resonance (m_h is the SM Higgs mass set to the value of 125 GeV).

For both the nonresonant and resonant searches signal selection is further optimised and the selected events are divided into four categories based on the ditau transverse momentum (less than or greater than 100 GeV) and the number of b-tagged jets (one or at least two). This optimisation was designed to benefit from different signal-to-background ratios in different kinematic regions.

For the nonresonant search, the observed $m_{\tau\tau}$ distribution does not show any excess of events with respect to the SM background prediction. For the resonant search, at $m_{bb\tau\tau} \simeq 300$ GeV a small deficit of events with a local significance of approximately two standard deviations is observed in the data relative to the estimated background events. No evidence of Higgs boson pair production is present in the data.

6.2.4 The $WW^*\gamma\gamma$ analysis

The $WW^*\gamma\gamma$ analysis aims at combining advantages offered on one hand by Higgs diphoton decays, with large branching ratio of the $h \to WW^*$ decays on the other. As demonstrated in Section 6.2.1, Higgs boson decays to two photons provide excellent reconstruction of the Higgs boson mass resulting in strong background suppression. In this analysis, one W boson is required to decay leptonically and the other hadronically.

Event selection follows closely the one in $hh \to bb\gamma\gamma$ in terms of requirements on the photons. The range of the diphoton mass considered here is somewhat broader, with $105 < m_{\gamma\gamma} < 160$ GeV. Signal region is defined as the diphoton mass window $m_{\gamma\gamma} \in [123.3, 126.7]$ GeV, the sideband region as $m_{\gamma\gamma} \in [105, 160]$ GeV excluding the signal region. The requirements related to the $h \to W^* \to l\nu jj$ decay are the presence of at least two jets, none of which are identified as b-jets, exactly one lepton and missing transverse energy E_T^{miss}. In order to distinguish if the momentum imbalance in the event originates from weak interactions (as is the case for the signal), or from reso-

lutions and inefficiencies of measuring particles' momenta in the detector the significance parameter [154] is used. Large values of this parameter indicate that observed E_T^{miss} originates from unobserved objects such as neutrinos or unknown weakly interacting particles. In this analysis significance of missing transverse energy must be greater than one.

The background processes are single Higgs boson production and continuum backgrounds, such as $W(\rightarrow l\nu)\gamma\gamma$ +jets processes. Events from single Higgs boson production can mimic the signal if, for example, the Higgs boson decays to two photons and other objects in the event are consistent with semileptonic $h \rightarrow WW^*$ decays. These events feature a diphoton mass peak at $m_{\gamma\gamma} = m_h$ and are therefore called resonant backgrounds. As in the $bb\tau\tau$ channel, contributions of these background processes are estimated from simulation. The background that is nonresonant in the diphoton mass, $m_{\gamma\gamma}$, spectrum is measured using the continuum background in the $m_{\gamma\gamma}$. The number of nonresonant background events in the signal region N_{SR} is estimated from the number of events in sidebands of the $m_{\gamma\gamma}$ in the data, N_{sb} using the formula: $N_{SR} = N_{sb}\frac{f_{sb}}{1-f_{sb}}$. The quantity f_{sb} is the fraction of background events in the range of diphoton masses $m_{\gamma\gamma} \in [105, 160]$ GeV, falling into the signal region $m_{\gamma\gamma} \in [123.3, 126.7]$ GeV. It is determined in a data control region, as shown in Figure 6.2a. The control region is constructed following requirements for the signal region without the requirements on the lepton and missing transverse energy. The estimation of signal and background in the signal region of the $\gamma\gamma WW^*$ analysis is shown in Figure 6.2b.

Within the range of di-photon invariant masses considered, 13 events are found, four of which are in the signal mass window. The expected number of events from single SM Higgs boson production and continuum background processes amounts to 1.65 ± 0.47. Due to the small number of events, event counts are used in both nonresonant and resonant searches. The background-only hypothesis corresponds to 1.8 standard deviations. For the resonant production, the expected numbers of events are 0.47 ± 0.05 and 0.72 ± 0.06 for a resonance mass of 300 GeV and 500 GeV, respectively.

6.3 Statistical combination procedure

In order to enhance the sensitivity of Higgs pair production cross-section measurement, the four channels are statistically combined. The compatibility of the background-only hypothesis with the observed data is measured

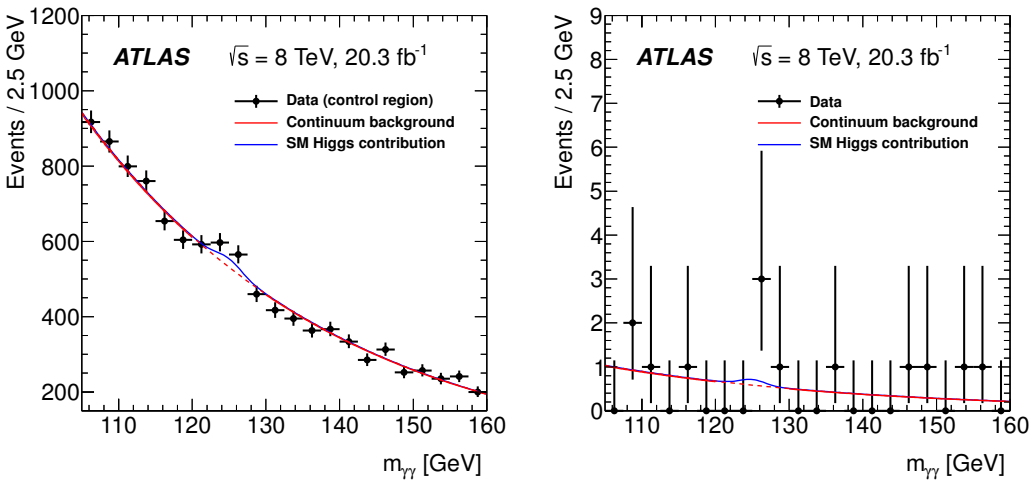

(a) (b)

Figure 6.2: The distribution of the diphoton invariant mass $m_{\gamma\gamma}$ for events passing (a) the control region selection and (b) the final signal selection. The red curves represent the continuum background contributions and the blue curves include the contributions from single SM Higgs boson. Details on estimation of these backgrounds are given in the text.

using Maximal Likelihood (ML) method with a test statistics based on profile likelihood ratio. Upper limits on the Higgs boson pair production cross section are derived using the CLs method [155].

Signal selection was chosen for each analysis in such a way as to ensure ortogonality of the phase spaces studied. In other words, selection criteria ensured that each event was classified in at most one signal category. There are systematic uncertainties that affect two or more analyses, for example: luminosity, jet energy scale and resolution, b-tagging, theoretical uncertainties on the single Higgs production process, etc. They are modeled with common nuisance parameters. Tables 6.1 and 6.2 indicate, what type of a signal discriminant is applied in each analysis in a search for a SM Higgs pair production and in BSM searches, respectively. In case of event yields, only uncertainties related to event rates are included. If the final discriminant is a kinematical distribution, shape uncertainties are additionally taken into account.

6.4 SM searches

Table 6.1 summarises signal discriminants used in all analyses as well as expected and observed cross-sections times branching ratios for the double Higgs production in gluon fusion for all four final states included in the combination. In case of $bbbb$ and $WW^*\gamma\gamma$ event yields are utilised in the fit. Given the small event yields in the latter and large resolution on the m_{bb} in the former, this proves to be the most sensitive choice. Likewise, $bb\gamma\gamma$ and $bb\tau\tau$ analyses use shapes of invariant masses of the Higgs boson that does not decay to a pair of b quarks, thus $m_{\gamma\gamma}$ and $m_{\tau\tau}$, respectively. The SM prediction for inclusive gluon fusion Higgs pair production cross-section is 9.9 ± 1.3 fb. Upper limits on the observed (expected) exclusive cross-sections relative to the SM are smallest in the $bbbb$ channel, in which it is equal to 63 (63), followed by upper limits obtained in the $bb\tau\tau$ and $bb\gamma\gamma$, which are equal to 160 (130) and 220 (100), respectively. The least stringent limits are obtained with the $WW^*\gamma\gamma$ channel and correspond to 1150 and 680 times the observed and expected SM cross-section. Large difference between observed and expected value of the cross section in the $bb\gamma\gamma$ channel is due to an excess of events in data with respect to predictions. The observed (expected) limits obtained in the combination exceeds by a factor 70 (48) the total SM cross section.

Table 6.1: Summary of signal discriminants used in all channels as well as expected and observed 95% CL upper limits on the cross-section for the SM Higgs pair production.

Final state	Discriminant	Upper limit on the cross-section [pb]	
		Expected	Observed
$bb\gamma\gamma$	$m_{\gamma\gamma}$	1.0	2.2
$bbbb$	event yields	0.62	0.62
$bb\tau\tau$	$m_{\tau\tau}$	1.3	1.6
$WW^*\gamma\gamma$	event yields	6.7	11
Combined		0.47	0.69

Leading systematical uncertainties are due to imperfect background modeling, b-tagging, theoretical predictions for Higgs boson decays and experimental measurements of jets and missing transverse energy and of luminosity. The large impact of uncertainties related to flavour tagging stems from large relative weight of the $bbbb$ final state in the combination.

6.5 Spin-0 searches

Higgs pair production can be enhanced with respect to the SM predicions due to a presence of a BSM scalar particle H, which decays to the pair of Higgs bosons h. This phenomenon is studied via a simplified model that contains the Higgs-like singlet H in addition to the SM Higgs doublet. Both H and h bosons obtain non-zero vacuum expectation values after electroweak symmetry breaking. In general, the cross-section values in this class of models depend on the mass of the heavy scalar, its vacuum expectation value relative to that of the Higgs ($\tan\beta = \frac{v}{v_H}$) and the mixing angle ϕ between the two bosons.[2] In the current studies, maximal values of the heavy scalar production cross-sections $pp \to H$ times its branching ratio to the SM Higgs boson $H \to hh$ for the given mass of the heavy scalar m_H are considered to obtain expected limits. Therefore, parameters $\tan\beta$ and ϕ may vary among various mass points. These values are based on recommendations presented in [2].

[2]Phenomenology of these models has been extensively studied in [49, 156–162].

Table 6.2: Summary of signal discriminants used in all channels as well as ranges of masses of the BSM scalar considered in each study.

Final state	Discriminant	Resonance mass range [GeV]
$bb\gamma\gamma$	event yields	[260, 500]
$bbbb$	m_{bbbb}	[500, 1500]
$bb\tau\tau$	$m_{bb\tau\tau}$	[260, 1000]
$WW^*\gamma\gamma$	event yields	[260, 500]

Table 6.2 lists distributions used in the signal extraction and range of masses m_H that are probed in each channel. In this search, distributions of reconstructed di-Higgs masses are used as fit inputs in the $bbbb$ and $bb\tau\tau$ searches, while the channels involving photons utilised event counts.

The 95% C.L. upper limits on the cross-section times branching ratio of this new particle of an unknown mass $m_H > 2m_h$ are displayed in Figure 6.3. They are obtained for all four channels mentioned above as well as their statistical combination. In the combination SM values for the decay branching ratios of the lighter Higgs boson h are assumed. The 1σ and 2σ uncertainty ranges of the expected combined limits are shown as green and yellow bands, respectively. Discontinuity of the limits around $m_H = 500$ GeV is due to the dominant sensitivity of the $bbbb$ analysis, that enters the combination above this value. The plot shows an excess of events at 300 GeV, that has a local significance of 2.5 σ. It is caused by the 3.0σ excess observed in the $bb\gamma\gamma$ channel, and attributed to a statistical fluctuation in data.[3] This upward fluctuation is consistent with an excess observed in the SM search.

Similarly to the nonresonant search, the systematic uncertainties with the largest impact on the sensitivity in the low mass range are related to the background modeling, b-tagging, jet and missing transverse energy measurements, and the SM Higgs boson decay branching ratios. In the larger mass range b-tagging uncertainty is by far most dominant, followed by uncertainties on the SM Higgs boson decay branching ratios, and jet/ missing transverse energy measurements.

[3]The fluctuation hypothesis was verified by performing several versions of the fit and inspecting events in the signal region. A subsequent study, using newly available first Run 2 data, has been undertaken and published in Ref. [163] Events have been analysed with similar selection requirements as above and no excess of events has been found.

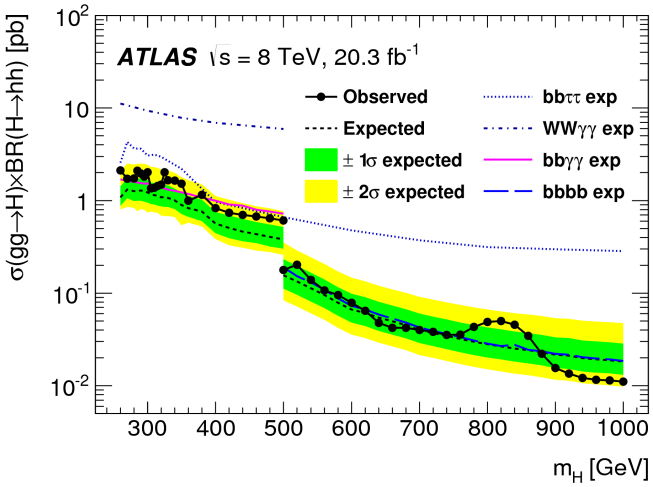

Figure 6.3: Upper limits on the cross-section times branching ratio of a heavy scalar resonance H decaying into a pair of Higgs bosons. Results are obtained with the statistical combination of the channels using 8 TeV dataset in ATLAS. Details are given in the text.

6.5.1 Comparison with CMS

The comparison of ATLAS and CMS searches for a spin-0 BSM scalar are shown in Fig. 6.4. using integrated luminosities of $17.9 - 20.3$ fb^{-1}. This comparison was performed by overlaying results published by both experiments. It was intended for a qualitative comparison of observed and upper limits and features therefore no uncertrainties bands. In this plot, the mass of a heavy scalar is denoted as $m_X^{\text{spin-0}}$, following CMS conventions. In the CMS searches three final states are utilised: $bb\gamma\gamma$ [139, 142], $bbbb$ [140, 141] as well as $bb\tau\tau$ [143, 164, 165]. 95% C.L. upper limits obtained in these channels are displayed in Fig. 6.4 in red, khaki and magenta lines, respectively. Dashed lines correspond to expected and solid lines to observed limits. The results of statistical combination of ATLAS results discussed above is shown in navy-blue lines.

In both ATLAS and CMS searches the most sensitive channel at low resonance mass, below 350 GeV, is $bb\gamma\gamma$. Its sensitivity benefits from a good trigger and reconstruction efficiency and low background. In contrast, above 500 GeV the most sensitive channel is $b\bar{b}b\bar{b}$. At high mass of the heavy scalar

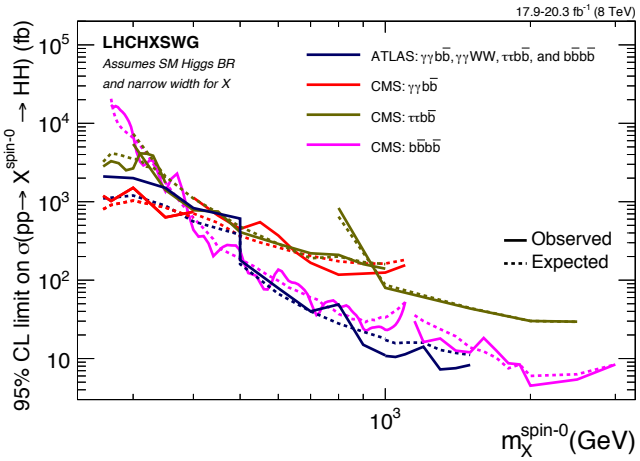

Figure 6.4: Limits on the searches of a heavy scalar resonance decaying into the pair of Higgs bosons in the 8 TeV dataset in ATLAS and CMS. In case of ATLAS a combined result of several searches is shown, whereas CMS results in various final states are displayed independently. Figure from Ref. [2].

the branching fraction of this channel and experimental techniques of reconstructing highly boosted b-jets provide a decisive advantage. CMS has demonstrated that its search range can be extended to 3 TeV, way above 1.5 TeV investigated by ATLAS. The properties of the $bb\tau\tau$ channel with the state-of-the-art analysis methods offer good sensitivity in the intermediate mass range. It can also be seen, that expected limits of the ATLAS search at low resonance mass coincide with (both expected and observed) CMS limits in the $bb\gamma\gamma$ channel. Observed ATLAS limits are less stringent, due to an observed excess of signal events in the $bb\gamma\gamma$ final state, discussed earlier. Discontinuities of the limits are caused by different analysis techniques adopted in various mass ranges.

6.6 Summary

This Chapter presents Higgs pair searchers that have been performed by the ATLAS experiment at Run 1 and their statistical combination. These studies utilised 20 fb^{-1} of data at a center-of-mass energy of 8 TeV of colliding protons. Four decay channels have been used: $bbbb$, $bb\gamma\gamma$, $bb\tau\tau$, and $WW^*\gamma\gamma$.

Reconstruction techniques applied in all of them have been outlined. The analysis featuring four b quarks in the final state reconstructs and identifies separate b-quark jets from the low-momentum Higgs boson decays and identifies the boosted $h \to bb$ decay reconstructed as a single jet using jet substructure techniques. The $bb\gamma\gamma$ study reconstructs one Higgs boson from two energetic isolated photons with diphoton invariant mass compatible with m_h and the other one from two jets identified as b-jets within a (broader) di-jet mass window. The $bb\tau\tau$ final state uses events with one τ lepton decaying leptonically and the other one hadronically and divides them into four categories based on the di-τ transverse momentum (less than or greater than 100 GeV) and the number of identified b-jets ("1" or "2 or 3"). The $WW\gamma\gamma$ analysis reconstructs one Higgs boson from its decays to a pair of photons and the other one from semi-leptonic decays of the WW^*. It vetoes events featuring b-jets.

Statistical combination of all four channels has been performed. In the SM (non-resonant) study, event yields in $bbbb$ and $WW\gamma\gamma$ final states and the invariant mass of two photons and two τ leptons in $bb\gamma\gamma$ and $bb\tau\tau$, respectively have been used in the final discriminant. In the search for a heavy resonance, the distributions of invariant masses $m_{bb\tau\tau}$ and m_{bbbb} have been used in two channels with largest number of events, while in final states with photons event counts have been utilised in the fit. The combination results in a 95% C.L. upper limit of 0.69 pb on the observed cross section of the non-resonant Higgs boson pair production, while the expected limit is 0.47 pb. The observed upper limit is approximately 70 times larger than the cross section for Higgs pair production through gluon fusion in the SM. The data has been interpreted in selected BSM scenarios. One of them, predicting largest enhancement of Higgs pair producion cross-section with respect to the SM, is the production of a heavy scalar resonance decaying to a pair of SM Higgs bosons. In this scenario the observed (expected) upper limit on production cross-section times branching ratio varies from 2.1 (1.1) pb at the heavy resonance mass of 260 GeV to 0.011 (0.018) pb at the mass of 1000 GeV. These limits are obtained under the assumption that the Higgs boson decay branching ratios do not deviate from the SM.

The upper limits for cross-section times branching ratio of a heavy BSM scalar decaying to a pair of Higgs bosons obtained by ATLAS has been compared with corresponding limits extracted by CMS experiment. It provides some insight into domains of possible improvements of experimental techniques of both experiments and demonstrates the role of statistical combina-

tion in maximising sensitivity.

The examples of analyses improvements undertaken in studies using Run 2 data are given in the next Chapter. In particular, developments in the τ reconstruction and machine learning methods in Run 2 increase this channel sensitivity to low di-Higgs masses, making its sensitivity competitive with $b\bar{b}\gamma\gamma$.

7 Combination of Higgs pair searches with the Run 2 data

This chapter describes a combination of searches of Higgs boson pair production using up to 36 fb^{-1} of data collected at centre of mass energy of colliding protons equal to $\sqrt{s} = 13$ TeV by the ATLAS experiment. Six channels are selected for Run 2 Higgs pair searches: $bbbb$ [166], bbW^+W^- [167], $bb\tau\tau$ [168], $W^+W^-W^+W^-$ [169], $bb\gamma\gamma$ [163] and $W^+W^-\gamma\gamma$ [170]. In this way, more phase space regions are investigated than in Run 1 described in the previous chapter. Other advantage with respect to the previous studies lies in the increase of expected signal event yields. This is due to larger predicted cross-section through gluon fusion from $\simeq$7 fb to $\simeq$10 fb [2] with the increase of centre of mass energy from 8 to 13 TeV on one hand and almost a factor of 2 increase of integrated luminosity on the other.

In this dataset SM Higgs pair production has been searched for, together with several BSM models predicting enhancement of the cross-section. A non-resonant model with anomalous Higgs boson self-coupling modifier $\kappa_\lambda \equiv \frac{\lambda_{3h}^{BSM}}{\lambda_{3h}}$ is investigated under the assumption that all other Higgs boson couplings have their SM values. Resonant models involving a new heavy particle decaying into a pair of Higgs bosons studied in this analysis include both generic BSM extensions of the SM featuring an additional scalar or a spin-2 particle that decays into a pair of Higgs bosons and more specific theories. Among the specific models probed, Ref. [171] summarises searches within the two-Higgs-Doublet Model [53], Minimal Supersymmetric Standard Model (MSSM) [50–52], and Electroweak Singlet Models (EWK-singlet) [49, 159–162].

The predictions of these BSM models are expressed in multi-dimensional parameter spaces. For example, in the EWK-singlet model, a mixing angle α between the Higgs boson and the additional scalar as well as the ratio of the

vacuum expectation values of the two, $\tan\beta$ are free parameters determining cross-section predictions. Instead of constraining intricate models, the predictions offering largest cross-section enhancements with respect to the SM have been chosen to study, as summarised in [2].

In this Chapter I restrict myself to summarising the measurements interpretations in terms of generic models, because they give a good view of the sensitivity of different channels and their combination to the SM and its extensions. Analyses strategies in each channel are optimised for different searches and are presented in the corresponding section.

The statistical combination procedure follows the Run 1 combination described in Chapter 6 and can be briefly summarised in the following: The CLs approach [155] for determining exclusion intervals is applied and asymptotic formulae of likelihood-based tests [92] are used. The orthogonality of signal regions is ensured by harmonised event selection with the exception of the $bb\gamma\gamma$ signal regions which have negligible overlap. The combination results are obtained using a fit to the data in all signal regions. The fit simultaneously constraints the signal cross-section as well as systematical and statistical uncertainties parametrised with nuissance parameters. Experimental systematical uncertainties and uncertainties related to the signal acceptance are correlated across all channels. Theoretical and modelling systematic uncertainties of the backgrounds, on the other hand, are not correlated across different final states because the overlap among background processes to the different searches is negligible. The impact of each systematic uncertainty on the obtained limit has been evaluated by recomputing the limits without the inclusion of this uncertainty.

This Chapter is based on the publication of Ref. [171].

7.1 Upper limits on the SM di-Higgs production cross-section

Signal samples are generated using Madgraph5_aMC@NLO [65] matrix element (ME) with CT10 NLO parton distribution function (PDF) set [145] and Herwig++ [172] Parton Shower with hadronisation simulated with the UE-EE-5-CTEQ6L1 tune [173] set of parameters. Matrix element includes partial effects of the finite top quark mass in the real-radiation NLO corrections [144], while the virtual-loop corrections are computed using Higgs

effective field theory (HEFT) with infinite top quark mass.

In order to obtain kinematical distributions that are not affected by the HEFT approximation, the generated events are then corrected with a generator level bin-by-bin reweighting of the di-Higgs invariant mass distribution, calculated at NLO with finite top-quark mass [121]. The theoretical uncertainties of the SM signal cross-section are estimated to be less than 10% [2] and are neglected in the statistical analysis.

The cross-section measurement is performed in the kinematical region, where energy of the two Higgses is close to their threshold. Since neither of the Higgs boson is boosted, their decay products are expected to be well separated from each other. Jets are reconstructed using anti-k_t algorithm [83] with a radius parameter R = 0.4.

The *bbbb* analysis selects events, in which four anti-k_t jets are reconstructed with a radius parameter R = 0.4. This is called a "resolved" selection. This channel internally statistically combines different datasets from 2015 and 2016 as they use different b-jet trigger algorithms. In the final limit-setting fit the distribution of invariant di-Higgs mass, m_{HH}, is used.

The $bbWW^*$ analysis selects semileptonic decays of the WW^* pair. Therefore, a light lepton (electron and muon) and four jets (two of them being b-jets) are expected in the event, together with missing energy due to a neutrino. In the SM analysis all jets are reconstructed with a radius parameter $R = 0.4$ using anti-k_t algorithm. The number of events in the signal region is used as the final discriminant in the fit.

In the WW^*WW^* study three channels are defined, depending on decay products of the W bosons: fully leptonic and semi-leptonic with either two or four jets resulting from hadronic decays of one or two W bosons, respectively. This analysis identifies in total nine signal categories depending on the number and relative flavours of leptons. Dilepton events are required to have two leptons of the same charge, either two electrons or two muons (2 signal categories). Three-lepton events are selected if the sum of the lepton charges is ± 1. They are further subdivided into three signal categories based on the number of same-flavour, opposite-charge lepton pairs in the event being 0, 1, or 2. Four-lepton events are divided into four categories according to the number of same-flavour, opposite-charge lepton pairs and the invariant mass (m_{4l}) of the four-lepton system. The number of same-flavour, opposite-charge lepton pairs is required to be less than two or equal to two, and m_{4l} is smaller or larger than 180 GeV.

The $WW^*\gamma\gamma$ analysis selects events in which one W boson decays lep-

tonically and a second one decays hadronically. Jets from hadronic W decay are reconstructed using anti-k_t algorithm with a radius R = 0.4. Only one category is used in all the searches, with $m_{\gamma\gamma}$ being the final discriminant.

The $bb\gamma\gamma$ analysis searches utilises two event selections: A "loose selection", used in the κ_λ study, requires two energetic jets with transverse momenta larger than 40 GeV and 25 GeV, respectively. A "tight selection", adopted in the SM HH search, demands that transverse momenta of jets are larger than 100 and 30 GeV. All jets have a radius parameter R = 0.4. Both selections are subdivided into two categories requiring one b-tagged jet or two b-tagged jets. Both these categories in their respective selection are used to obtain each fit result.

The $bb\tau\tau$ analysis selects events with two τ leptons and two jets with a radius of R = 0.4, which are b-tagged. One of the two τ leptons is required to decay hadronically. Events are categorised according to the decays of the other τ lepton into di-hadronic ($\tau_{had}\tau_{had}$) and semi-leptonic ($\tau_{lep}\tau_{had}$) final states. In the $\tau_{lep}\tau_{had}$ channel, events are triggered by single lepton triggers (SLT), requiring an electron or a muon in the final state, or by the coincidence of a lepton trigger with a hadronic τ trigger (LTT). In the $\tau_{had}\tau_{had}$ channel, events are triggered by single hadronic τ triggers (STT) or double hadronic τ triggers (DTT). The analysis is divided into three categories depending on the trigger combination. In order to improve the separation of signal from background multivariate techniques (BDTs) are used. BDTs are constructed and trained in each category individually. In the $\tau_{had}\tau_{had}$ channel they are trained against the largest backgrounds: top quark pairs, $Z \to \tau\tau$ and multi-jet events. In the $\tau_{lep}\tau_{had}$ channel the training against the dominant top quark pair background is performed. Variables used as inputs to the BDTs for the three channels differ due to differences in background composition. In all three channels variables related to the properties of the di-Higgs final state, such as: invariant mass of the di-Higgs system, approximate di-τ mass, invariant mass of two b-jets, and radial separation ΔR between two τs and two b-jets provide good discrimination against backgrounds. The three regions are statistically combined with the BDT score distributions in the signal regions together with event yields in the control regions being the input for the fit.

The upper limits at 95% CL on the measured cross-section of the Higgs boson pair production $\sigma_{ggF}(pp \to hh)$ resulting from individual and combined fits are normalised to the SM ggF cross-section σ^{SM}_{ggF}. They are shown in Fig. 7.1: the upper limits for individual final states are shown above the

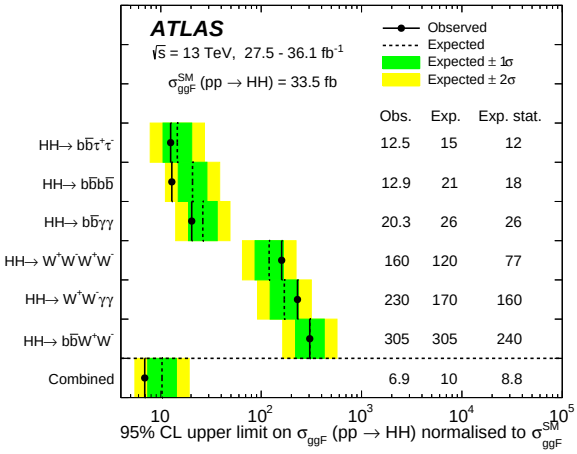

Figure 7.1: Upper limits at 95% CL on the cross-section of the SM HH production normalised to its ggF SM expectation.

dashed line and the upper limits of their combination below it. Numerical values of the limits in individual channels and their combination are listed in columns on the right hand side of Fig. 7.1. In the column labeled "Obs" limits resulting from data are given. The expected limits are given in two statistical models: the one in which all systematical and statistical uncertainties are taken into account (the column labelled "Exp.") and the one including only statistical uncertainties ("Exp. stat."). The three most sensitive channels are $bbbb$, $bb\tau\tau$, and $bb\gamma\gamma$, with limits on the SM cross-section more stringent by a factor of $\sim$10 with respect to the channels that include WW^* in the final state.

The combined observed upper limit on the di-Higgs production cross-section is 6.9 times larger than its predicted SM value, while the expected upper limit is 10 times larger. This discrepancy, still within the 2σ uncertainty interval, is a result of an observed deficit of events in this dataset. The main sources of systematic uncertainty are related to the modelling of the backgrounds, the statistical uncertainty of simulated events and the τ reconstruction and identification.

7.2 Constrains on the Higgs boson self-coupling

The three final states which are most sensitive to the SM di-Higgs production cross-section are selected to set constraints on the Higgs boson self-coupling modifier κ_λ. The fit is performed under the assumption that all other Higgs couplings have their SM values.

To make predictions for any value of κ_λ only three LO MC samples with different values of κ_λ are generated. All other values are obtained as linear combinations of these three samples. Binned ratios of m_{HH} (the generated (BSM) di-Higgs invariant mass distributions) to the SM distribution are computed for all values of κ_λ using the leading-order matrix elements generated by (LO) MadGraph5_aMC@NLO [65] with PYTHIA 8.2 [174] parton shower, using the A14 tune [68] and the NNPDF 2.3 LO [175] PDF set. These distributions are then used to reweight the SM di-Higgs signal events generated at NLO using the full detector simulation. This procedure is validated by comparing kinematic distributions obtained with the reweighting procedure and LO samples generated with their corresponding κ_λ values set explicitly in the LO event generator. The two sets of distributions are found to be in agreement.[1] The reweighted NLO signal sample is used to compute the signal acceptance and the kinematic distributions for different values of κ_λ.

The dependence of the shape of m_{HH} distributionon on κ_λ is illustrated in Figure 7.2 for generator-level $pp \to hh$ events. Both the normalisation and shape of m_{HH} are strongly dependent on the interference between the box and the triangle diagrams, as discussed in Chapter 4. For $\kappa_\lambda = 0$ only the (dominant) box contribution is present and the cross-section is larger than in the SM. The m_{HH} distributionon in this case has a peak at the threshold $\simeq 2m_t$ production. For large positive values of κ_λ, such as 5 or 10, the triangle diagram dominates the cross-section, therefore the distribution peaks at the $2m_H$ threshold. For $\kappa_\lambda \simeq 2$ almost maximum destructive interference between the box and the triangle diagrams takes place, resulting in a deficit of events betwen m_H and $2m_t$. This deficit is more pronounced for $\kappa_\lambda = 5$ making the m_{HH} distribution narrower than in the $\kappa_\lambda = 10$ case. In case of negative values of the Higgs self-coupling the interference is constructive, leading to the overall growth of the cross-section. Peaks characterictic of

[1] This procedure assumes that higher order QCD corrections on the differential cross-section $d\sigma/dm_{HH}$ are independent of κ_λ and that higher order electroweak corrections are negligible.

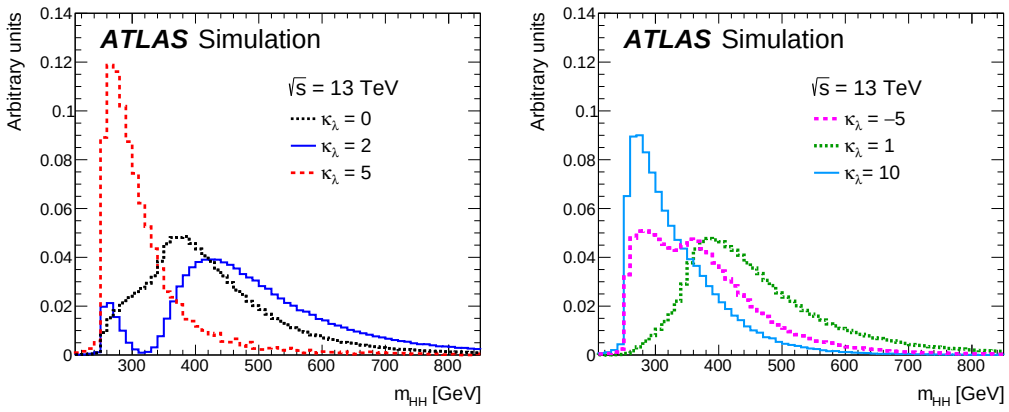

Figure 7.2: Generator-level m_{HH} distributions computed for selected values of κ_λ: 0, 2, 5 in (a), and -5, 1, 10 in (b).

threshold production in both channels are present, yet smaller relative to cases with destructive interference.

In the $bb\gamma\gamma$ study, the "loose" jet selection is used in the κ_λ scan. Similarly to the SM HH search, the di-photon invariant mass $m_{\gamma\gamma}$ distribution is used in the statistical analysis. This distribution, related to a single Higgs boson and not to the Higgs pair, is independent of the boson's self-coupling. The sensitivity of this analysis to κ_λ parameter is due to the signal acceptance, which varies by about 30% over the probed range of values as shown in Figure 7.3. With respect to the analysis publication [42], the combination improves the computation od the signal acceptance in this channel by using the NLO reweighted samples instead of LO ones.

The analysis selection in the *bbbb* channel closely follows the SM analysis described above. The final discriminant used in the κ_λ analysis is the di-Higgs mass m_{HH}, displayed in Fig. 7.4 (a). The background processes in the *bbbb* analysis include multi-jet processes (Multijet), estimated with data-driven techniques, top quark pairs, in which decays both W bosons decay hadronically (Hadronic $t\bar{t}$), top quark pairs with at least one of the W bosons decaying leptonically (Semileptonic $t\bar{t}$). A good agreement between data and the expected background is observed with the exception of a small excess in the region around 280 GeV. Figures 7.3 and 7.4 (a) demonstrate that both the shape of the m_{HH} distribution and the signal acceptance strongly depend on κ_λ. The exclusion limits on the cross-section as a function of κ_λ is therefore

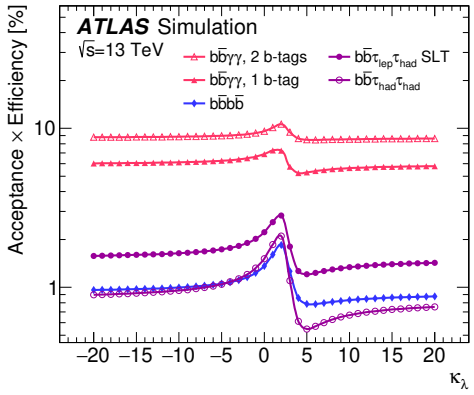

Figure 7.3: Signal acceptance times efficiency as a function of κ_λ for all individual channels: $bb\gamma\gamma$, $bbbb$, and $bb\tau\tau$.

determined by the interplay of these effects.

The $bb\tau\tau$ analysis uses both semileptonic, $\tau_{lep}\tau_{had}$, and fully hadronic, $\tau_{had}\tau_{had}$, final states. The former uses only events that pass the single lepton trigger (SLT), while the events that pass the (LTT) trigger (requiring the coincidence of a lepton trigger with a hadronic τ trigger) are not included due to their negligible contribution. The main backgrounds in the $bb\tau\tau$ channels are: double and single top quark production (Top-quark), the background originating from jets misreconstructed as hadronic τ decays (jet $\rightarrow \tau_{had}$ fakes), backgrounds arising from taonic decays of a Z boson, accompanied by two heavy-flavour jets ($Z \rightarrow \tau\tau + (bb, bc, cc)$), SM single Higgs boson production (SM Higgs) and other smaller backgrounds (Other). The κ_λ analysis uses the same sets of variables to build BDT discriminants as the SM one described above with the BDTs retrained using the NLO SM signal sample reweighted with $\kappa_\lambda = 20$. The BDT score distributions, presented in Fig. 7.4 (b) and (c), for the $\tau_{had}\tau_{lep}$ and $\tau_{had}\tau_{had}$ channels, respectively, are used in the fit to compute the final results. The shape of the BDT distributions does not depend on κ_λ as strongly as in case of the $bbbb$ final state. The sensitivity of this analysis is instead affected by a variation in the signal acceptance, that varies by up to a factor of three over the probed range of κ_λ values, as shown in Figure 7.3.

The 95% CL allowed κ_λ intervals are given in Table 7.1. Limits resulting from data in individual channels and their combination are listed in the

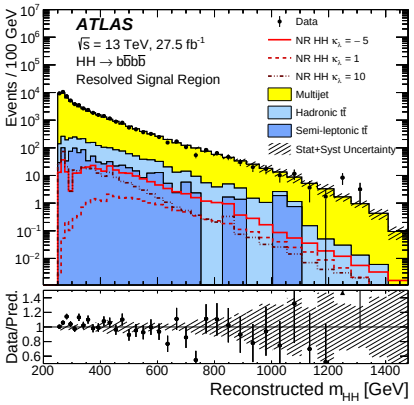

(a) The reconstructed m_{HH} distribution in the *bbbb* analysis

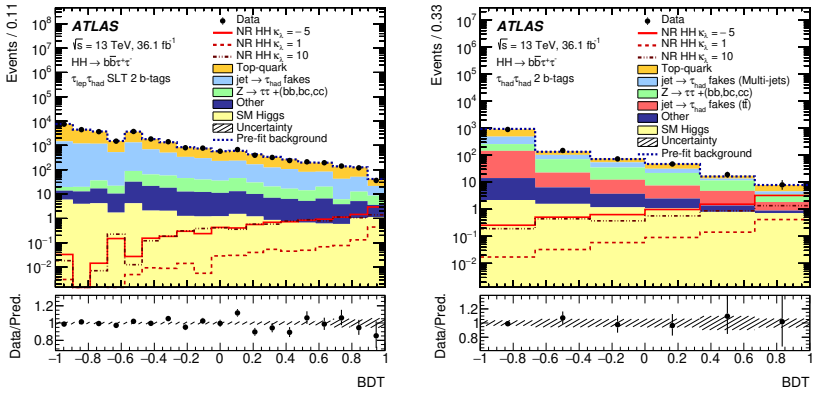

(b) The BDT distribution in the $bb\tau\tau$ $\tau_{lep}\tau_{had}$ analysis

(c) The BDT distribution in the $bb\tau\tau$ $\tau_{had}\tau_{had}$ analysis

Figure 7.4: Final discriminants used in the κ_λ analysis for the *bbbb* (a) and the $bb\tau\tau$ channels (b) and (c). The shaded area represent the uncertainty on the total background expectation, including: the statistical uncertainty of the simulated samples and all experimental and theoretical systematic uncertainties. The signal distribution is overlaid for selected values of κ_λ parameter (including the SM value of 1) and is normalised to the expected yield.

Table 7.1: Allowed κ_λ intervals at 95% CL for the $bbbb$, $bb\tau\tau$, $bb\gamma\gamma$ final states and their combination.

	Allowed κ_λ intervals at 95% CL		
Final state	Obs.	Exp.	Exp. stat. only
$bbbb$	$[-10.9, 20.1]$	$[-11.6, 18.8]$	$[-9.8, 16.3]$
$bb\tau\tau$	$[-7.4, 15.7]$	$[-8.9, 16.8]$	$[-7.8, 15.5]$
$bb\gamma\gamma$	$[-8.1, 13.1]$	$[-8.1, 13.1]$	$[7.9, 12.9]$
Combined	$[-5.0, 12.0]$	$[-5.8, 12.0]$	$[-5.3, 11.5]$

column labeled "Obs". Like before, the expected limits are given in two statistical models: the one in which all systematical and statistical uncertainties are taken into account (the column labelled "Exp.") and the one including only statistical uncertainties ("Exp. stat."). The statistical uncertainties related to the smallness of expected signal yields are the dominating sources of uncertainties in all three analyses and in their combination. The inclusion of systematic uncertainties weakens the κ_λ limits by less than 10%. The final state, in which systematic uncertainties have the relative smallest impact on the limits is the $bb\gamma\gamma$ one, while the final state most affected by systematic uncertainties is $bbbb$.

Fig. 7.5 illustrates, how these limits are obtained by presenting the dependence of Higgs pair production cross-section on κ_λ values in the probed range of $[-20, 20]$. The observed (expected) 95% CL upper limits are shown as solid (dashed) lines. The lines coresponding to individual channels are shown without error bands, while the $\pm 1\sigma$ and $\pm 2\sigma$ uncertainty bands are only given for their combination. They are overlayed with theory prediction for the cross-section as a function of κ_λ.

As a result of statistical combination, κ_λ values outside the range $-5.0 \leq \kappa_\lambda \leq 12.0$ are excluded at 95% confidence level. This limit is already competitive with respect to the one obtained in HL-LHC feasibility study, outlined in Chapter 8, despite $\sim$30 times smaller statistics. The improvements stem predominantly from better reconstruction techniques of photons and b-quarks, as well as combination of three channels with maximal sensitivities to slightly different regions of κ_λ.

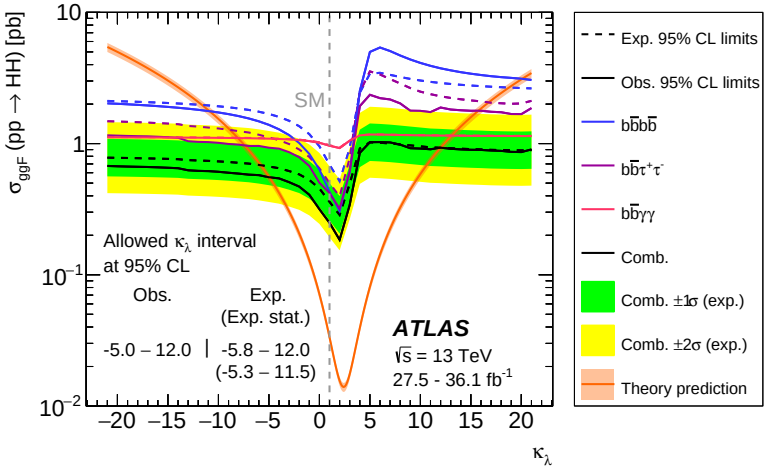

Figure 7.5: Upper limits at 95% CL on the cross-section of the ggF SM Higgs pair production as a function of κ_λ in individual channels and their combination. The observed (expected) limits are displayed as solid (dashed) lines. In the $bb\gamma\gamma$ final state, the observed and expected limits coincide. The $\pm1\sigma$ and $\pm2\sigma$ uncertainty bands (green and yellow, respectively) are only shown for the combined expected limit. The theoretical prediction of the cross-section as a function of κ_λ is also shown.

7.3 Upper limits for resonant BSM Higgs pair production

These searches are performed in the BSM particle mass range of 260–3000 GeV.

The search for the heavy spin-0 particle decaying to a pair of Higgs bosons is performed using all six di-Higgs final states. With the exception of $bb\tau\tau$ and *bbbb*, all signal samples are simulated at NLO with MadGraph5_aMC@NLO using the CT10 PDF set. The matrix-element generator is interfaced to HERWIG++ with the UE-EE-5-CTEQ6L1 tune. The $bb\tau\tau$ and the *bbbb* final states use both LO ME generated with MadGraph5_aMC@NLO. In the former the NNPDF 2.3 LO PDF set interfaced to PYTHIA 8.2 with the A14 tune is used, while in the latter ME are interfaced to HERWIG++ with the UE-EE-5-CTEQ6L1 tune.

Fig. 7.6 (a) shows the upper limits at 95% CL on the resonant BSM Higgs pair production cross-section as a function of the resonance mass m_S. Upper limits obtained from individual channels are marked by lines of various colours, while the combined result is marked by a black line with green and yellow bands, corresponding to 1σ and 2σ uncertainty. The vertical black lines in each pannel indicate mass intervals where different final states are combined. The $WW^*\gamma\gamma$ and WW^*WW^* channels are included only in the range of small resonance masses, $260 - 500$ GeV, $bb\tau\tau$ and $bb\gamma\gamma$ in the small and intermediate $m_S < 1$ TeV, $bbWW^*$ in the intermadiate and large masses, from 500 GeV to 3 TeV. The *bbbb* channel covers the full range. No statistically significant excess is observed within the mass range of $260 - 3000$ GeV. In the range of small m_S the most sensitive channel is $bb\gamma\gamma$. In the intermediate mass range, from 500 GeV to 1 TeV, the sensitivity of the combination is influenced mainly due to three channels: *bbbb*, $bb\tau\tau$ and $bb\gamma\gamma$. In the mass range above 1 TeV the *bbbb* channel is the most sensitive. Systematic uncertainties have a sizeable effect on the upper limits depending on the probed resonance mass.

Overall the systematic uncertaintes affect the limit by 12% (11%) for a resonance mass of 1 (3) TeV. The largest systematic uncertainties at 1 TeV are due to the modelling of the backgrounds and b-tagging. They impact the upper limit by 7% and 2%, respectively. At 3 TeV, modelling of the backgrounds changes the upper limit by 9%, while the impact of jet resolution and energy scale is 2%.

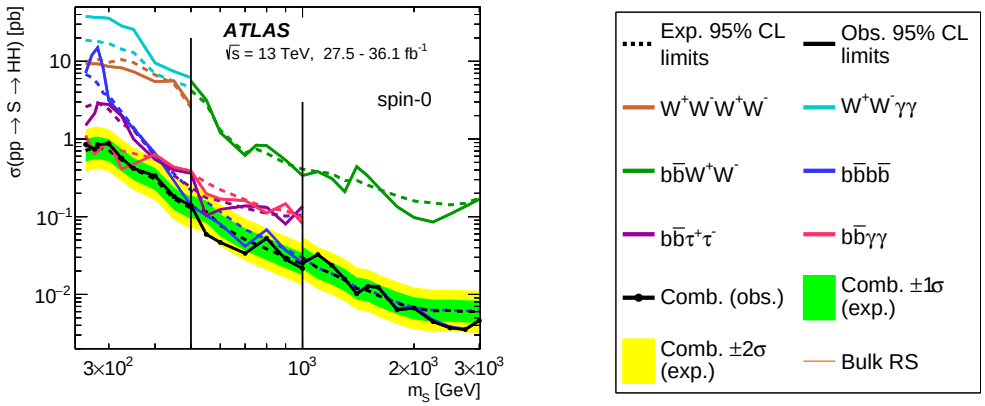

(a) Spin-0 search

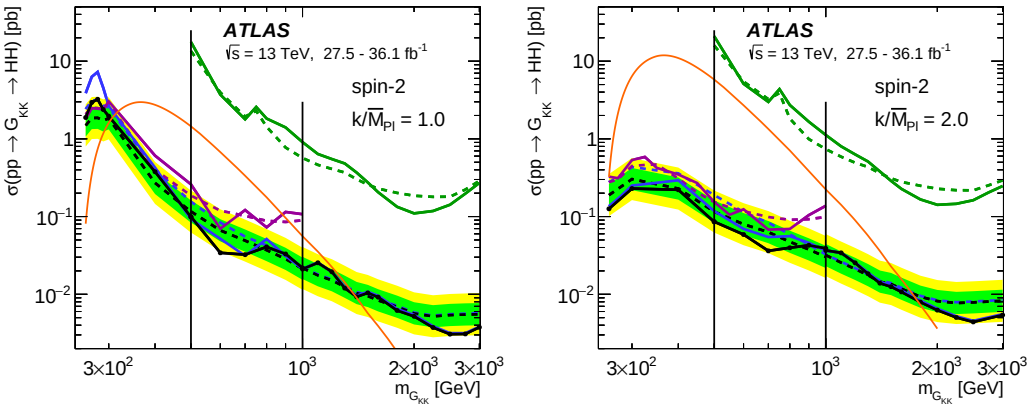

(b) spin-2 KK graviton, $k/\overline{M}_{Pl} = 1$

(c) spin-2 KK graviton, $k/\overline{M}_{Pl} = 2$

Figure 7.6: Upper limits at 95% CL on the cross-section of the resonant Higgs boson pair production for a spin-0 scalar (a), a spin-2 KK graviton with $k/\overline{M}_{Pl} = 1$ (b) and with $k/\overline{M}_{Pl} = 2$ (c) as a function of the heavy particle's mass m_S and $m_{G_{KK}}$. The observed (expected) limits are shown as solid (dashed) lines. The ±1 and ±2 bands are only shown for the expected limits of the combination.

The searches for the spin-2 boson are inspired by the Randall–Sundrum (RS) model of warped extra dimensions [176] that predicts a new spin-2 Kaluza–Klein (KK) graviton, that can decay to the Higgs boson pairs. Contrary to the spin-0 singlet, the width of the graviton changes with its mass, $m_{G_{KK}}$, and depends on the parameter $k/\overline{M_{Pl}}$, where k denotes the curvature of the warped extra dimension in the bulk RS model and $\overline{M_{Pl}}$ is the effective four-dimensional Planck mass, whose numerical value is $\overline{M_{Pl}} = 2.4 \times 10^{18}$ GeV. The search is performed for models with $k/\overline{M_{Pl}}$ equal to 1 and 2. For $k/\overline{M_{Pl}} = 1$, the graviton's width ranges from 3% for $m_{G_{KK}} = 0.3$ TeV to 6% for $m_{G_{KK}} = 3$ TeV, while for $k/\overline{M_{Pl}} = 2$ the corresponding ranges are from 11% to 25%. This model is investigated using three channels: $bbbb$, bbW^+W^-, $bb\tau\tau$ because they offer best sensitivity in the relevant range of masses.

Gravitons are simulated using an LO model in MadGraph5_aMC@NLO with the NNPDF 2.3 LO PDF set interfaced to Pythia 8.2 with the A14 tune. The upper limits in the KK graviton search are shown as a function of its mass in Figures 7.6b and 7.6c for $k/\overline{M_{Pl}}$ equal to 1 and 2, respectively. Again, the uncertainty bands are shown only for the combined result. The largest observed deviation from the background-only expectation in the combined search have sensitivities below 2σ. Theory predictions at the Leading Order are overlaid with an orange line in both plots. Exclusion ranges on the KK graviton mass are obtained by comparing the upper limit with the predicted cross section. In the case of $k/\overline{M_{Pl}} = 1$, the bulk RS model is excluded at 95% CL in the graviton mass range from 310 GeV to 1380 GeV. In the case of $k/\overline{M_{Pl}} = 2$, the model is excluded at 95% CL for graviton masses from 260 GeV, where the scan starts, to 1760 GeV.

The impact of the systematic uncertainties on the upper limits amounts to ∼20% for $k/\overline{M_{Pl}} = 1$. In the case of $k/\overline{M_{Pl}} = 2$, it ranges from 25% to 29% between $m_{G_{KK}}$ ranging from 3 TeV to 1 TeV. The largest systematic uncertainties are from the modelling of the backgrounds (affecting the limit by ∼15%). For $k/\overline{M_{Pl}} = 1$ other large sources of systematic uncertainties are due to b-tagging, largest at low graviton mass, and affecting the limit by 3%, and from jet energy scale and resolution at high mass, that affect the upper limit by $2\% - 3\%$. For $k/\overline{M_{Pl}} = 2$, jet energy scale and resolution impacts the upper limits by $4\% - 5\%$. The systematic uncertainties affect upper limits more for $k/\overline{M_{Pl}}= 2$, due to the width of the signal graviton, which is four times larger in case $k/\overline{M_{Pl}} = 2$ than $k/\overline{M_{Pl}} =1$.

7.4 Constraining the electroweak singlet model

The experimental limits on the cross-section for a spin-0 resonance production, discussed in the previous section, can be interpreted as constraints in the electroweak singlet (EWKS) parameter planes. To do so, the expected values of cross-section for each point in the parameter space is obtained by scaling the prediction for heavy scalar production cross-section at NNLO+NNLL from Ref. [2] with singlet coupling modifiers and branching fractions computed with sHDECAY [177].

Figure 7.7 summarises exclusion limits for the EWKS model in two parameter planes. Figures 7.7a and 7.7b show $(m_S, \sin\alpha)$ planes for $\tan\beta = 1$ and $\tan\beta = 2$, respectively. The EWKS model predicts that the width of a resonance with large m_S can be sizeable. Therefore, results presented here and obtained using a narrow width assumption are valid only in regions of the parameter space where the resonance width, Γ_S, is smaller than the experimental resolution at the resonance mass m_S: $\Gamma_S/m_S < 2\%$ for $bb\gamma\gamma$, $\Gamma_S/m_S < 5\%$ for $bbbb$ and $\Gamma_S/m_S < 10\%$ for $bb\tau\tau$. The dotted lines in Figures 7.7a and 7.7b indicate the separation between regions where the resonance width is larger than 2% and 5% of the resonance mass and the hatch-marked regions include points where $\Gamma_S/m_S > 10\%$ and no exclusion may be provided with the current analysis setup. Figure 7.7c shows limits in the $(\sin\alpha, \tan\beta)$ parameter space obtained for relatively low mass of the EWKS, $m_S = 260$ GeV, for which narrow width is a good approximation and the three searchers can be straightforwardly combined. The indirect contraints on $|\sin\alpha|$, originating from SM Higgs coupling measurements [178], are also shown, as green horizontal and vertical lines.

The exclusion limits obtained with double Higgs searches improve over the single Higgs results in regions of parameter space where $\tan\beta$ is large and the mass of the singlet is intermediate.

7.5 Summary

This Chapter presents searches for Higgs boson pair production using six final states: $bbbb$, bbW^+W^-, $bb\tau\tau$, $W^+W^-W^+W^-$, $bb\gamma\gamma$ and $W^+W^-\gamma\gamma$ and their statistical combination. They utilise 36.1 fb^{-1} of proton–proton collision data at 13 TeV recorded with the ATLAS detector during years 2015 and 2016 of Run 2.

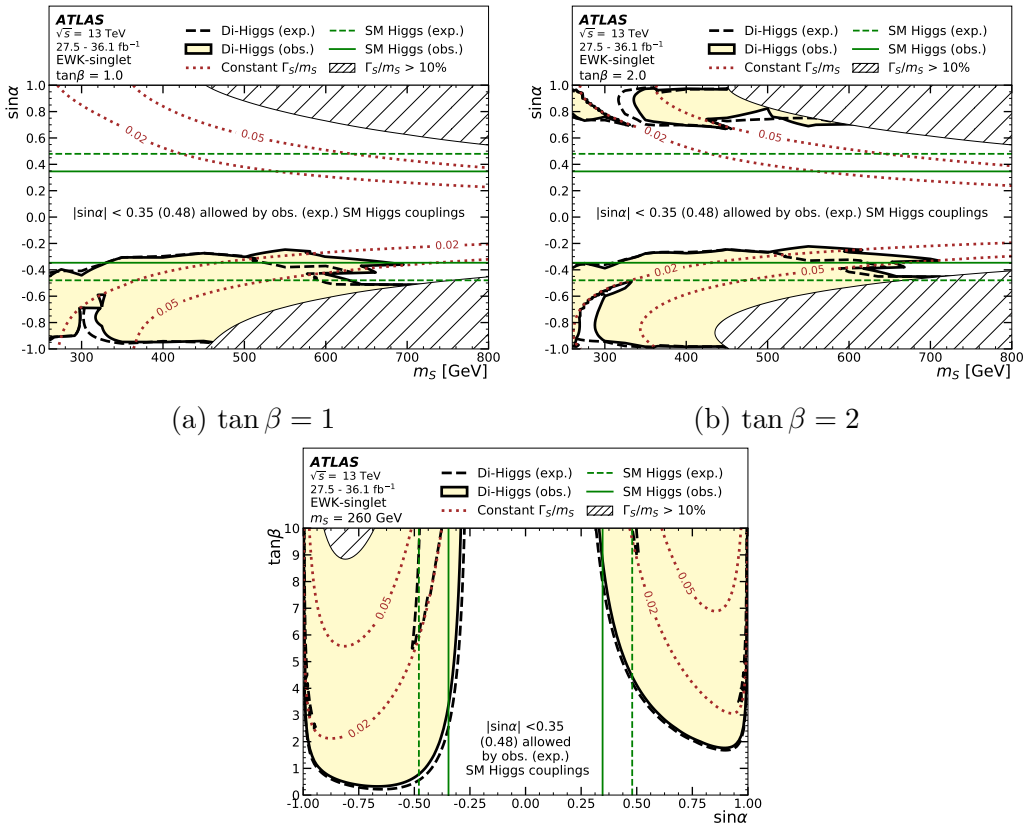

(a) $\tan\beta = 1$ (b) $\tan\beta = 2$

(c) $m_S = 260$ GeV

Figure 7.7: Excluded regions for the EWK-singlet model (light yellow) for $\tan\beta = 1$ (a), $\tan\beta = 2$ (b), and $m_S = 260$ GeV (c). Detailed description in the text.

Both types of searches, non-resonant and resonant, have been performed using only gluon fusion production of the Higgs pairs and neglecting other production channels due to their much smaller cross-sections. No statistically significant excess of events with respect to the Standard Model predictions is found. The observed (expected) 95% confidence level upper limit on the SM-like di-Higgs production cross-section is 6.9 (10) times the Standard Model prediction. Additionally, upper limits on the Higgs pair production cross-section are extracted as a function of the Higgs boson self-coupling modifier κ_λ, by combining the three most sensitive final states: $bbbb$, $bb\tau\tau$, and $bb\gamma\gamma$. This combination excludes the values of κ_λ outside the range $-5.0 \leq \kappa_\lambda \leq 12.0$ at 95% confidence level.

Upper limits are set on the production cross-section of selected resonant enhancements of the SM cross-sections, such as heavy spin-0 and spin-2 resonances in the mass range 260–3000 GeV, decaying into pairs of Higgs bosons.

The above mentioned three final states are also combined to constrain the Electroweak Singlet Model in the $(m_S, \sin\alpha)$ as well as the $(\sin\alpha, \tan\beta)$ parameter spaces. At the current stage Higgs pair searchers have slightly larger constraining power than searchers probing single Higgs boson production.

Measuring the interval of allowed values of κ_λ, $-5.0 < \kappa_\lambda < 12.0$, is a big success of the studies presented in this Chapter. The sensitivity using early Run 2 dataset is, however, still insufficient to exclude a non-self-interacting Higgs scenario ($\kappa_\lambda = 0$).

There is an interesting line of research connecting properties of the Higgs boson potential with a speculated electroweak baryogenesis [179]. The evolution of the Higgs potential with decreasing temperature of the Universe could enable phase transition between CP-violating and CP-conserving parameter spaces leading to baryon–anti-baryon asymmetry observed today. For the electroweak phase transition to meet out-of-equilibrium conditions [180, 181] required by electroweak baryogenesis models, the Higgs potential (and its self-coupling!) must deviate from the SM. Current exclusion limits on κ_λ do not provide sufficient constraining powers for these models, yet the increasing precision of its measurements opens doors to eventually answering this fundamental question in collider experiments.

Further studies undertaken by ATLAS experiment employing $bb\gamma\gamma$ [182], $bb\tau\tau$ [183], multileptonic final states without [184] and with b quarks [185], that are beyond the scope of this monograph, increase the sensitivity to κ_λ by utilising the full 140 fb^{-1} dataset of in Run 2. The combined result of Ref. [186] employs all the above final states and obtains allowed range of,

$-1.2 < \kappa_\lambda < 7.2$. Additionally, this last search employs vector boson fusion production of the Higgs pairs and constrains also a quartic coupling between two vector bosons and two Higgs bosons, κ_{2V}. Probing BSM deviations in multiple coupling strengths simultaneously is a complicated task, especially since the correlations between some of them decrease the overall sensitivity. Such a case was found by CMS experiment when constraining simultaneously κ_λ and Higgs coupling to top quarks in Ref. [187].

With increasing dataset, in particular during the upgraded High Luminosity LHC, and the number of analysed production and decay channels, we expect to constrain Higgs boson potential even better. Some of the possibilities and challenges anticipated at High Luminosity LHC are presented in the next Chapter.

8 Projections towards the High Luminosity LHC

This chapter presents the first feasibility study of Higgs pair production and the measurement of the Higgs trilinear self coupling performed by ATLAS experiment in view of the High Luminosity LHC (HL-LHC) upgrade programme. For this study, a parameterised simulation of the upgraded ATLAS detector is used and expected pileup conditions are accounted for. This chapter is is based on two publications: [6] and [188], that I co-authored.

8.1 Infrastructure upgrades

8.1.1 Planned accelerator upgrades

After completion of Run 3, major engineering works are foreseen in order to achieve higher centre-of-mass energies and unprecendented collision rates of proton bunches of the LHC. This planned new accelerator is therefore called High Luminosity LHC, or HL-LHC. The upgrade of superconducting magnets in the LHC tunnel will enable achieving the collision energy of 14 TeV.

The designed instantenuous luminosity of the HL-LHC is 7.5×10^{34} cm^{-2}s^{-1}, which should enable collecting $\sim$3000 fb^{-1} during a period of about 10 years. Collisions will be recorded at rates up to 40 MHz, with up to $\mu = 200$ proton-proton interactions per bunch crossing. This is a factor of $3-10$ more interactions per bunch crossing than during "standard" LHC runs. These conditions result in highly increased radiation as well as larger pileup. Pileup is related to difficulties in resolving primary vertices from different interactions due to large number of collision rate per bunch crossing. As a result, physics objects

or their parts, such as tracks or energy deposits in calorimeters, from one interaction might be wrongly attributed to another. Pileup is a complication present already during the current runs of the LHC and it is being mitigated with constantly improved software modeling of the detector working conditions as well as reconstrution algorithms. For the HL-LHC, in addition to the dedicated software, important upgrades in detector hardware are planned.

8.1.2 High Luminosity upgrade of the ATLAS detector

The change of collision rates between the LHC and HL-LHC from $\mu = 60$ to 200 require redesigning detectors. The foreseen improvements of the ATLAS detector are described in the Letter of Intent [189], where various layout options are considered, summarised in the Scoping Document [190] (2015).

In the trigger and data acquisition system two-level hardware trigger with L0 output rate up to 1MHz and L1 up to 400 KHz is forseen together with a High-Level Trigger with 10 kHz output (permanently recorded data). Custom hardware triggers will enable for data streaming at rates $1 - 40$ MHz. New readout systems in the Inner Tracker, Calorimeters and Muon Spectrometer will be installed, in order to maintain the detector performance. Physics goals require to maintain efficient triggers for isolated electrons, muons photons and τ leptons with transverse momentum thresholds around 20 GeV.

The ATLAS inner tracker, now consisting of pixel and strip silicon subdetectors and transition radiation tracker, will be replaced with a new, all silicon detector. This material ensures maintaing tracking performance in conditions of high occupancy as well as long-term operations in the much increased radiation environment. Its pseudorapidity coverage will be increased with respect to the current from 2.4 to 4 by the addition of 4 pixel discs in the forward region.

Improvements in the forward regions of the calorimeters are foreseen to cope with cell noise. Liquid Argon (LAr) forward electromagnetic calorimeter with be replaced by a higher granularity detector (sFcal). Additionally, High Granularity Timing Detector will be installed in front of LAr end-caps, at pseudorapidity region $2.4 \leq |\eta| \leq 4.3$. Readout electronics of LAr and Tile Calorimeters will be replaced. Additionally, new elements called Resistive Plate Chambers (RPC) are expected in the muon detector.

Software developments are ongoing continuously since Run 1 with the foreseen major milestones including:

- reconstruction of charged particles using the information from the tracker and from the calorimeter simultaneously (the so-called "particle flow" algorithms),
- improved track association to jets and flavour tagging,
- many algorithms will be improved using informations from previous runs and improved MC simulations,
- the usage of machine learning techniques in: pileup mitigation/subtraction and tagging short-lived heavy particles.

8.2 Feasibility of observing Higgs boson pairs in the $bb\gamma\gamma$ channel

In this study the dominant di-Higgs production process, gluon fusion, was explored. The final state was chosen to be $bb\gamma\gamma$, following phenomenological studies [1, 132, 133, 191] predicting reasonable sensitivity to observe this process.

This analysis is based upon software and detector modelling available in 2014, thus does not include updates in reconstruction techniques described in the previous Chapter.

8.2.1 Monte Carlo samples

The processes constituting irreducible backgrounds in this channel are: continuum (non-resonant) $bb\gamma\gamma$ production, as well as single Higgs decaying to a pair of photons and produced in association with two top quarks, Z boson and two b quarks, $ttH(\rightarrow \gamma\gamma)$, $Z(\rightarrow bb)H(\rightarrow \gamma\gamma)$ and $bbH(\rightarrow \gamma\gamma)$, respectively. In addition to irreducible backgrounds, whose experimental signatures are identical to the signal signature, reducible contributions originate from final states, in which one or more objects are misidentified. For example: a light flavour jet or c-jet is sometimes mis-identified as a b-jet, or an electron or jet initiated by a light flavour quark (j) is wrongly identified as a photon. The possible contribution from each of these processes depends on the mis-identification probability ("fake rate") for each type of an object. Therefore, based on the estimated magnitude of the various fake rates and the cross sections of the processes, the following final states were considered as

the most significant background contributions in the present analysis: $jj\gamma\gamma$, $cc\gamma\gamma$, $bb\gamma j$, tt and $tt\gamma$. There may possibly be other processes which contribute to reducible backgrounds. This analysis neglects for instance the effect of multiple interactions per bunch-crossing, during which some objects may be produced in one collision and other may arise from another, with two primary vertices indistinguishable from one another. These effects of multi-parton interactions were not included due to lack of detailed studies on the future performance of the upgraded detector and large theoretical uncertainties in modelling these processes.

This analysis is performed using events simulated using Monte Carlo (MC) methods. Signal processes were generated, at the leading order, employing finite top quark mass approximation, using Madgraph5 "SM" model [144]. For the Higgs boson decays and parton showering PYTHIA 8 [63] was used. The event yields were normalised to the NNLO cross-section calculations of Refs. [192, 193] (utilising infinite top quark mass). The signal samples were generated with the values of the Higgs self-coupling strength: λ_{3h} resulting in $\kappa_\lambda \in \{0, 1, 2, 10\}$.

The majority of background processes were generated with Madgraph 5 matrix elements matched to PYTHIA 8 parton showers. The top quark pair production was generated with MC@NLO matrix elements and HERWIG [172] parton shower at the NNLO.

Multi-jet processes: $bb\gamma\gamma$, $bb\gamma j$, $bbjj$, $cc\gamma\gamma$ and $jj\gamma\gamma$ (j denoting a light flavour and c a c-quark jet) were simulated inclusively (e.g. allowing for an additional jet in the tree-level matrix element) at the leading perturbative order in QCD. A threshold on the jet and photon transverse momenta was set at 20 GeV. Events originating from $jj\gamma\gamma$ samples, that through showering acquire heavy flavour quarks in the final state, are removed to avoid double counting of events with b and c quarks.

For generation of single Higgs processes various generators were used, all providing NLO accuracy. The $Z(\to bb)H(\to \gamma\gamma)$ proces was generated with PYTHIA 8. For $ttH(\to \gamma\gamma)$ POWHEG [147] was used. $bbH(\to \gamma\gamma)$ was generated with Madgraph 5 and showered with PYTHIA. The normalisation of single Higgs cross-sections follows LHC cross-section working group recommendations [131, 148, 149]. They are normalised to NNLO with exception of ttH and bbH, for which only NLO cross-sections were available at that time.

8.2.2 Object definitions

This sensitivity study was performed using simplified simulation of detector performance. The modeling of expected performance of the ATLAS detector was done by randomly distorting the four vectors of final state particles obtained in the simulations using the so-called smearing functions. Smearing functions were derived from the full detector simulations for benchmark processes, using $\mu = 140$ [194, 195].

Photons are defined as with $p_T > 30$ GeV and $|\eta| < 1.37$ or $1.52 < |\eta| < 2.37$ to match the detector coverage. [1] The photon smearing functions have been updated with respect to those described in Refs [194, 195]: the smearing in the azimuthal angle has been replaced with a smearing of 10 mrad/$\sqrt{E[GeV]}$. Photons must be isolated with respect to all jets in the event, which means that there are no jets within an annulus of $0.1 < \Delta R < 0.4$ around the photon candidate, and any jet reconstructed within a cone of $\Delta R < 0.1$ must have an energy within 15% of the photon energy. In the latter case, a jet is accociated with the QED radiation from a photon. The identification of photons is modelled with a function dependent on its transverse momenta, that reaches a plateau efficiency equal to 76% for photons with transverse momenta larger than 80 GeV.

Jets are identified using anti-k_T algorightm with a cone size $R = 0.4$ and are required to have transverse momenta $p_T > 25$ GeV and $|\eta| < 2.5$. Truth b-jets are identified by finding a truth b-hadron within a cone of 0.4 around the jet direction. The b-tagging performance for these jets is then modeled by applying an efficiency function, at a working point corresponding to a mean efficiency of 70%. This means that on average 70% of b-jets are correctly identified.

It was found that the reconstructed invariant mass of b-quark pairs, m_{bb}, in the signal samples had a maximum at around 113 GeV, significantly below the generated Higgs mass of 125 GeV. This effect is attributed to radiation of partons outside the jet cone as well as semi-leptonic b-hadron decays resulting in measuring only a fraction of the energy of a b-jet. Consequently, the acceptance of signal events was drastically decreased. Therefore, a correction was derived as the ratio of the energy of a b-quark and that of a full jet. Following application of this correction to the truth jets, the most probable value of m_{bb} in signal improved from 113 GeV to 127 GeV, much closer

[1] Extension in the tracker coverage to $|\eta| < 4$ was not accounted for in the present study.

to the expected value. This correction is similar to an experimental Jet Energy Scale correction, here applied in a simplified way since the detector performance is not known. The transverse momentum of the jets is smeared by $10-25\%$ using the parametrization that depends on both pseudorapidity and transverse momenta.

For leptons an isolation requirement is applied: there should be no jets with $p_T > 10$ GeV within the isolation cone $0.1 < \Delta R < 0.4$ from any lepton.

The misidentification probabilities for: jet $\rightarrow$ photon, light flavour jet $\rightarrow$ b-jet and c-jet $\rightarrow$ b-jet are provided by the so-called fake rate functions, derived from simulation. They are of the order 0.25%, 1% and 30% respectively. These numbers were derived based on qualities of flavour taggers developed in Run 1 [150]. The electron $\rightarrow$ photon fake rates were obtained for the barrel and endcap calorimeters separately, assuming the current level of detector performance. The mis-identification probability is of 2% in the barrel ($|\eta| < 1.37$) and 5% in the endcap ($1.37 < |\eta| < 2.37$).

In order to ensure that there is no duplication in the final-state objects, the so-called overlap removal is applied.

8.2.3 Signal selection

A cut-based signal selection was performed. In order to choose best phase space cuts, several kinematical variables have been studied. Figures 8.1 and 8.2 present b-quark jets and photons in the SM signal and backgrounds. Distributions related to the di-Higgs system are displayed in Fig. 8.3, and jet multiplicity in Fig. 8.4. In all these figures part of the $jj\gamma\gamma$ backgrounds featuring lighter flavour jets are not displayed because they largely resemble the dominant $bb\gamma\gamma$ process.

Events are required to pass the following criteria:

- There are at least 2 isolated photons present in the event.
- At least 2 jets must be identified as b-jets with leading (subleading) transverse momenta of 40 (25) GeV and pseudorapidity $|\eta| < 2.5$.
- There are no isolated leptons with transverse momenta larger than 25 GeV and $|\eta| < 2.5$.
- The total number of jets in the event must not exceed 6.

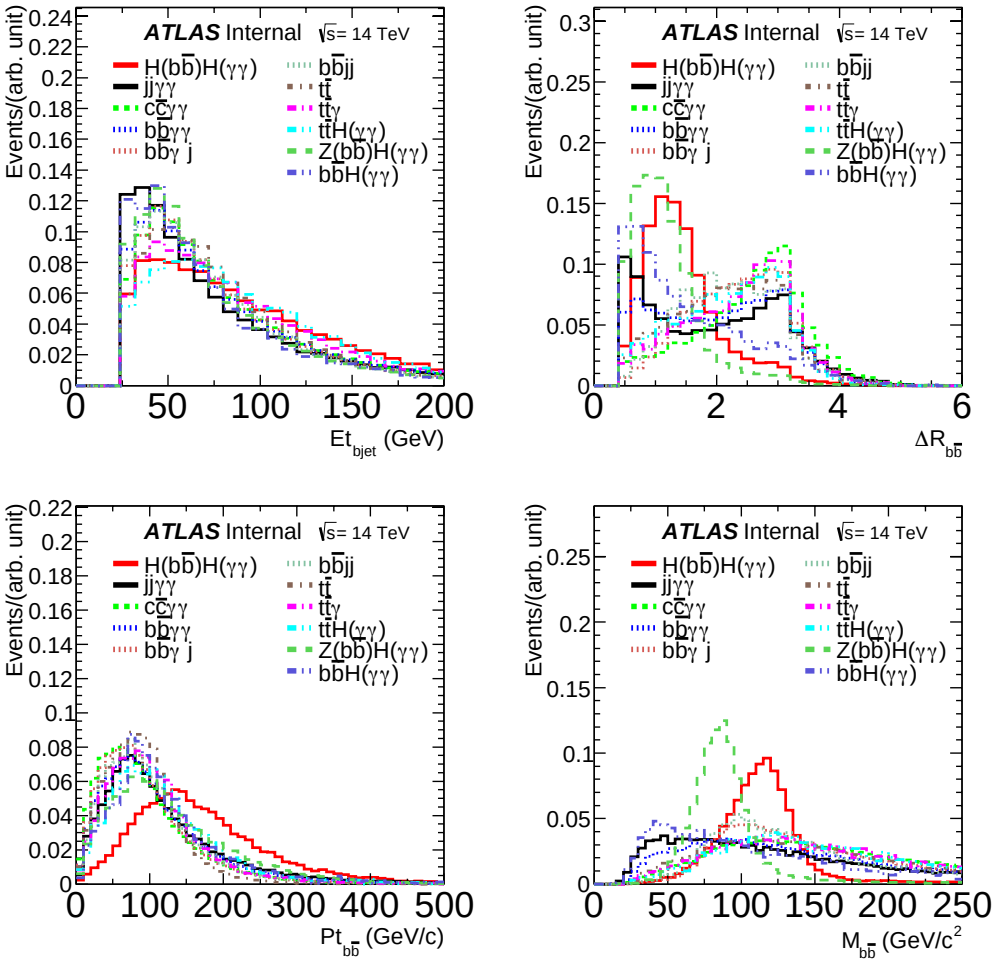

Figure 8.1: Signal and background distributions for transverse energy of a b-quark jet (top left), transverse momentum of the b-quark pair (bottom left), angular separation between the two b-jets (top right), and invariant mass of the two b-quarks (bottom right).

- Isolation requirements are applied between decay products of either of the Higgs boson: $\Delta R_{bb} > 0.4$, $0.4 < \Delta R_{\gamma\gamma} < 2.0$,

- Minimal isolation between decay products of the two Higgs bosons: $\Delta R_{b\gamma} > 0.4$.

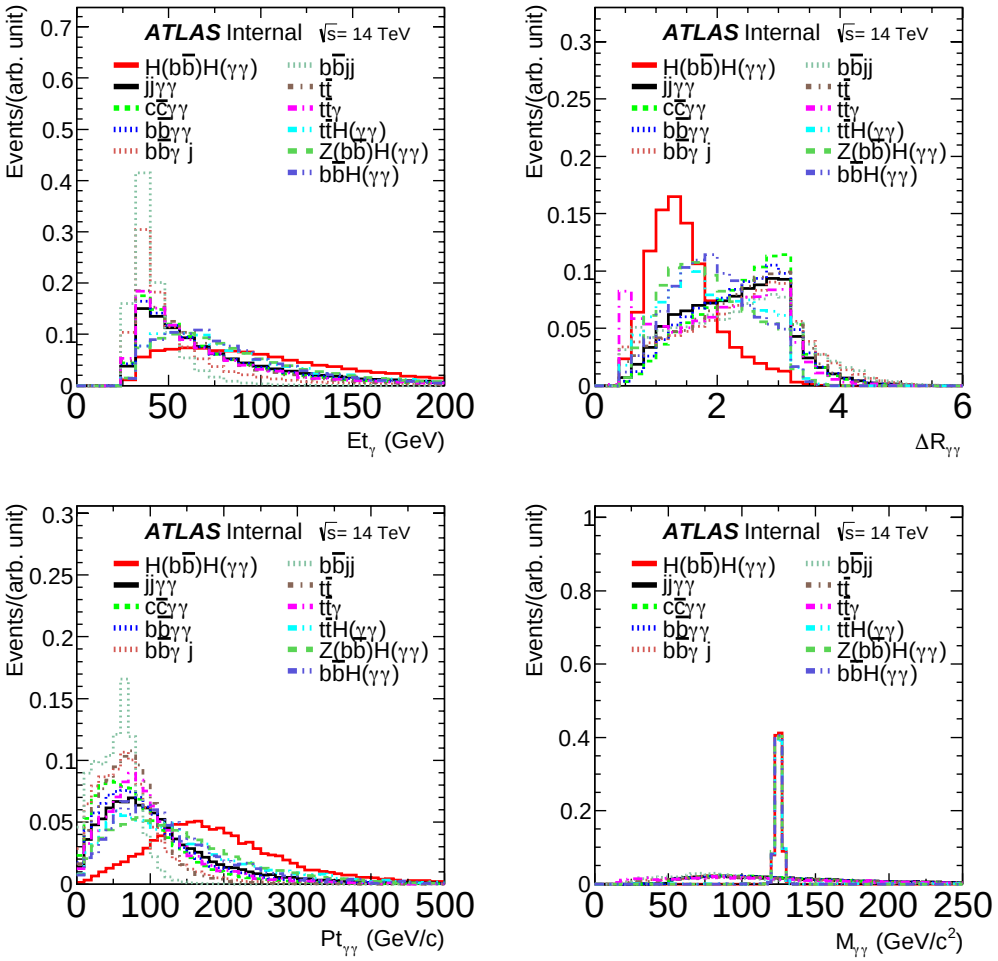

Figure 8.2: Signal and background distributions for E_T^γ (top left), $\Delta R_{\gamma\gamma}$ (top right), $p_T^{\gamma\gamma}$ (bottom left), and $m_{\gamma\gamma}$ (bottom right).

- Invariant masses of the di-photon and di-b systems must fall within their respective windows: $123 < m_{\gamma\gamma} < 128$ GeV and $100 < m_{bb} < 150$ GeV.
- Transverse momenta of the di-photon and di-b systems must be sufficiently large: $p_T^{\gamma\gamma}$, $p_T^{bb} > 110$ GeV.

Selection criteria based on angular separation were inspired by Ref. [191]. Optimisation studies of these cuts were performed here independently and on

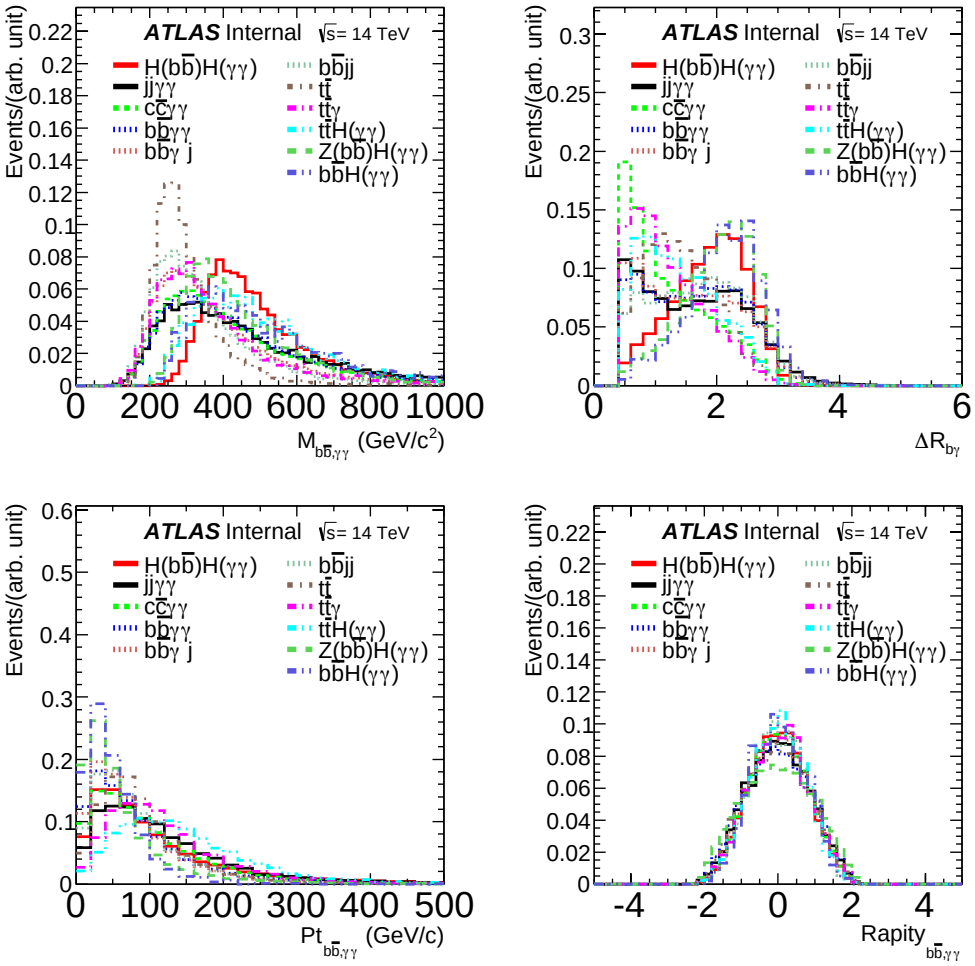

Figure 8.3: Signal and background distributions for $m_{bb\gamma\gamma}$ (top left) , $\Delta R_{b\gamma}$ (top right), $p_{T_{bb\gamma\gamma}}$ (bottom left), and $\eta_{bb\gamma\gamma}$ (bottom right).

a wider range of backgrounds than in Ref [191]. It was found that tightening the separation of b-jets to $\Delta R_{bb} < 2.0$ further improves signal significance and this requirement was added. Vetoing isolated leptons proved useful for decreasing the contribution from (semi-)leptonically decaying top quark pairs.

Some of the criteria above might need to be further optimised once pile-up contamination is rigorously taken into account. For example, selection based on transverse momenta of a combined bb object might result in accepting

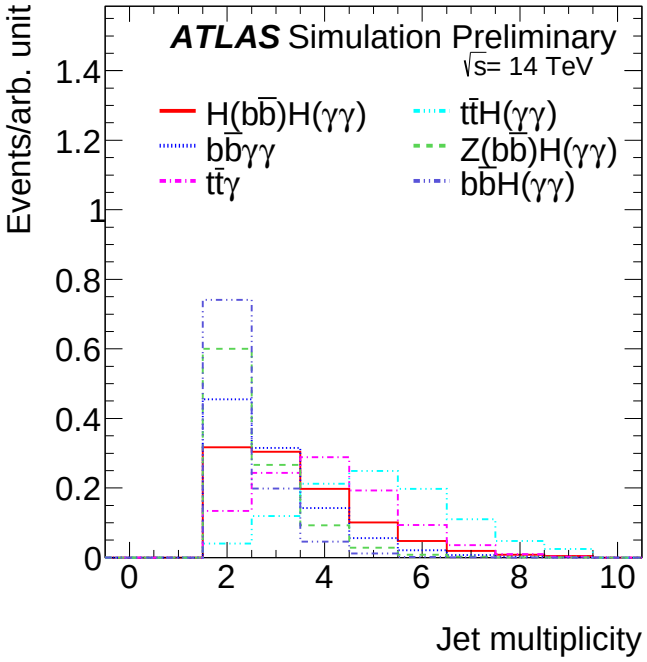

Figure 8.4: Jet multiplicity distribution in signal and backgrounds.

events consisting of one very high-p_T jet from a genuine background process paired with a soft jet from pile-up. Likewise, the upper cut on the number of jets, justified by Figure 8.4 can only be done under assumption of an efficient pile-up suppressing algorithm, such as Jet Vertex Tagging, decribed in Ref [86]. It is worth noting, that at the time this study was performed, the estimate on the number of jets in the signal sample varied between versions 6 and 8 of the PYTHIA generator used in the simulations. Since PYTHIA 8 predicts larger jet multiplicity, this parton shower generator was chosen in order to provide a conservative estimation of sensitivity.

8.2.4 Results

The number of events in selected SM and BSM signals (parametrised by values of κ_λ, with $\kappa_\lambda = 1$ corresponding to the SM) and backgrounds that pass selection criteria are summarised in Table 8.1. Events are split into two categories: the first one with both photons in the barrel ($|\eta| < 1.37$) and

the second with at least one photon in the endcap part of the calorimeter ($1.52 < |\eta| < 2.37$). This procedure takes advantage of different signal-to-background ratios as well as photon misidentification probabilities in these regions and improves the expected significance. The uncertainties that are listed in Table 8.1 result from the available Monte Carlo statistics. Background labels are meant exclusively: the $bb\gamma\gamma$ events contain at least two b-jets, the $cc\gamma\gamma$ contain two c jets and no b-jets, and so on, to avoid multiple counting of the same event. The expected SM signal yield is 6.7 (1.8) events in the barrel (endcap) and the corresponding expected background yield is 29 (19) events. The final rows shows the resulting signal significance, $S/\sqrt{B}$, that yield 1.2 and 0.4 in the barrel and endcap, respectively. Combining these significances in quadrature leads to the combined significance of $\sim$1.3.

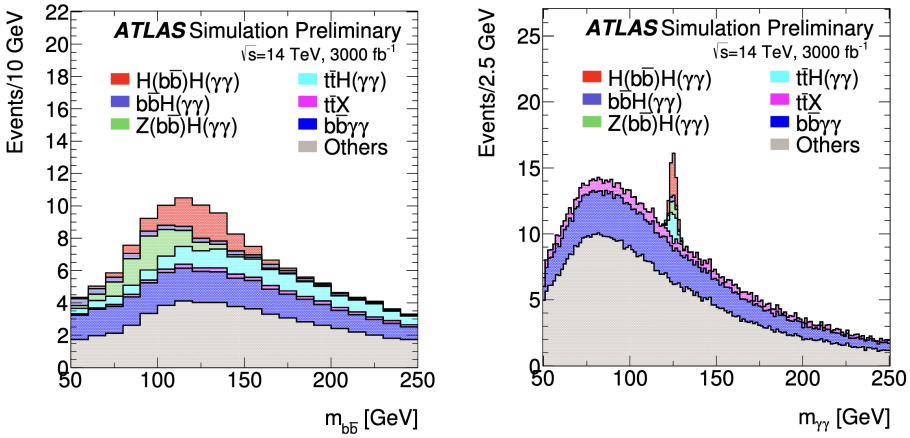

(a) m_{bb} distribution (b) $m_{\gamma\gamma}$ distributions

Figure 8.5: The distributions of m_{bb} and $m_{\gamma\gamma}$. Histograms representing all processes are stacked. All selection criteria except for m_{bb} and $m_{\gamma\gamma}$ requirements are applied.

Figure 8.5 shows the distributions of invariant masses of reconstructed di-b and di-photon systems, m_{bb} and $m_{\gamma\gamma}$, after applying all the selection criteria except for m_{bb}/ $m_{\gamma\gamma}$. To obtain a better statistics, the individual shape is obtained using the events before the mass and angular cuts are applied, but normalized to the number of expected events.

An upper limit on the number of total di Higgs signal events is set based on the simulated dataset corresponding to 3000 fb^{-1}. It is assumed for sim-

Table 8.1: The number of events in SM (κ_λ=1) and BSM (κ_λ = 0, 2, 10) signals and background processes expected in 3000 fb^{-1} passing selection requirements.

Samples	Expected number of events	Events in the barrel	Events in end-caps
$H(bb)H(\gamma\gamma)(\kappa_\lambda = 1)$	8.4 ± 0.1	6.7 ± 0.1	1.8 ± 0.1
$H(bb)H(\gamma\gamma)(\kappa_\lambda = 0)$	13.7 ± 0.2	10.7 ± 0.2	3.1 ± 0.1
$H(bb)H(\gamma\gamma)(\kappa_\lambda = 2)$	4.6 ± 0.1	3.7 ± 0.1	0.9 ± 0.1
$H(bb)H(\gamma\gamma)(\kappa_\lambda = 10)$	36.2 ± 0.8	27.9 ± 0.7	8.2 ± 0.4
$jj\gamma\gamma$	7.4 ± 1.8	5.2 ± 1.5	2.2 ± 1.0
$cc\gamma\gamma$	7.0 ± 1.2	4.1 ± 0.9	2.9 ± 0.8
$bb\gamma\gamma$	9.7 ± 1.5	5.2 ± 1.1	4.5 ± 1.0
$bb\gamma j$	8.4 ± 0.4	4.3 ± 0.2	4.1 ± 0.2
$bbjj$	1.3 ± 0.2	0.9 ± 0.1	0.4 ± 0.1
$tt(\geq 1$ lepton)	0.2 ± 0.1	0.1 ± 0.1	0.1 ± 0.1
$tt\gamma$	3.2 ± 2.2	1.6 ± 1.6	1.6 ± 1.6
$ttH(\gamma\gamma)$	6.1 ± 0.5	4.9 ± 0.4	1.2 ± 0.2
$Z(bb)H(\gamma\gamma)$	2.7 ± 0.1	1.9 ± 0.1	0.8 ± 0.1
$bbH(\gamma\gamma)$	1.2 ± 0.1	1.0 ± 0.1	0.3 ± 0.1
Total Background	47.1 ± 3.5	29.1 ± 2.7	18.0 ± 2.3
$S/\sqrt{B}$ ($\kappa_\lambda = 1$)	1.3	1.2	0.4

plicity that the signal acceptance does not depend on the Higgs self-coupling modification κ_λ. In the case of systematic uncertainties being negligible with respect to statistical ones, as is considered in this study, the number of Higgs pair events depends quadratically on κ_λ. The CL_s technique [155] is used leading to the exclusion at 95% C.L. of models with $\kappa_\lambda < -1.3$ and $\kappa_\lambda > 8$.

8.3 Summary

This Chapter presents the first feasibility study, performed by ATLAS experiment, of measuring Higgs boson pairs at the upgraded ATLAS detector at the HL-LHC. A single $h(\to bb)h(\to \gamma\gamma)$ final state is employed. Conservative estimates on efficiencies of reconstructing photons and b-quarks are adopted in order to account for high pile-up conditions foreseen at the HL-LHC.

The analysis described in this Chapter reports observation of Higgs pairs at the sensitivity of about 1σ, and sets broad limits on the Higgs boson self-coupling λ_{3h}. It demonstrates, how challenging it is going to be to observe this process even with huge statistics of HL-LHC. In the time of publishing, this result stood in contrast to phenomenological studies performed at the same time, such as those described in [116, 132, 133], that reported significantly higher signal significance ($S/\sqrt{B}$) than obtained here. In particular, in Ref. [116] it is predicted that the Higgs boson self-coupling might be measured within a factor of two in the $h(\to bb)h(\to \gamma\gamma)$ channel at HL-LHC. The cause of discrepancies is related to a more optimistic assumptions on the $hh \to bb$ mass resolution than adopted here, which allows the mass of the bb sytem to become a much more powerful discriminant. Additionally, the phenomenological studies do not consider the full range of background, omitting for example top quark production processes, that are accounted for in this study.

Experimental study presented in this Chapter does not fully account for systematical uncertainties. The assumptions on pileup are included in the distortion of four-momenta of reconstructed objects and assume no event overlap. Likewise, it is assumed that by the time of the HL-LHC all backgrounds will be well understood through studying their dedicated control regions, and therefore background normalisation uncertainties are neglected. Such improvement in constraining background processes is demonstrated in the early studies of this process in Run 1 data [139], performed in parallel with HL-LHC analysis, and later, in Run 2 studies reported in Ref. [171].

On the other hand, the study described in this Chapter may have not employed the optimal suppression of the dominant $jj\gamma\gamma$ backgrounds. The 70% flavour tagging working point is utilised, that gives large signal acceptance at the cost of large fake rate. In later analyses performed in data a more detailed optimisation of the flavour tagging working point was carried out resulting in a better background suppresion. Additionally, the full detector coverage of the modernised tracking detector, $|\eta| < 4$, was not taken into account. This improvement will likely result in a better signal acceptance through better reconstruction and identification of forward jets.

This analysis focuses on optimising angular separation variables. A number of observables, such as the sub-leading photon transverse momentum, have not been used in the event selection because of their insufficient discriminating power. Such obervables, however, could be included in algorithms employing Machine Learning algorithms: boosted decision trees (BDT) or neural networks, and used to further enhance the signal significance.

A more recent study of HL-LHC prospects of measuring di-Higgs production in the $bb\gamma\gamma$ channel performed by ATLAS [196], is conducted using a different methodology than described in this Chapter. It is based on extrapolations of the Run 2 results, obtained with 139 fb^{-1}, in which signal-like events are divided into four categories based on the value of a BDT discriminant and reconstructed di-Higgs invariant mass. To account for the increased luminosity and center-of-mass energy at the HL-LHC, dedicated multiplicative scale factors are used. Additionally, experimental and theoretical systematic uncertainties are scaled with respect to their Run 2 values. Most experimental uncertainties are expected to be reduced relative to their Run 2 values due to both detector upgrades and improved understanding of its performance. Theory systematics are halved with respect to their Run 2 estimates. The extrapolated precision on the signal strength measurement with (without) systematic uncertainties is 50% (46%), with a corresponding signal significance of 2.2σ (2.3σ). Assuming SM values of all other couplings, the 1σ confidence interval constraining κ_λ is projected to be [0.3,1.9] ([0.4,1.8]) with (without) systematic uncertainties. This study shows that sensitivity of Higgs pair production in the $bb\gamma\gamma$ channel at the HL-LHC will rely on proper control of the background modeling.

Higgs pair production remains one of the most exciting processes to be observed, and is crucial in driving the design of next generation high energy physics experiments.

9 Summary

This monograph summarises studies of Higgs boson properties in its decays to pairs of W or Higgs bosons and searches for beyond Standard Model interactions.

Higgs boson has been for many years a missing piece of the quantum field theory description of unified electro-magnetic and weak interactions. Its discovery marks a completion of the electroweak theory and at the same time opens up a new direction in investigating the properties of elementary particles. Studying Higgs boson properties has become a pursuit of many analyses by the ATLAS and CMS experiments. The mass, spin and CP properties, as well as coupling strengths to the electroweak bosons, third and second generations of quarks and leptons have been measured. These studies have confirmed the Standard Model (SM) nature of the new particle.

This monograph presents two experimental studies of the Brout-Englert-Higgs (BEH) mechanism, aiming at either confirming the SM picture of electroweak symmetry breaking or finding beyond SM effects. The first line of analyses targets Higgs boson production in vector boson fusion and measures its couplings to electroweak bosons, with the emphasis on disentangling couplings to longitudinally and transversally polarised W and Z bosons. The second set of analyses searches for pair-produced Higgs bosons, with the aim of constraining its trilinear self-coupling. In this way, the shape of the Higgs boson potential can be experimentally measured.

Presented studies include measurements of inclusive cross-section of Higgs boson production via the gluon–gluon fusion (ggF) and vector-boson fusion (VBF) at $\sqrt{s} = 13$ TeV, using the fully leptonic Higgs boson decays via WW^*. The VBF production is further utilised to perform a measurement of Higgs boson coupling-strengths to longitudinally and transversely polarised W and Z bosons. In this way Higgs boson couplings to longitudinally polarised bosons are scrutinised and compared with the BEH mechanism predictions.

Measurements using polarisations of electroweak bosons, such as the one described in this monograph, are not confined to the Higgs physics. The other manifestation of longitudinal degrees of freedom of electroweak bosons is the behaviour of their scattering amplitudes at energies ~ 1 TeV. If the Higgs boson coupling to longitudinally polarised W bosons matches the value predicted by the BEH mechanism, the cross-section for scattering of the longitudinally polarised W bosons decreases with energy. Possible deviations should manifest themselves by increased values of cross-sections. ATLAS has observed production of W^+W^- boson pairs in association with two jets [197] and measured the cross-section for this process to be in agreement with the Standard Model predictions. With the full Run 2 dataset of 140 fb^{-1}, polarisation-sensitive measurements in di-boson final states at high energies are also starting to be statistically significant: [198, 199].

In the domain of Higgs pair production, this monograph summarises both theory developments in calculating Higgs pair production in the SM, and my own phenomenology studies related to maximising sensitivity to Higgs trilinear coupling using LO predictions. These works have led to establishing theory predictions and recommendations for experimental studies, summarised in a dedicated chapter of CERN Yellow Report 4 [2] that I coordinated within the Higgs Cross Section Working Group.

Experimental Higgs pair searchers presented in this monograph were performed using Run 1 and early data of Run 2 of the LHC. The emphasis is put on statistical combination of several search channels. In Run 1 four final states were studied: $bbbb$, $bb\gamma\gamma$, $bb\tau\tau$, and $WW\gamma\gamma$. In Run 2 two more channels were added: bbW^+W^- and $W^+W^-W^+W^-$. Neither dataset is sufficient to observe SM Higgs pair production. Therefore, several generic beyond Standard Model theories, predicting enhancement of the rates for this process, have been constrained. In particular, constraints on triple Higgs self-coupling have been established, providing first measurements of the Higgs boson potential. Other generic models, for example these predicting BSM heavy scalar or spin-2 particles have been probed. Further studies performed by ATLAS include additionally VBF production and more di-Higgs final states. Eventually, these studies will enable an assessment of anomalous interactions by probing all coupling strengths involved in the double Higgs boson production within a unified framework of effective field theory operators (for example SMEFT, [200]).

The first feasibility study of measuring Higgs pair production at the High Luminosity LHC by the ATLAS experiment is also presented in this mono-

graph. This analysis is restricted to the $bb\gamma\gamma$ final state and uses Monte Carlo simulations and parameterised efficiencies and resolution to approximate the expected performance of the upgraded ATLAS detector under HL-LHC conditions.

With successfully ongoing Run 3 and well advanced constructions for the High Luminosity LHC, it is crucial to gradually improve analysis strategies to obtain best possible results. This monograph presented only the beginnig of efforts directed at measuring the Higgs potential. They will pave the road ahead to the next generations of particle physics experiments.

Bibliography

[1] M. Slawinska, W. van den Wollenberg, B. van Eijk, and S. Bentvelsen, *Phenomenology of the trilinear Higgs coupling at proton-proton colliders*, arXiv:1408.5010.

[2] D. de Florian et al., *Handbook of LHC Higgs cross sections: 4. Deciphering the nature of the Higgs sector*, 2017. https://e-publishing.cern.ch/index.php/CYRM/issue/view/32.

[3] ATLAS Collaboration, *Searches for Higgs boson pair production in the $hh \to bb\tau\tau, \gamma\gamma WW^*, \gamma\gamma bb, bbbb$ channels with the ATLAS detector*, *Physical Review D* **92** (2015) 092004. https://arxiv.org/abs/1509.04670.

[4] ATLAS Collaboration, *Search for Higgs boson pair production in the $b\bar{b}\gamma\gamma$ final state using pp collision data at $\sqrt{s} = 13$ TeV with the ATLAS detector*, Tech. Rep. ATLAS-CONF-2016-004, CERN, Geneva, 2016. https://cds.cern.ch/record/2138949.

[5] ATLAS Collaboration, *Combination of searches for Higgs boson pair production in pp collisions at $\sqrt{s} = 13$ TeV with the ATLAS detector*, *Physical Review Letters* **133** (2024), no. 10 101801.

[6] ATLAS Collaboration, *Prospects for measuring Higgs pair production in the channel $H(\to \gamma\gamma)H(\to b\bar{b})$ using the ATLAS detector at the HL-LHC*, Tech. Rep. ATL-PHYS-PUB-2014-019, CERN, Geneva, 2014. https://cds.cern.ch/record/1956733.

[7] ATLAS Collaboration, *Measurements of gluon-gluon fusion and vector-boson fusion Higgs boson production cross-sections in the $H \to WW^* \to e\nu\mu\nu$ decay channel in pp collisions at $\sqrt{s} = 13$ TeV*

with the ATLAS detector, *Physics Letters B* **789** (2019) 508–529. https://arxiv.org/abs/1808.09054.

[8] G. Giudice, C. Grojean, A. Pomarol, and R. Rattazzi, *The Strongly-Interacting Light Higgs*, *Journal of High Energy Physics* **0706** (2007) 045, [hep-ph/0703164].

[9] M. Gonzalez-Alonso, A. Greljo, G. Isidori, and D. Marzocca, *Electroweak bounds on Higgs pseudo-observables and $h \to 4\ell$ decays*, *European Physical Journal C* **75** (2015), no. 341. https://arxiv.org/abs/1504.04018.

[10] S. L. Glashow, *Partial-symmetries of weak interactions*, *Nuclear Physics* **22** (1961), no. 4 579–588.

[11] S. Weinberg, *A model of leptons*, *Physical Review Letters* **19** (1967) 1264–1266.

[12] A. Salam, *Weak and Electromagnetic Interactions*, *Conf. Proc. C* **680519** (1968) 367–377.

[13] F. Englert and R. Brout, *Broken Symmetry and the Mass of Gauge Vector Mesons*, *Physical Review Letters* **13** (1964) 321–323.

[14] P. W. Higgs, *Broken symmetries, massless particles and gauge fields*, *Physics Letters* **12** (1964) 132–133.

[15] P. W. Higgs, *Broken Symmetries and the Masses of Gauge Bosons*, *Physical Review Letters* **13** (1964) 508–509.

[16] **ATLAS** Collaboration, G. Aad *et. al.*, *Observation of a new particle in the search for the Standard Model Higgs boson with the ATLAS detector at the LHC*, *Physics Letters* **B716** (2012) 1–29, [arXiv:1207.7214].

[17] **CMS** Collaboration, S. Chatrchyan *et. al.*, *Observation of a new boson at a mass of 125 GeV with the CMS experiment at the LHC*, *Physics Letters* **B716** (2012) 30–61, [arXiv:1207.7235].

[18] P. W. Higgs, *Spontaneous Symmetry Breakdown without Massless Bosons*, *Physical Review* **145** (1966) 1156–1163.

[19] M. Thomson, *Modern Particle Physics*. Cambridge University Press, 2013.

[20] J. Brehmer, J. Jaeckel, and T. Plehn, *Polarized WW Scattering on the Higgs Pole*, *Physical Review* **D90** (2014), no. 5 054023, [arXiv:1404.5951].

[21] C. Anastasiou, C. Duhr, F. Dulat, E. Furlan, T. Gehrmann, F. Herzog, A. Lazopoulos, and B. Mistlberger, *High precision determination of the gluon fusion Higgs boson cross-section at the LHC*, *Journal of High Energy Physics* **2016** (2016) 1–101.

[22] "Public ATLAS Luminosity Results for Run 2 of the LHC." https://twiki.cern.ch/twiki/bin/view/AtlasPublic/LuminosityPublicResultsRun2.

[23] J. Pequenao, "Computer generated image of the whole ATLAS detector." https://cds.cern.ch/record/1095924, 2008.

[24] J. Pequenao and P. Schaffner, "How ATLAS detects particles: diagram of particle paths in the detector." https://cds.cern.ch/record/1505342, 2013.

[25] ATLAS Collaboration, *Expected Performance of the ATLAS Experiment - Detector, Trigger and Physics*, arXiv:0901.0512.

[26] J. Pequenao, "Computer Generated image of the ATLAS calorimeter." https://cds.cern.ch/record/1095927, 2008.

[27] ATLAS Collaboration, *The ATLAS Experiment at the CERN Large Hadron Collider*, *Journal of Instrumentation* **3** (2008), no. 08 S08003. https://cds.cern.ch/record/1129811.

[28] ATLAS Collaboration, *ATLAS muon spectrometer: Technical Design Report*. Technical design report. ATLAS. CERN, Geneva, 1997. https://cds.cern.ch/record/331068.

[29] ATLAS Collaboration, *Performance of the ATLAS trigger system in 2015*, *The European Physical Journal C* **77** (2017), no. 5. http://dx.doi.org/10.1140/epjc/s10052-017-4852-3.

[30] ATLAS Collaboration, *Improved luminosity determination in pp collisions at $\sqrt{s} = 7$ TeV using the ATLAS detector at the LHC*, *European Physical Journal* **C73** (2013) 2518, [arXiv:1302.4393].

[31] ATLAS Collaboration, *Luminosity determination in pp collisions at $\sqrt{s} = 13\,TeV$ using the ATLAS detector at the LHC*, *The European Physical Journal C* **83** (2023), no. 10. http://dx.doi.org/10.1140/epjc/s10052-023-11747-w.

[32] G. Avoni, M. Bruschi, G. Cabras, D. Caforio, N. Dehghanian, A. Floderus, B. Giacobbe, F. Giannuzzi, F. Giorgi, P. Grafström, V. Hedberg, F. L. Manghi, S. Meneghini, J. Pinfold, E. Richards, C. Sbarra, N. S. Cesari, A. Sbrizzi, R. Soluk, G. Ucchielli, S. Valentinetti, O. Viazlo, M. Villa, C. Vittori, R. Vuillermet, and A. Zoccoli, *The new LUCID-2 detector for luminosity measurement and monitoring in ATLAS*, *Journal of Instrumentation* **13** (2018), no. 07 P07017.

[33] S. van der Meer, *Calibration of the effective beam height in the ISR*, tech. rep., CERN, Geneva, 1968. CERN-ISR-PO-68-31, ISR-PO-68-31, https://cds.cern.ch/record/296752.

[34] P. Grafström and W. Kozanecki, *Luminosity determination at proton colliders*, *Progress in Particle and Nuclear Physics* **81** (2015) 97–148.

[35] ALEPH, CDF, D0, DELPHI, L3, OPAL and SLD Collaborations, LEP Electroweak Working Group, Tevatron Electroweak Working Group and SLD electroweak heavy flavour group, *Precision Electroweak Measurements and Constraints on the Standard Model*, arXiv:1012.2367.

[36] ALEPH, DELPHI, L3 and OPAL Collaborations, The LEP Working Group for Higgs Boson Searches, *Search for the Standard Model Higgs boson at LEP*, *Physics Letters B* **565** (2003) 61–75.

[37] CDF Collaboration, *Combined Search for the Standard Model Higgs Boson Decaying to a $b\bar{b}$ Pair Using the Full CDF Data Set*, *Physical Review Letters* **109** (2012) 111802.

[38] D0 Collaboration, *Combined Search for the Standard Model Higgs Boson Decaying to $b\bar{b}$ Using the D0 Run II Data Set*, *Physical Review Letters* **109** (2012) 121802.

[39] CDF and D0 Collaborations, *Evidence for a Particle Produced in Association with Weak Bosons and Decaying to a Bottom-Antibottom Quark Pair in Higgs Boson Searches at the Tevatron*, *Physical Review Letters* **109** (2012) 071804.

[40] ATLAS Collaboration, *Combined search for the Standard Model Higgs boson in pp collisions at $\sqrt{s}$=7 TeV with the ATLAS detector*, *Physical Review D* **86** (2012) 032003.

[41] CMS Collaboration, *Combined results of searches for the Standard Model Higgs boson in pp collisions at $\sqrt{s} = 7$ TeV*, *Physics Letters B* **710** (2012), no. 1 26–48.

[42] ATLAS and CMS Collaborations, *Combined Measurement of the Higgs Boson Mass in pp Collisions at $\sqrt{s} = 7$ and 8 TeV with the ATLAS and CMS Experiments*, *Physical Review Letters* **114** (2015) 191803.

[43] ATLAS Collaboration, *Measurement of the Higgs boson mass in the $H \to ZZ^* \to 4l$ and $H \to \gamma\gamma$ channels with $\sqrt{s} = 13$ TeV pp collisions using the ATLAS detector*, *Physics Letters B* **784** (2018) 345–366.

[44] ATLAS Collaboration, *Combined Measurement of the Higgs Boson Mass from the $H \to \gamma\gamma$ and $H \to ZZ^* \to 4\ell$ Decay Channels with the ATLAS Detector Using $\sqrt{s} = 7$, 8, and 13 TeV pp Collision Data*, *Physical Review Letters* **131** (2023) 251802.

[45] ATLAS Collaboration, *Evidence for the spin-0 nature of the Higgs boson using ATLAS data*, *Physics Letters B* **726** (2013), no. 1 120–144.

[46] ATLAS Collaboration, *Study of the spin and parity of the Higgs boson in diboson decays with the ATLAS detector*, *The European Physical Journal C* **75** (2015) 476. [Erratum: European Physical Journal **C 76** (2016) 153].

[47] CMS Collaboration, *Study of the Mass and Spin-Parity of the Higgs Boson Candidate via Its Decays to Z Boson Pairs*, *Physical Review Letters* **110** (2013) 081803, [arXiv:1212.6639].

[48] ATLAS Collaboration, *A combination of measurements of Higgs boson production and decay using up to* 139 fb^{-1} *of proton–proton collision data at* $\sqrt{s} = 13$ *TeV collected with the ATLAS experiment*, tech. rep., CERN, Geneva, 2020. https://atlas.web.cern.ch/Atlas/GROUPS/PHYSICS/CONFNOTES/ATLAS-CONF-2020-027.

[49] A. Hill and J. van der Bij, *Strongly interacting Singlet – Doublet Higgs Models*, *Physical Review* **D36** (1987) 3463–3473.

[50] A. Djouadi, *The anatomy of electroweak symmetry breaking Tome II: The Higgs bosons in the Minimal Supersymmetric Model*, *Physics Reports* **459** (2008), no. 1–6 1–241.

[51] A. Djouadi and J. Quevillon, *The MSSM Higgs sector at a high* M_{SUSY}*: reopening the low* $\tan\beta$ *regime and heavy Higgs searches*, *Journal of High Energy Physics* **2013** (2013), no. 10 28.

[52] A. Djouadi, L. Maiani, G. Moreau, A. Polosa, J. Quevillon, and V. Riquer, *The post-Higgs MSSM scenario: habemus MSSM?*, *The European Physical Journal C* **73** (2013), no. 12 2650.

[53] G. Branco, P. Ferreira, L. Lavoura, M. Rebelo, M. Sher, and J. P. Silva, *Theory and phenomenology of two-Higgs-doublet models*, *Physics Reports* **516** (2012), no. 1–2 1–102.

[54] B. Patt and F. Wilczek, *Higgs-field Portal into Hidden Sectors*, 2006. https://arxiv.org/abs/hep-ph/0605188.

[55] D. B. Kaplan and H. Georgi, *SU(2)* $\times$ *U(1) breaking by vacuum misalignment*, *Physics Letters B* **136** (1984), no. 3 183 – 186.

[56] D. B. Kaplan, H. Georgi, and S. Dimopoulos, *Composite Higgs scalars*, *Physics Letters B* **136** (1984), no. 3 187 – 190.

[57] F. Bezrukov and M. Shaposhnikov, *The Standard Model Higgs boson as the inflaton*, *Physics Letters B* **659** (2008), no. 3 703–706.

[58] I. Masina and A. Notari, *Higgs mass range from Standard Model false vacuum inflation in scalar-tensor gravity*, *Physical Review D* **85** (2012), no. 12 123506.

[59] V. Branchina, H. Faivre, and V. Pangon, *Effective potential and vacuum stability*, *Journal of Physics G: Nuclear and Particle Physics* **36** (2008), no. 1 015006.

[60] D. Buttazzo, G. Degrassi, P. P. Giardino, G. F. Giudice, F. Sala, A. Salvio, and A. Strumia, *Investigating the near-criticality of the Higgs boson*, *Journal of High Energy Physics* **2013** (2013), no. 12 089.

[61] ATLAS Collaboration, *Constraints on Higgs boson properties using $WW^*(\to e\nu\mu\nu)jj$ production in 36.1 fb^{-1} at $\sqrt{s}$= 13 TeV pp collisions with the ATLAS detector*, *The European Physical Journal C* **82** (2022), no. 7 622. https://arxiv.org/abs/2109.13808.

[62] ATLAS Collaboration, *ATLAS data quality operations and performance for 2015 – 2018 data-taking*, *Journal of Instrumentation* **15** (2020), no. 04 P04003. https://arxiv.org/abs/1911.04632.

[63] T. Sjöstrand et al., *A Brief Introduction to PYTHIA 8.1*, *Comput. Phys. Commun.* **178** (2008) 852–867, [arXiv:0710.3820].

[64] ATLAS Collaboration, *Measurement of the Z/γ^* boson transverse momentum distribution in pp collisions at $\sqrt{s}$ = 7 TeV with the ATLAS detector*, *Journal of High Energy Physics* **09** (2014) 145, [arXiv:1406.3660].

[65] J. Alwall, R. Frederix, S. Frixione, V. Hirschi, F. Maltoni, *et. al.*, *The automated computation of tree-level and next-to-leading order differential cross sections, and their matching to parton shower simulations*, *Journal of High Energy Physics* **1407** (2014) 079, [arXiv:1405.0301].

[66] S. Frixione et al., *Matching NLO QCD computations and parton shower simulations*, *Journal of High Energy Physics* **0206** (2002) 029, [hep-ph/0204244].

[67] F. Maltoni et al., *Higgs characterisation at NLO in QCD: CP properties of the top-quark Yukawa interaction*, *European Physical Journal C* **74** (2014), no. 9 3065, [arXiv:1407.5089].

[68] ATLAS Collaboration, *ATLAS Pythia 8 tunes to 7 TeV data*, Tech. Rep. ATL-PHYS-PUB-2014-021, CERN, Geneva, 2014. https://cds.cern.ch/record/1966419.

[69] **NNPDF** Collaboration, R. Ball et al., *Parton distributions for the LHC run II*, *Journal of High Energy Physics* **04** (2015) 040, [arXiv:1410.8849].

[70] F. Demartin et al., *Higgs characterisation: NLO and parton-shower effects*, in *2nd Toyama International Workshop on Higgs as a Probe of New Physics*, 2015. https://arxiv.org/abs/1505.07081.

[71] S. Alioli, P. Nason, C. Oleari, and E. Re, *A general framework for implementing NLO calculations in shower Monte Carlo programs: the POWHEG BOX*, *Journal of High Energy Physics* **2010** (2010), no. 6 043.

[72] Jon Butterworth et al., *PDF4LHC recommendations for LHC Run II*, *J. Phys. G* **43** (2016) 023001. https://arxiv.org/abs/1510.03865.

[73] G. Luisoni et al., *$HW^{\pm}/HZ$ + 0 and 1 jet at NLO with the POWHEG BOX interfaced to GoSam and their merging within MiNLO*, *Journal of High Energy Physics* **10** (2013) 083, [arXiv:1306.2542].

[74] P. Z. Skands, *Tuning Monte Carlo generators: The Perugia tunes*, *Physical Review D* **82** (2010) 074018.

[75] H.-L. Lai, M. Guzzi, J. Huston, Z. Li, P. M. Nadolsky, J. Pumplin, and C.-P. Yuan, *New parton distributions for collider physics*, *Physical Review D* **82** (2010) 074024.

[76] S. Frixione, E. Laenen, P. Motylinski, C. White, and B. R. Webber, *Single-top hadroproduction in association with a W boson*, *Journal of High Energy Physics* **2008** (2008), no. 07 029.

[77] ATLAS Collaboration, *The ATLAS Simulation Infrastructure*, *European Physical Journal C* **70** (2010) 823–874, [arXiv:1005.4568].

[78] S. Agostinelli, et al., *Geant4—a simulation toolkit*, *Nuclear Instruments and Methods in Physics Research Section A: Accelerators, Spectrometers, Detectors and Associated Equipment* **506** (2003), no. 3 250–303.

[79] ATLAS Collaboration, *Performance of primary vertex reconstruction in proton-proton collisions at $\sqrt{s}$ =7 TeV in the ATLAS experiment*, . ATLAS-CONF-2010-069, `https://cds.cern.ch/record/1281344`.

[80] ATLAS Collaboration, *Characterization of Interaction-Point Beam Parameters Using the pp Event-Vertex Distribution Reconstructed in the ATLAS Detector at the LHC*, . ATLAS-CONF-2010-027, `https://cds.cern.ch/record/1277659`.

[81] ATLAS Collaboration, *Electron efficiency measurements with the ATLAS detector using the 2015 LHC proton-proton collision data*, Tech. Rep. ATLAS-CONF-2016-024, CERN, Geneva, 2016. `https://cds.cern.ch/record/2157687`.

[82] ATLAS Collaboration, *Muon reconstruction performance of the ATLAS detector in proton-proton collision data at $\sqrt{s}$ =13 TeV*, *European Physical Journal C* **76** (2016), no. 5 292. `https://arxiv.org/abs/1603.05598`.

[83] G. S. Salam et al., *The anti-k_t jet clustering algorithm*, *Journal of High Energy Physics* **0804** (2008) 063, [`arXiv:0802.1189`].

[84] ATLAS Collaboration, *Jet energy scale measurements and their systematic uncertainties in proton-proton collisions at $\sqrt{s} = 13$ TeV with the ATLAS detector*, *Physical Review D* **96** (2017), no. 7 072002.

[85] ATLAS Collaboration, *Performance of missing transverse momentum reconstruction for the ATLAS detector in the first proton-proton collisions at at $\sqrt{s}$= 13 TeV*, *The European Physical Journal C* **78** (2018), no. 11 903.

[86] ATLAS Collaboration, *Tagging and suppression of pileup jets*, Tech. Rep. ATLAS-CONF-2014-018, CERN, Geneva, 2014. `https://cds.cern.ch/record/1700870`.

[87] ATLAS Collaboration, *Forward Jet Vertex Tagging: A new technique for the identification and rejection of forward pileup jets*, Tech. Rep. ATL-PHYS-PUB-2015-034, CERN, Geneva, 2015. `https://cds.cern.ch/record/2042098`.

[88] ATLAS Collaboration, *Performance of b-Jet Identification in the ATLAS Experiment*, *Journal of Instrumentation* **11** (2016), no. 04 P04008.

[89] ATLAS Collaboration, *Optimisation of the ATLAS b-tagging performance for the 2016 LHC Run*, Tech. Rep. ATL-PHYS-PUB-2016-012, CERN, Geneva, 2016. https://cds.cern.ch/record/2160731.

[90] M. L. Mangano et al., *ALPGEN, a generator for hard multiparton processes in hadronic collisions*, *Journal of High Energy Physics* **0307** (2003) 001, [`hep-ph/0206293`].

[91] T. Gleisberg et al., *Event generation with SHERPA 1.1*, *Journal of High Energy Physics* **0902** (2009) 007, [`arXiv:0811.4622`].

[92] G. Cowan et al., *Asymptotic formulae for likelihood-based tests of new physics*, *European Physical Journal C* **71** (2011) 1554, [`arXiv:1007.1727`]. [Erratum: European Physical Journal **C 73**, 2501 (2013)].

[93] ATLAS Collaboration, *Measurements of b-jet tagging efficiency with the ATLAS detector using $t\bar{t}$ events at $\sqrt{s} = 13$ TeV*, *Journal of High Energy Physics* **08** (2018) 089.

[94] T. Plehn, D. Rainwater, and D. Zeppenfield, *Method for identifying $H \to \tau\tau \to e^{\pm}\mu^{\mp}p_T^{miss}$ at the CERN LHC*, *Physical Review D* **61** (2000), no. 9 093005.

[95] ATLAS Collaboration, *Jet energy scale measurements and their systematic uncertainties in proton-proton collisions at $\sqrt{s} = 13$ TeV with the ATLAS detector*, *Physical Review D* **96** (2017), no. 7 072002.

[96] ATLAS Collaboration, *Electron reconstruction and identification in the ATLAS experiment using the 2015 and 2016 LHC proton-proton*

collision data at $\sqrt{s}$ = 13 TeV, *European Physical Journal C* **79** (2019), no. 8 639.

[97] ATLAS Collaboration, *Electron and photon energy calibration with the ATLAS detector using 2015–2016 LHC proton-proton collision data*, *Journal of Instrumentation* **14** (2019), no. 03 P03017.

[98] ATLAS Collaboration, *E_T^{miss} performance in the ATLAS detector using 2015–2016 LHC pp collisions*, tech. rep., 2018. `https://cds.cern.ch/record/2625233`.

[99] D. B. Kaplan and H. Georgi, *SU(2) x U(1) Breaking by Vacuum Misalignment*, *Physics Letters* **B136** (1984) 183–186.

[100] J. Alwall, R. Frederix, S. Frixione, V. Hirschi, F. Maltoni, O. Mattelaer, H. S. Shao, T. Stelzer, P. Torrielli, and M. Zaro, *The automated computation of tree-level and next-to-leading order differential cross sections, and their matching to parton shower simulations*, *Journal of High Energy Physics* **07** (2014) 079, [`arXiv:1405.0301`].

[101] G. Passarino, C. Sturm, and S. Uccirati, *Higgs pseudo-observables, second Riemann sheet and all that*, *Nuclear Physics B* **834** (2010), no. 1-2 77–115.

[102] A. David and G. Passarino, *Through precision straits to next standard model heights*, *Reviews in Physics* **1** (2016) 13–28.

[103] M. Ghezzi, R. Gomez-Ambrosio, G. Passarino, and S. Uccirati, *NLO Higgs effective field theory and κ-framework*, *Journal of High Energy Physics* **2015** (2015), no. 7 175.

[104] A. Greljo et al., *Electroweak Higgs production with HIGGSPO at NLO QCD*, *European Physical Journal C* **77** (2017), no. 12 838.

[105] M. Gonzalez-Alonso et al., *Pseudo-observables in Higgs decays*, *European Physical Journal C* **75** (2015) 128, [`arXiv:1412.6038`].

[106] ATLAS Collaboration, *Measurement of inclusive and differential cross sections in the $H \to ZZ^* \to 4\ell$ decay channel in pp collisions at $\sqrt{s} = 13$ TeV with the ATLAS detector*, *Journal of High Energy Physics* **10** (2017) 132.

[107] ATLAS Collaboration, *Higgs boson production cross-section measurements and their EFT interpretation in the 4ℓ decay channel at $\sqrt{s}$ =13 TeV with the ATLAS detector*, *European Physical Journal C* **80** (2020), no. 10 957. [Erratum: European Physical Journal **C 81** (2021) 398].

[108] M. Baak et al., *Interpolation between multi-dimentional histograms using a new non-linear moment morphing method*, *Nuclear Instruments and Methods in Physics Research Section A: Accelerators, Spectrometers, Detectors and Associated Equipment* **771** (2015) 39–48.

[109] ATLAS Collaboration, *A morphing technique for signal modeling in a multidimentional space of coupling parameters*, . `https://cds.cern.ch/record/2066980`.

[110] Wouter Verkerke and David Kirkby, *The RooFit toolkit for data modeling*, 2003. `https://arxiv.org/abs/physics/0306116`.

[111] K. Cranmer, G. Lewis, L. Moneta, A. Shibata, and W. Verkerke, *HistFactory: A tool for creating statistical models for use with RooFit and RooStats*, tech. rep., New York U., New York, 2012. `https://cds.cern.ch/record/1456844`.

[112] E. N. Glover and J. van der Bij, *Higgs boson pair production via gluon fusion*, *Nuclear Physics* **B309** (1988) 282.

[113] T. Plehn, M. Spira, and P. Zerwas, *Pair production of neutral Higgs particles in gluon-gluon collisions*, *Nuclear Physics* **B479** (1996) 46–64, [`https://arxiv.org/abs/hep-ph/9603205`].

[114] S. Dawson, S. Dittmaier, and M. Spira, *Neutral Higgs boson pair production at hadron colliders: QCD corrections*, *Physical Review* **D58** (1998) 115012, [`hep-ph/9805244`].

[115] S. Borowka, N. Greiner, G. Heinrich, S. Jones, M. Kerner, J. Schlenk, and T. Zirke, *Full top quark mass dependence in Higgs boson pair production at NLO*, *Journal of High Energy Physics* **2016** (2016), no. 10 107.

[116] J. Baglio, A. Djouadi, R. Groeber, M. Muehlleitner, J. Quevillon, *et. al.*, *The measurement of the Higgs self-coupling at the LHC: theoretical status*, *Journal of High Energy Physics* **1304** (2013) 151, [arXiv:1212.5581].

[117] F. Maltoni, E. Vryonidou, and M. Zaro, *Top-quark mass effects in double and triple Higgs production in gluon-gluon fusion at NLO*, *Journal of High Energy Physics* **2014** no. 11 079.

[118] A. Djouadi, M. Spira, and P. Zerwas, *Production of Higgs bosons in proton colliders: QCD corrections*, *Physics Letters* **B264** (1991) 440–446.

[119] M. Spira, A. Djouadi, D. Graudenz, and P. Zerwas, *Higgs boson production at the LHC*, *Nuclear Physics* **B453** (1995) 17–82, [hep-ph/9504378].

[120] S. Dawson, *Radiative corrections to Higgs boson production*, *Nuclear Physics* **B359** (1991) 283–300.

[121] S. Borowka, N. Greiner, G. Heinrich, S. Jones, M. Kerner, J. Schlenk, U. Schubert, and T. Zirke, *Higgs Boson Pair Production in Gluon Fusion at Next-to-Leading Order with Full Top-Quark Mass Dependence*, *Physical Review Letters* **117** (2016), no. 1 012001.

[122] S. Borowka, N. Greiner, G. Heinrich, S. P. Jones, M. Kerner, J. Schlenk, U. Schubert, and T. Zirke, *Erratum: Higgs Boson Pair Production in Gluon Fusion at Next-to-Leading Order with Full Top-Quark Mass Dependence*, *Physical Review Letters* **117** (2016) 079901.

[123] D. Y. Shao, C. S. Li, H. T. Li, and J. Wang, *Threshold resummation effects in Higgs boson pair production at the LHC*, *Journal of High Energy Physics* **2013** (2013) 169. http://dx.doi.org/10.1007/JHEP07(2013)169.

[124] D. de Florian and J. Mazzitelli, *Higgs Boson Pair Production at Next-to-Next-to-Leading Order in QCD*, *Physical Review Letters* **111** (2013) 201801, [arXiv:1309.6594].

[125] J. Pumplin, D. Stump, J. Huston, H. Lai, P. M. Nadolsky, *et. al.*, *New generation of parton distributions with uncertainties from global QCD analysis*, *Journal of High Energy Physics* **0207** (2002) 012, [hep-ph/0201195].

[126] R. Frederix, S. Frixione, V. Hirschi, F. Maltoni, O. Mattelaer, *et. al.*, *Higgs pair production at the LHC with NLO and parton-shower effects*, *Physics Letters* **B732** (2014) 142–149, [arXiv:1401.7340]. Code available from https://cp3.irmp.ucl.ac.be/projects/madgraph/attachment/wiki/HiggsPairProduction/SM.tar.gz.

[127] H. Georgi and M. Machacek, *Doubly charged Higgs bosons*, *Nuclear Physics* **B262** (1985) 463.

[128] R. Grober and M. Muhlleitner, *Composite Higgs Boson Pair Production at the LHC*, *Journal of High Energy Physics* **1106** (2011) 020, [arXiv:1012.1562].

[129] M. Spira, "HPAIR program." Code available from https://tiger.web.psi.ch/hpair/.

[130] S. Kretzer, H. Lai, F. Olness, and W. Tung, CTEQ*6 parton distributions with heavy quark mass effects*, *Physical Review* **D69** (2004) 114005, [hep-ph/0307022].

[131] S. Dawson et al., *Handbook of LHC Higgs Cross Sections: 1. Inclusive Observables*, 2011. http://cds.cern.ch/record/1318996.

[132] U. Baur, T. Plehn, and D. L. Rainwater, *Probing the Higgs selfcoupling at hadron colliders using rare decays*, *Physical Review* **D69** (2004) 053004, [hep-ph/0310056].

[133] M. J. Dolan, C. Englert, and M. Spannowsky, *Higgs self-coupling measurements at the LHC*, *Journal of High Energy Physics* **1210** (2012) 112, [arXiv:1206.5001].

[134] S. Dawson, E. Furlan, and I. Lewis, *Unravelling an extended quark sector through multiple Higgs production?*, *Physical Review* **D87** (2013) 014007, [arXiv:1210.6663].

[135] Q. Li, Q.-S. Yan, and X. Zhao, *Higgs Pair Production: Improved Description by Matrix Element Matching*, *Physical Review* **D89** (2014) 033015, [arXiv:1312.3830].

[136] J. Grigo, J. Hoff, K. Melnikov, and M. Steinhauser, *On the Higgs boson pair production at the LHC*, *Nuclear Physics* **B875** (2013) 1–17, [arXiv:1305.7340].

[137] H. Haber and G. Kane, *The search for supersymmetry: Probing physics beyond the standard model*, *Physics Reports* **117** (1985), no. 2 75–263.

[138] ATLAS Collaboration, *Search for Higgs boson pair production in the $b\bar{b}b\bar{b}$ final state from pp collisions at $\sqrt{s} = 8$ TeV with the ATLAS detector*, *The European Physical Journal C* **75** (2015) 9.

[139] G. Aad *et. al.*, *Search For Higgs Boson Pair Production in the $\gamma\gamma b\bar{b}$ Final State using pp Collision Data at $\sqrt{s} = 8$ TeV from the ATLAS Detector*, *Physical Review Letters* **114** (2015), no. 8 081802, [arXiv:1406.5053].

[140] CMS Collaboration, *Search for resonant pair production of Higgs bosons decaying to two bottom quark-antiquark pairs in proton-proton collisions at 8 TeV*, *Physics Letters B* **749** (2015) 560, [arXiv:1503.0411].

[141] CMS Collaboration, *Search for heavy resonances decaying to two Higgs bosons in final states containing four b quarks*, *The European Physical Journal C* **76** (2016), no. 7 371.

[142] CMS Collaboration, *Search for resonant HH production in 2γ+2b channel*, CMS Physics Analysis Summary CMS-PAS-HIG-13-032, 2014. http://cdsweb.cern.ch/record/1697512.

[143] CMS Collaboration, *Model independent search for Higgs boson pair production in the $\mathrm{b\bar{b}}\tau^+\tau^-$ final state*, CMS Physics Analysis Summary CMS-PAS-HIG-15-013, Geneva, 2016. https://cds.cern.ch/record/2139335.

[144] R. Frederix, S. Frixione, V. Hirschi, F. Maltoni, O. Mattelaer, P. Torrielli, E. Vryonidou, and M. Zaro, *Higgs pair production at the*

LHC with NLO and parton-shower effects, *Physics Letters B* **732** (2014) 142–149.

[145] H.-L. Lai, M. Guzzi, J. Huston, Z. Li, P. M. Nadolsky, J. Pumplin, and C.-P. Yuan, *New parton distributions for collider physics*, *Physical Review D* **82** (2010), no. 7 074024.

[146] P. Nason, *A new method for combining NLO QCD with shower Monte Carlo algorithms*, *Journal of High Energy Physics* **2004** (2004), no. 11 040.

[147] S. Frixione, P. Nason, and C. Oleari, *Matching NLO QCD computations with parton shower simulations: the POWHEG method*, *Journal of High Energy Physics* **2007** (2007), no. 11 070.

[148] B. Mellado et al., *Handbook of LHC Higgs Cross Sections: 2. Differential Distributions*, 2012. `http://cds.cern.ch/record/1416519`.

[149] C. T. Potter et al., *Handbook of LHC Higgs Cross Sections: 3. Higgs Properties: Report of the LHC Higgs Cross Section Working Group*, 2013. `http://cds.cern.ch/record/1559921`.

[150] ATLAS Collaboration, *Calibration of the performance of b-tagging for c and light-flavour jets in the 2012 ATLAS data*, tech. rep., CERN, Geneva, 2014. `https://atlas.web.cern.ch/Atlas/GROUPS/PHYSICS/CONFNOTES/ATLAS-CONF-2014-046`.

[151] ATLAS Collaboration, *Measurements of fiducial and differential cross sections for Higgs boson production in the diphoton decay channel at* $\sqrt{s} = 8$ *TeV with ATLAS*, *Journal of High Energy Physics* **2014** (2014), no. 9 112.

[152] ATLAS Collaboration, *Identification and energy calibration of hadronically decaying tau leptons with the ATLAS experiment in pp collisions at* $\sqrt{s} = 8$ *TeV.*, *The European Physical Journal C* **75** (2015) 303.

[153] A. Elagin, P. Murat, A. Pranko, and A. Safonov, *A new mass reconstruction technique for resonances decaying to* $\tau\tau$, *Nuclear Instruments and Methods in Physics Research Section A:*

Accelerators, Spectrometers, Detectors and Associated Equipment **654** (2011), no. 1 481–489.

[154] ATLAS Collaboration, *Object-based missing transverse momentum significance in the ATLAS detector*, tech. rep., CERN, Geneva, 2018. `https://atlas.web.cern.ch/Atlas/GROUPS/PHYSICS/CONFNOTES/ATLAS-CONF-2018-038`.

[155] A. L. Read, *Presentation of search results: the CLs technique*, *Journal of Physics G: Nuclear and Particle Physics* **28** (2002), no. 10 2693.

[156] T. Binoth and J. J. van der Bij, *Influence of strongly coupled, hidden scalars on Higgs signals*, *Zeitschrift fuer Physik C Particles and Fields* **75** (1997), no. 1 17–25.

[157] R. Schabinger and J. D. Wells, *Minimal spontaneously broken hidden sector and its impact on Higgs boson physics at the CERN Large Hadron Collider*, *Physical Review D* **72** (2005), no. 9 093007.

[158] B. Patt and F. Wilczek, *Higgs-field Portal into Hidden Sectors*, 2006. `https://arxiv.org/abs/hep-ph/0605188`.

[159] C.-Y. Chen, S. Dawson, and I. M. Lewis, *Exploring resonant di-Higgs boson production in the Higgs singlet model*, *Physical Review D* **91** (2015), no. 3 035015, [`arXiv:1410.5488`].

[160] S. Dawson and I. M. Lewis, *NLO corrections to double Higgs boson production in the Higgs singlet model*, *Physical Review D* **92** (2015), no. 9 094023.

[161] T. Robens and T. Stefaniak, *Status of the Higgs Singlet Extension of the Standard Model after LHC Run 1*, *European Physical Journal C* **75** (2015) 104.

[162] T. Robens and T. Stefaniak, *LHC Benchmark Scenarios for the Real Higgs Singlet Extension of the Standard Model*, *European Physical Journal C* **76** (2016), no. 5 268, [`arXiv:1601.0788`].

[163] ATLAS Collaboration, *Search for Higgs boson pair production in the $\gamma\gamma b\bar{b}$ final state with 13 TeV pp collision data collected by the ATLAS experiment*, *Journal of High Energy Physics* **2018** (2018), no. 11 40.

[164] CMS Collaboration, *Searches for a heavy scalar boson* H *decaying to a pair of 125 GeV Higgs bosons* hh *or for a heavy pseudoscalar boson* A *decaying to* Zh*, in the final states with* $\mathrm{h} \to \tau\tau$, *Physics Letters B* **755** (2016) 217–244.

[165] CMS Collaboration, *Search for resonant pair production of Higgs bosons decaying to* $b\bar{b}$ *and* $\tau^+\tau^-$ *in proton-proton collisions at* $\sqrt{s} = 8$ *TeV*, Tech. Rep. CMS-PAS-EXO-15-008, Geneva, 2015. `https://cds.cern.ch/record/2125293`.

[166] ATLAS Collaboration, *Search for pair production of Higgs bosons in the* $b\bar{b}b\bar{b}$ *final state using proton-proton collisions at* $\sqrt{s} = 13$ *TeV with the ATLAS detector*, *Journal of High Energy Physics* **2019** (2019), no. 1 30.

[167] ATLAS Collaboration, *Search for Higgs boson pair production in the* $b\bar{b}WW^*$ *decay mode at* $\sqrt{s} = 13$ *TeV with the ATLAS detector*, *Journal of High Energy Physics* **2019** (2019), no. 4 92.

[168] ATLAS Collaboration, *Search for Resonant and Nonresonant Higgs boson pair production in the* $b\bar{b}\tau^+\tau^-$ *decay channel in pp collisions at* $\sqrt{s} = 13$ *TeV with the ATLAS Detector*, *Physical Review Letters* **121** (2018), no. 19 191801.

[169] ATLAS Collaboration, *Search for Higgs boson pair production in the* WW^*WW^* *decay channel using ATLAS data recorded at* $\sqrt{s} = 13$ *TeV*, *Journal of High Energy Physics* **2019** (2019), no. 5 124.

[170] ATLAS Collaboration, *Search for Higgs boson pair production in the* $\gamma\gamma WW^*$ *channel using pp collision data recorded at* $\sqrt{s} = 13$ *TeV with the ATLAS detector*, *The European Physical Journal C* **78** (2018), no. 12 1007.

[171] ATLAS Collaboration, *Combination of searches for Higgs boson pairs in pp collisions at* $\sqrt{s} = 13$ *TeV with the ATLAS detector*, *Physics Letters B* **800** (2020) 135103.

[172] M. Bähr, S. Gieseke, M. A. Gigg, D. Grellscheid, K. Hamilton, O. Latunde-Dada, S. Plätzer, P. Richardson, M. H. Seymour, A. Sherstnev, and B. R. Webber, *Herwig++ physics and manual*, *The European Physical Journal C* **58** (2008), no. 4 639–707.

[173] M. H. Seymour and A. Siódmok, *Constraining MPI models using σ_{eff} and recent Tevatron and LHC Underlying Event data*, *Journal of High Energy Physics* **2013** (2013), no. 10 113.

[174] T. Sjöstrand, S. Ask, J. R. Christiansen, R. Corke, N. Desai, P. Ilten, S. Mrenna, S. Prestel, C. O. Rasmussen, and P. Z. Skands, *An introduction to pythia 8.2*, *Computer Physics Communications* **191** (2015) 159–177.

[175] R. D. Ball, V. Bertone, S. Carrazza, C. S. Deans, L. Del Debbio, S. Forte, A. Guffanti, N. P. Hartland, J. I. Latorre, J. Rojo, and M. Ubiali, *Parton distributions with LHC data*, *Nuclear Physics B* **867** (2013), no. 2 244–289.

[176] L. Randall and R. Sundrum, *Large Mass Hierarchy from a Small Extra Dimension*, *Physical Review Letters* **83** (1999), no. 17 3370–3373.

[177] R. Costa, M. Mühlleitner, M. O. P. Sampaio, and R. Santos, *Singlet extensions of the Standard Model at LHC Run 2: benchmarks and comparison with the NMSSM*, *Journal of High Energy Physics* **2016** (2016), no. 6 34.

[178] ALTAS Collaboration, *Constraints on new phenomena via Higgs boson couplings and invisible decays with the ATLAS detector*, *Journal of High Energy Physics* **2015** (2015), no. 11 206.

[179] A. Noble and M. Perelstein, *Higgs self-coupling as a probe of the electroweak phase transition*, *Physical Review D* **78** (2008) 063518. `http://dx.doi.org/10.1103/PhysRevD.78.063518`.

[180] A. D. Sakharov, *Violation of CP Invariance, C asymmetry, and baryon asymmetry of the universe*, *Journal of Experimental and Theoretical Physics* **5** (1967) 32–35.

[181] V. A. Rubakov and M. E. Shaposhnikov, *Electroweak baryon number non-conservation in the early Universe and in high-energy collisions*, *Physics-Uspekhi* **39** (1996), no. 5 461–502.

[182] ATLAS Collaboration, *Studies of new Higgs boson interactions through nonresonant HH production in the $b\bar{b}\gamma\gamma$ final state in pp*

collisions at $\sqrt{s}$ = 13 TeV with the ATLAS detector, *Journal of High Energy Physics* **2024** (2024), no. 1 66.

[183] ATLAS Collaboration, *Search for the nonresonant production of Higgs boson pairs via gluon fusion and vector-boson fusion in the $b\bar{b}\tau^+\tau^-$ final state with the ATLAS detector*, *Physical Review D* **110** (2024), no. 3 032012.

[184] ATLAS Collaboration, *Search for non-resonant Higgs boson pair production in final states with leptons, taus, and photons in pp collisions at $\sqrt{s}$ = 13 TeV with the ATLAS detector*, *Journal of High Energy Physics* **2024** (2024), no. 8 164.

[185] ATLAS Collaboration, *Search for non-resonant Higgs boson pair production in the $2b + 2\ell + E_T^{miss}$ final state in pp collisions at $\sqrt{s}$ = 13 TeV with the ATLAS detector*, *Journal of High Energy Physics* **2024** (2024), no. 2 37.

[186] ATLAS Collaboration, *Combination of Searches for Higgs Boson Pair Production in pp collisions at $\sqrt{s} = 13$ TeV with the ATLAS Detector*, *Physical Review Letters* **133** (2024), no. 10 101801.

[187] CMS Collaboration, *Search for Higgs boson pair production in events with two bottom quarks and two tau leptons in proton–proton collisions at $\sqrt{s}$ =13 TeV*, *Physics Letters B* **778** (2018) 101–127.

[188] M. Slawinska, *High-Luminosity LHC prospects with the upgraded ATLAS detector*, *Proceedings of Science* **DIS2016** (2016) 266.

[189] ATLAS Collaboration, *Letter of Intent for the Phase-II Upgrade of the ATLAS Experiment*, Tech. Rep. CERN-LHCC-2012-022. LHCC-I-023, CERN, Geneva, 2012. `https://cds.cern.ch/record/1502664`.

[190] ATLAS Collaboration, *ATLAS Phase-II Upgrade Scoping Document*, Tech. Rep. CERN-LHCC-2015-020. LHCC-G-166, CERN, Geneva, 2015. `https://cds.cern.ch/record/2055248`.

[191] U. Baur, T. Plehn, and D. L. Rainwater, *Measuring the Higgs boson self coupling at the Large Hadron Collider* , *Physical Review Letters* **89** (2002) 151801, [`hep-ph/0206024`].

[192] D. de Florian and J. Mazzitelli, *Higgs Boson Pair Production at Next-to-Next-to-Leading Order in QCD*, *Physical Review Letters* **111** (2013), no. 20 201801.

[193] J. Grigo, K. Melnikov, and M. Steinhauser, *Virtual corrections to higgs boson pair production in the large top quark mass limit*, *Nuclear Physics B* **888** (2014) 1729.

[194] ATLAS Collaboration, *Performance assumptions for an upgraded ATLAS detector at a High-Luminosity LHC*, Tech. Rep. ATL-PHYS-PUB-2013-004, CERN, Geneva, 2013. `https://cds.cern.ch/record/1527529`.

[195] ATLAS Collaboration, *Performance assumptions based on full simulation for an upgraded ATLAS detector at a High-Luminosity LHC*, Tech. Rep. ATL-PHYS-PUB-2013-009, CERN, Geneva, 2013. `https://cds.cern.ch/record/1604420`.

[196] ATLAS Collaboration, *Measurement prospects of Higgs boson pair production in the $b\bar{b}\gamma\gamma$ final state with the ATLAS experiment at the HL-LHC*, tech. rep., CERN, Geneva, 2022. `https://atlas.web.cern.ch/Atlas/GROUPS/PHYSICS/PUBNOTES/ATL-PHYS-PUB-2022-001`.

[197] ATLAS Collaboration, *Observation of electroweak production of W^+W^- in association with jets in proton-proton collisions at $\sqrt{s}$ = 13 TeV with the ATLAS detector*, *Journal of High Energy Physics* **07** (2024) 254.

[198] ATLAS Collaboration, *Evidence of pair production of longitudinally polarised vector bosons and study of CP properties in $ZZ \to 4\ell$ events with the ATLAS detector at $\sqrt{s}$ = 13 TeV*, *Journal of High Energy Physics* **12** (2023) 107.

[199] ATLAS Collaboration, *Studies of the Energy Dependence of Diboson Polarization Fractions and the Radiation-Amplitude-Zero Effect in WZ Production with the ATLAS Detector*, *Physical Review Letters* **133** (2024), no. 10 101802. [Erratum: Physical Review Letters 133, 169901 (2024)].

[200] I. Brivio and M. Trott, *The Standard Model as an Effective Field Theory*, *Physics Reports* **793** (2019) 1–98.